ASSISTED NERVE REGENERATION UTILIZING NOVEL NERVE CONDUITS WITH WALL-ENCAPSULATED CELLS

by

Aaron Xu Sun

B.S. in Electrical & Computer Engineering and Chemistry, Rutgers University 2013

Submitted to the Graduate Faculty of

Swanson School of Engineering in partial fulfillment

of the requirements for the degree of

Doctor of Philosophy

University of Pittsburgh

2018

UNIVERSITY OF PITTSBURGH

SWANSON SCHOOL OF ENGINEERING

This dissertation was presented

by

Aaron X. Sun

It was defended on

July 26, 2018

and approved by

Kacey G. Marra, Ph.D.
Associate Professor, Departments of Plastic Surgery & Bioengineering

Andrew W. Duncan, Ph.D.
Assistant Professor, Department of Pathology & Bioengineering

Bryan N. Brown, Ph.D.
Assistant Professor, Depratment of Bioengineering & Obstetrics, Gynecology, and Reproductive Services & Clinical and Translational Science Institute

Dissertation Director: Rocky S. Tuan, Ph.D.
Distinguished Professor, Departments of Orthopaedic Surgery & Bioengineering & Mechanical and Materials Science

ASSISTED NERVE REGENERATION UTILIZING NOVEL NERVE CONDUITS WITH WALL-ENCAPSULATED CELLS

Aaron X. Sun, PhD

University of Pittsburgh, 2018

Peripheral nerves possess an innate ability to regenerate, but following complete transection or segmental damage to the nerve, surgical intervention is required to re-approximate the ends of a nerve for a chance at functional recovery. Among the treatment options, synthetic nerve conduits are a promising tissue engineering approach to effect peripheral nerve regeneration across functionally debilitating segmental defects. An essential step in this restoration is the formation of a "nerve bridge" pioneered by Schwann cells that migrate to the center of the conduit in response to chemokine gradients.

This work in this dissertation focuses on the creation of a chemokine gradient in nerve conduits through the use of stem cell-secreted neurotrophic factors. While cell incorporation inside conduits is a widely applied technique and has demonstrated some beneficial effects, conventional cell-seeding methods fail to produce a directional signal for invading Schwann cells. A large part of the challenge to providing this signal is the ability to localize cells to a desired region. The work herein elaborates a versatile, single-step method to encapsulate neurotrophically active cells within the walls of a conduit through the use of a composite

nanofibrous scaffold, allowing for strict control of cell number and spatial distribution along the length of the conduit. The resulting structure significantly enhances dorsal root ganglion outgrowth *in vitro*, and is flexible and mechanically suitable for *in vivo* implantation. Utilizing stem cells encapsulated within the central third of the conduit, markedly different cell distribution (Gaussian vs. quadratic) and retention are observed over the course of 6 weeks in a 10 mm rat sciatic nerve transection model when compared to standard cell injection method. This drives Schwann cell migration into the center of the regenerating nerve bridge, and at 16 weeks rats presented with significantly enhanced function and axon myelin over control. Taken together, the work in this dissertation demonstrates that this method of utilizing a spatially restricted cell secretome, which is a departure from conventional homogeneous or uncontrolled cell loading, presents a new paradigm for studying and maximizing the potential of cell application in peripheral nerve repair.

TABLE OF CONTENTS

LIST OF TABLES

LIST OF FIGURES

PREFACE

Funding acknowledgements

U.S. Department of Defense (W81XWH-15-1-0600 and W81XWH-14-1-0217)

National Institutes of Health (R01 GM115444 and T32 EB001026)

Acknowledgements

First and foremost I would like to acknowledge my primary mentor and advisor, Dr. Rocky S. Tuan, for making all of this possible. I could not have asked for a better advisor – he allowed me freedom to pursue my interests within the lab, provided guidance when it was needed, and pushed me to continually consider alternate paths of thinking. The way he made connections throughout his expansive knowledge base was a model that I strove to be able to emulate. Through Rocky, I have had the opportunity to study various avenues in tissue engineering and developmental biology, and my graduate experience was all the more rewarding because of this. So to Rocky a true heartfelt thank you for making my PhD the best it could be.

Next, I would like to acknowledge the many mentor figures I have had in my path through graduate school. Dr. Hang Lin was the first person I worked with in the lab, and through him I learned the ins and outs of cartilage tissue engineering. He was a good friend, colleague, and mentor and I cannot thank him enough for his early guidance. Dr. Pete Alexander was always a sounding board for ideas, and challenged me to think more critically about what impact

I wanted my work to have. Dr. Thomas Lozito was an irreplaceable *senior* friend and mentor, and I can easily say my growth as a scientist was in large part due to working with him and his lizards/salamanders. I am very grateful to have coincided with him during my time at the lab. Lastly, I want to give a special thanks to Dr. Ben Rothrauff. From the start of my PhD, he has been a consistent figure I could always turn to and talk to about anything – whether it was scientific or non-scientific. His insightful discussions on the state of the field or future paths allowed me to really mature as a scientist, and his commitment to his work was inspiring. I cannot imagine a PhD without Ben in the lab. To all my mentors, I sincerely wish you success in your promising careers.

These acknowledgements would of course be incomplete without mention of the various people that have worked with me and supported me in my various projects: Alyssa Falcione, Travis Prest, John Fowler, Rachel Brick, Ricardo Londono, He Shen, Megan Hudnall, Yuhao Deng, Jian Tan, Shinsuke Kihara, Peter Mittwede, Kelsey Gloss, Eddie Lu, Xinyu Li, Gary Yu, Kalon Overholt, Madalyn Fritch, Michael DeHart, Kim Möller, Daniel McKeel, and Guang Yang. I would like to give special thanks to Alyssa Falcione for managing all of my animals during the *in vivo* phases of my projects and showing me the ropes with animal work. However, everyone I worked with was vital to the success of the projects, and I would like to give thanks to everyone who worked with me. In addition to them, I would like to acknowledge the rest of the lab as well for providing a welcoming environment and tight-knit community that fostered collaboration and a sense of family.

Lastly, I would like to thank my family and friends for all their support throughout these PhD years. It goes without saying that in their absence, this journey would not have been possible.

1.0 INTRODUCTION

Across both mammalian and non-mamallian species, nerves are divided into two broad categories: central nerves and peripheral nerves, each comprising their own "system". While the central nervous system (CNS) is responsible for conscious executive function and functions as a control center, the peripheral nervous system (PNS) is the effector system responsible for interfacing the organism with the physical world around it. In terms of physical structure, the nerves that comprise the CNS are found in the spinal cord and brain, and all other nerves in the body are classified as peripheral. Broadly, the functions of the PNS thus include, but are not limited to movement, sensory input, and unconscious control of autonomic functions such as breathing and bowel movement – thus the integrity of the PNS is vital to the normal functioning of an organism. The peripheral nerves that comprise the PNS – specifically their regeneration after injury - are the focus of this dissertation.

Before discussing peripheral nerve injury, a look at the basic structure of a peripheral nerve is informative (Figure 1). The functional structure of the nerve is the axon that transmits signals from or to the cell body, which is located in the spinal cord for motor neurons or the dorsal root ganglion adjacent to the spinal cord for sensory nerves. Surrounding each individual axon is a structure known as the endoneurium, which is comprised of connective tissue elements such as Collagen IV, hyaluronan, and vascular structures. In addition, some axons are myelinated by Schwann cells that increase signal transduction and support the axonal structure. Going up a

level, groups of axons and their associated endoneuria cluster together and are contained by a structure known as the perineurium. Lastly, at the highest level, bundles of axons and their associated perineuria are enclosed within the epineurium. The epineurium is the structure that is grossly observed when the nerve is exposed via surgical means, and is composed of connective tissue elements such as Collagens I, Collagen III, and vascular elements. As evidenced by this hierarchy, peripheral nerves rely on a highly organized structure in order to transmit signals and innervate their proper endplates. With this understanding of the peripheral nerve structure, the processes disruption, injury, and subsequent regeneration of this architecture will now be discussed herein.

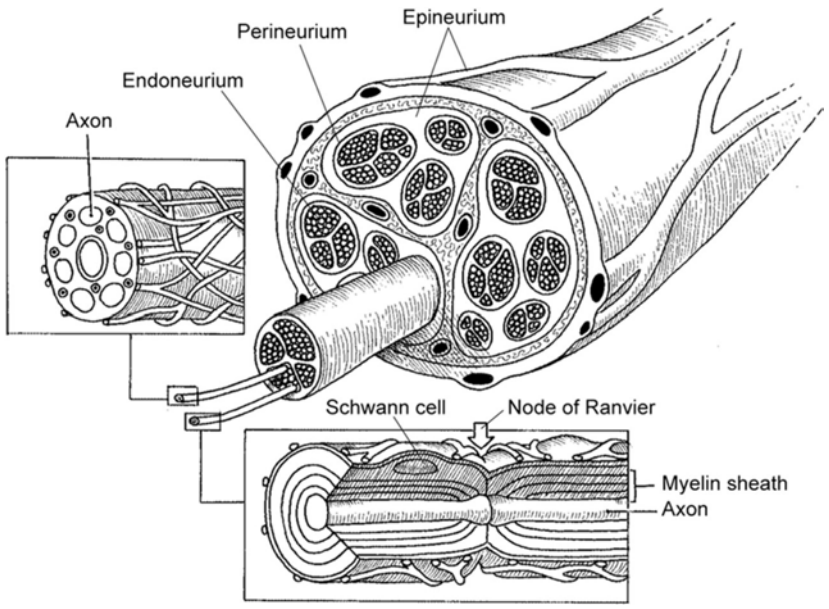

Figure 1: Anatomy of the peripheral nerve. Individual axons are surrounded by a myelin sheath produced by Schwann cells and encased within an endoneurium. Groups of axons and their endoneuria are bundled together within the perineurium. Groups of perineuria are encased by the epineurium, which is the outer layer of the nerve. Adapted from Griffin et al.[1] with permission from Wolter Kluwer.

1.1 PERIPHERAL NERVE INJURY

Peripheral nerve injury (PNI) affects over 300,000 people each year in the United States and is a significant cause of morbidity and lifelong disability despite surgical intervention.[2] Soldiers in particular are exposed to higher incidences of PNI due to battlefield injuries, and PNI morbidity leads to reduced military preparedness, early discharge, poor reintegration into civilian life, and has been implicated in higher rates of depression and suicide among these veterans.[3,4] Not only do they cause loss of function and major disability, they are also a huge economic burden for both the individual as well as society costing the United States approximately $150 billion annually in healthcare dollars.[5]

1.1.1 Classifications of Peripheral Nerve Injury

PNI can occur through a number of mechanisms, with disease and trauma being the most common.[6–8] Among diseases, conditions such as the formation of Schwannomas and degenerative processes like Charcot-Marie-Tooth lead to a decrease in the normal functioning of nerves and in some cases necessitate surgery. On the traumatic side, crush, stretch, and transection are the most common forms of injury to the nerve. These traumatic injuries were first categorized by Seddon in 1943 into three distinct categories (neurapraxia, axonotmesis, and neurotmesis),[9] and later expanded by Sunderland in 1951 into five escalating degrees of nerve injury (Figure 2).[10] Neurapraxia (Sunderland Class I) involves crush of the axons with no disruption in the axon or any of its surrounding structures – nerves subjected to this damage have delayed impulse conduction to varying degrees but generally recover in the timespan of weeks. Increasing in severity is axonotmesis (Sunderland Class II), which involves the loss of continuity

of the axon and its surrounding myelin but not its connective tissue coverings. In this case, conduction distal to the damaged axon is lost, but again recovery generally occurs without surgical intervention except in select cases where scar tissue formation may impede regrowth. Lastly, the most severe category, neurotmesis, involves a discontinuity in the axon as well as well as its connective tissue coverings (Sunderland Class III-V corresponding to endoneurial, perineurial, or epineurial discontinuity, respectively). These are the most severe injuries, and in the case of epineurial discontinuity (Sunderland Class V, also referred to as complete nerve transection), functional regeneration does not occur without surgical intervention. It is the bridging of these complete nerve transections that is the subject of this dissertation and will be discussed further.

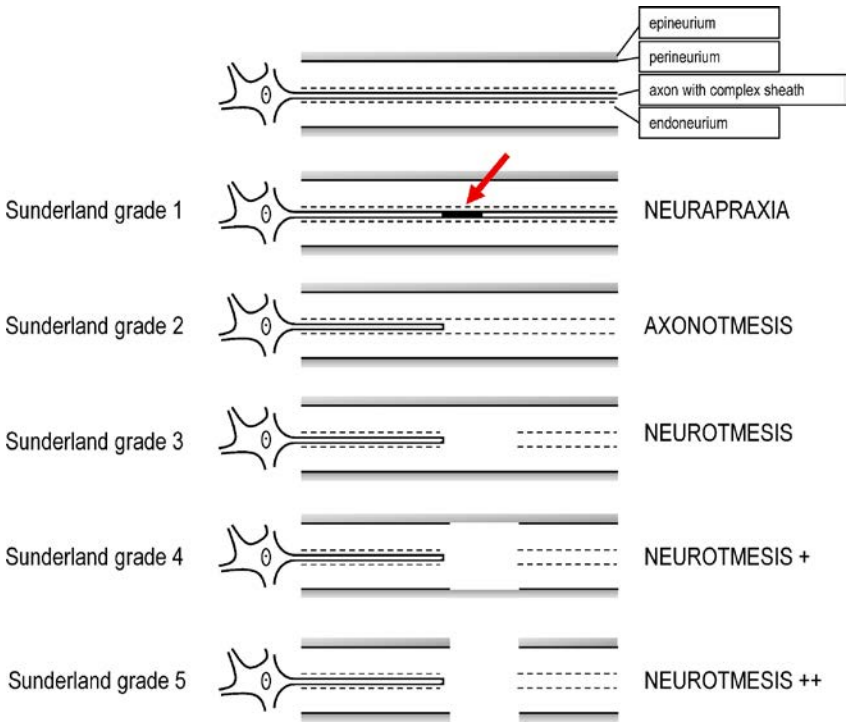

Figure 2: Sunderland nerve injury classification. Sunderland described 5 grades of nerve injury from least to most severe. These progress from crush (grade 1), to axonal discontinuity (grade 2), to endoneurial discontinuity (grade 3), to perineurial (grade 4) and finally epineurial discontinuity (grade 5). Adapted from Deumens et al.[11] with permission from Elsevier.

1.1.2 Challenges in Peripheral Nerve Regeneration

Complete transection of axons as well as all supporting tissues is associated with poor outcomes following injury.[12] While peripheral nerves possess the ability to regenerate at a rate of approximately 1-2 mm per day, during the process of nerve regrowth across large defects many obstacles arise that make regeneration across it a major challenge.[13–15] First, scar tissue formation at the site of injury can impede the growth and passage of axons across the defect. This fibrotic scar formation occurs due to the activity of resident fibroblasts within the nerve sheaths and

presents a physical barrier for axonal growth. Second, even with an unobstructed path, axonal dispersion occurs due to the highly irregular paths that axons can take. This phenomenon, in addition to the sprouting of collateral branches from growing nerves, results in inappropriate re-innervation when the axon finally reaches the motor endplate. Lastly, in the repair of large segmental defects (either aided or non-aided with surgical measures), axonal growth can become highly disordered and coalesce into a neuroma, which is a collection of axons in a ball-like structure, that induces neuropathic pain due to the spontaneous firing of action potentials within the tumorous growth. The advent of a neuroma also leads to subsequent target organ atrophy due to loss of innervation. Due to these factors, surgical intervention is required for functional return in cases of complete nerve transection.

1.1.3 Surgical Treatments for Complete Nerve Transection

There currently exist a number of surgical techniques used to repair nerve damage of varying location and severity.[1,11,16,17] Here we will exclude repairs techniques that do not bridge a gap within the same nerve (such as nerve transfer where a synergistic nerve may be used to re-innervate a muscle) and instead focus on repairs that connect the proximal to distal end of an injured nerve. Currently, the best treatment option for this type of nerve defect is tensionless end-to-end repair. In this procedure, the opposing ends of the nerve are directly sutured together (epineurially or perinuerially matched) allowing for nerves to grow directly from the proximal end through the distal stump. This technique boasts predictable positive outcomes, but often this is not an option because conditions must be “optimal”: repair immediately after injury (or very shortly thereafter), minimal gap <2.5 mm in length to avoid stretching of the nerve (which can decease blood supply), good blood supply and soft-tissue coverage, and lastly exact alignment of

the opposing ends obtained through epirneurial or perineurial matching.[1,11,16] In the case that end-to-end repair is not possible, the gold standard option is autografting. In this procedure, a nerve from another site (generally the sural nerve or other cutaneous nerve) is harvested from the patient and used to bridge the defect site, providing live Schwann cells (the functional support unit of the growing nerve) and the nerve tissue architecture. However, there are many downsides to this: diameter mismatch necessitates cabling (the use of multiple tubular grafts to create a larger diameter), the donor site is left innervated which can lead to consequences such as neuroma formation, and lastly there is a limited amount of donor material. Indeed, another complicating factor lies in the fact that there is only a 40-50% success rate for this gold standard technique. Alternative to the autograft, an allograft can instead be used where the transplanted nerve is taken from another (usually cadaveric) human. However, this technique does not allow for a live graft with functioning Schwann cells to be used because of immune rejection. In addition to these commonly used grafts, other grafts such as veins, muscle, or xenograft may be used as well, but they are not as commonly applied and will not be discussed.

More recently, in an attempt to overcome the limitations mentioned earlier, biomaterial nerve conduits have been employed in the search for an effective and efficient pathway to effect nerve regeneration. These nerve conduits are tubular in structure and provide a channel for nerves to grow through. This has demonstrated various benefits: potential for reduced neuroma formation, improved axon directionality and lack of axonal escape, and lack of donor-site morbidity. However, the main drawback of this technique is that current clinically applied synthetic nerve conduits are constrained in the range of nerve gaps they are able to bridge ($\leq$3 cm), as they have very poor functional recovery rates at lengths greater than this.[18] Table 1 lists the current FDA-approved nerve conduits for off-the-shelf repair of nerve defects - a discussion

of the efficacies of these conduits will not be presented here, but information can be found in well-written reviews on this topic.[19] Overall, there is still a need for biomaterials that can provide the complex bioactive cues that are necessary for nerve regeneration, and key to designing an "optimal" nerve conduit involves understanding the basic biology that occurs after a nerve is injured.

Table 1. Current FDA-approved nerve conduits for repair of peripheral nerve gaps. Reprinted from Gaudin et al.[20] under Creative Commons Attribution License.

Product	Material	Structure	Degradation time	Company	FDA-approval
NeuroTube	Polyglycolic acid	Absorbable woven mesh tube	3 mo	Synovis Micro Companies	1999
NeuraGen	Type I collagen	Semipermeable, fibrillar	3-4 yrs	Integra LifeSciences Co., Plainsboro, NJ, USA	2001
NeuroFlex	Type I collagen	Semipermeable, flexible, tubular	4–8 mo	Collagen Matrix, Inc., Franklin	2001
NeuroMatrix	Type I collagen	Semipermeable, flexible, tubular	4–8 mo	Collagen Matrix, Inc.	2001
NeuraWrap	Type I collagen	Semipermeable, longitudinal slit in wall	36–48 mo	Integra LifeSciences Co.	2004
NeuroMend	Type I collagen	Semipermeable wrap, unrolls and self-curls	4–8 mo	Collagen Matrix, Inc.	2006
Neurolac	Poly-DL-lactide-caprolactone	Synthetic and transparent, tubular	16 mo	Polyganics BV, Groningen, Netherlands	2003
SaluTunnel	Polyvinyl alcohol	Nonbiodegradable	No degradation	Salumedica LLC, Atlanta, GA, USA	2010
Avance	☒Processed human nerve allograft			AxoGen, Inc., Alachua, FL	2010
AxoGuard	Extracellular matrix derived from porcine small intestine submucosa	Absorbable semipermeable	No data	AxoGen, Inc., Alachua, FL	2013

1.2 THE NERVE REGENERATION PROCESS

As mentioned before, peripheral nerves possess the inherent ability to regenerate following damage to the nerve architecture. This is a highly coordinated sequence of events involving multiple cell types, and success is dependent on the completion of these processes. In this section, the nerve regeneration sequence will be covered, both with and without the aid of a tubular nerve conduit.

1.2.1 Wallerian Degeneration and Subsequent Regeneration

Normally, following injury to the nerve a process of events initiated by Wallerian degeneration occurs (Figure 3).[9] First, homeostasis is re-established through calcium-dependent degradation of cell material with retraction of both the proximal and distal ends of the axon (Figure 3A). Next, an inflammatory phase takes place where macrophages, T-cells, neutrophils, and other inflammatory cells clear the damaged nerve tissue and extracellular debris (Figure 3B). It is in this stage that scar tissue can form in large nerve defects, which can hinder the subsequent functional repair of the neural tissue. Following the inflammatory phase, a proliferative phase occurs where Schwann cells from the proximal axon stump form bands of Bungner as they align and begin to proliferate towards the distal stump (Figure 3C). This step involving the directional migration of Schwann cells is critical for successful regeneration because the bands of Bunger are the framework for the growth of axons as they regrow from the proximal to the distal end of the nerve. In cases where fibrous tissue is present, a painful neuroma can form as the scar blocks band of Bungner formation, which also leads to target organ atrophy due to loss of innervation (Figure 3E). Lastly, in the remodeling phase the Schwann cells that form the bands of Bungner

secrete neurotrophic factors (NTF) such as brain-derived neurotrophic factor (BDNF), ciliary neurotrophic factor (CNTF), nerve growth factor (NGF), and glial cell line-derived neurotrophic factor (GDNF), which assist with axonal sprouting, guidance, and survival (Figure 3D).[21] These cytokines have been shown to improve both nerve remyelination and regrowth, and play a key role in survival of motor and sensory neurons.[22]

1.2.2 Regeneration in a Nerve Conduit

In the case of regeneration in a hollow nerve conduit, the microenvironment within the conduit space is especially important (Figure 4).[23] Starting with a fluid phase, plasma exudate from both the proximal and distal nerve stumps fills the tube with neurotrophic factors and extracellular matrix (ECM) precursor molecules. This sets the stage for the next phase, the matrix phase, where a fibrin cable formed from the ECM precursor molecules extends from one stump to the other. The fibrin cable then acts as a framework from which the final stages of Schwann cell migration, axonal extension, and myelination occur. Given the key role of the fibrin cable bridge, providing physical and chemical cues to allow for its formation and subsequent cell migration is critical, and these will be discussed in the following sections.

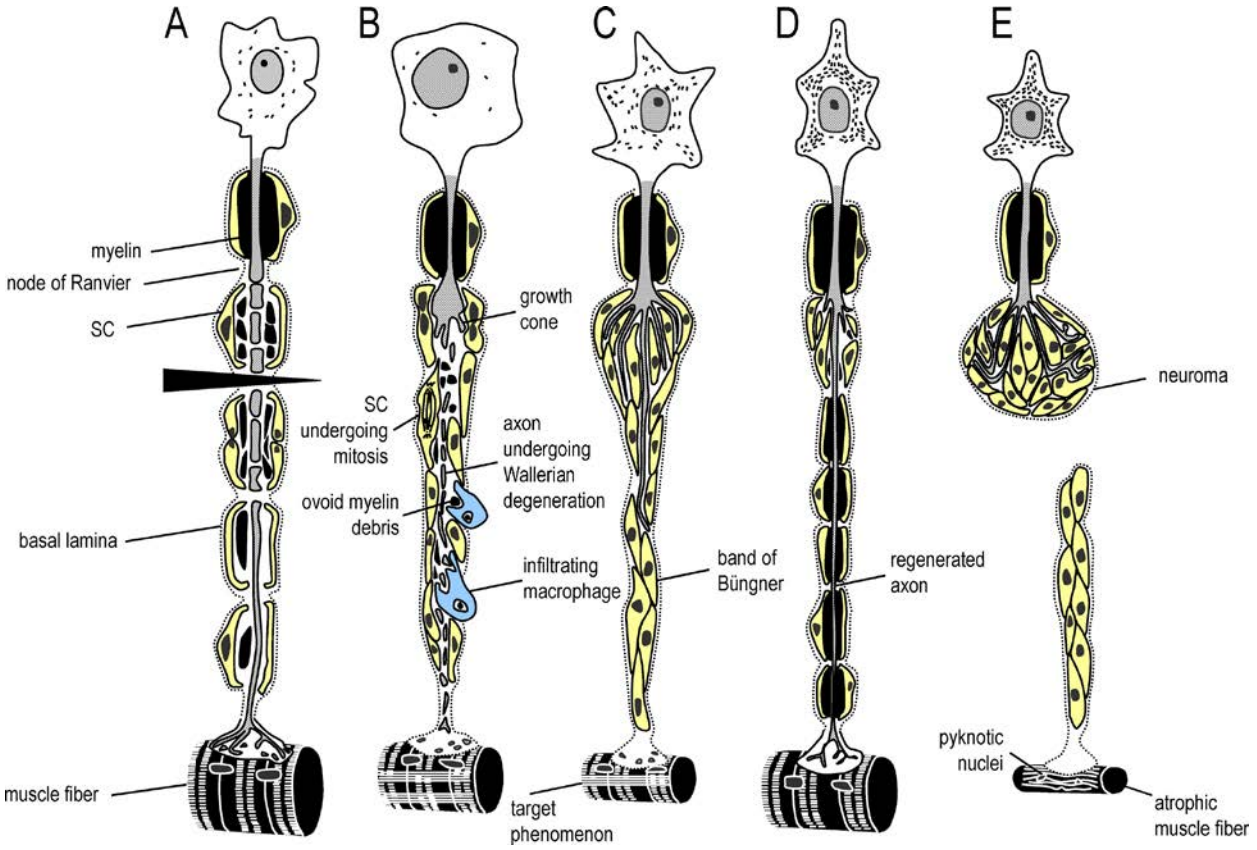

Figure 3. Nerve regeneration process following axonal damage. Briefly, damage to the axon results in degeneration of the axon proximally and distally (A). This then triggers the process of anterograde Wallerian degeneration and the infiltration of macrophages to clean up debris. The cell body also undergoes chromalytic, reactive changes to prime for the process of synthesis, and the muscle endplate starts to atrophy (B). Next, Schwann cells migrate from the proximal and distal end of the damage site and establish bands of Büngner for regenerating sprouts from the proximal end to regenerate into (C). Lastly, successful regeneration and re-innervation leads to reconnection and signaling at neuromuscular junctions. Axons that do not reach the end-target die back and muscle fiber atrophy is reversed as well (D). In the event that axons cannot bridge the injury site (such as in complete nerve transection), axons can form into a neuroma – a painful bundle of nerve fibers that spontaneously gives rise to action potentials (F). Adapted from Deumens et al.[11] with permission from Elsevier.

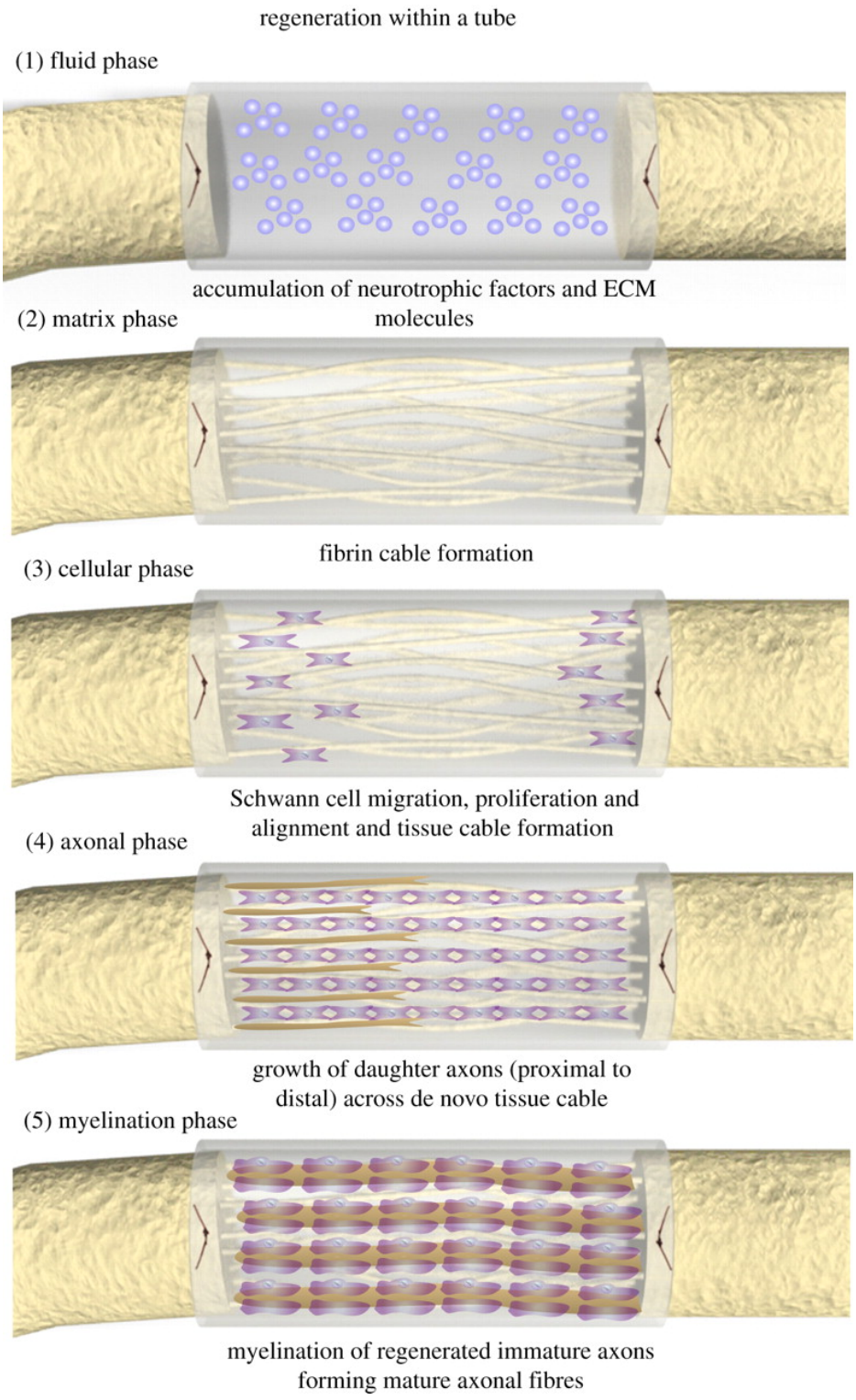

Figure 4. Regeneration within a tubular nerve conduit. Adapted from Daly et al.[18] with permission from Royal Society.

1.3 AUGMENTING NERVE REGENERATION

Nerve regeneration is a complex process that requires coordination of various signals, both biological and physical. Over the decades, factors that have been found to enhance or guide this phenomenon have been discovered and studied. Indeed, in the absence of many of these cues regeneration is greatly hindered, but on the flipside appropriate application of these factors can profoundly aid regrowth and survival. In this section, the major pathways to enhance nerve regeneration will be discussed.

1.3.1 Neurotrophic Growth Factors

Since the discovery that NGF increased neurite extension length in dorsal root ganglia in the 1950s,[24–26] various growth factors have been described to aid in nerve regeneration through various mechanisms.[27] Of these, perhaps the class that has received the most attention are the neurotrophins, which act on the high-affinity tropomyosin receptor kinase (Trk) family (part of the tyrosine receptor kinase family) and low-affinity p75 (part of the tumor necrosis factor alpha family) family. NGF acts through its high-affinity receptor TrkA and is known to function mainly by increasing the growth and complexity of sensory neurons both *in vitro* and *in vivo*.[28] BDNF (acting on Trk-B), is crucial for sustained axonal regeneration and myelination, but its role is less clear as high levels of BDNF can lead to apoptosis through the p75 pathway.[29,30] The last neurotrophins, neurotrophin-3 (NT-3) and neurotrophin-4/5 (NT-4/5) act on TrkC and TrkB, respectively. NT-3 has been shown to act as a trophic agent for motoneurons *in vitro*/typ 2b fast muscle fibers *in vivo* and play a role in sensory neuron survival[31–34] while NT-4/5 acts preferentially on slow motor units.[35] The role of the neurotrophins is still being expanded upon,

and for a more complete overview of this class of NTFs, please refer to these excellent reviews.[22,36–38]

Outside the neurotrophin family, many other NTFs play critical roles in nerve regeneration. GDNF, part of the TGFα-1 superfamily, acts on the GFRα-1 receptor and is important as a trophic agent for all types of peripheral neurons: motor, sensory, and autonomic.[39–42] In addition, it has many effects on Schwann cells: it acts as a chemotactic factor for migration, increases myelination of axons, and leads to Schwann cell proliferation.[43] Neuroactive cytokines like interleukin-6 (IL-6), leukemia inhibitory factor (LIF), and CNTF are all found after nerve injury and each play a role in the survival, growth, and myelination of axons following axotomy. There are also various other families of growth factors found to be active in nerve regeneration, including the insulin-like growth factors (IGF-1 and IGF-2), fibroblast growth factors (FGF-2), neuregulins (neu differentiation factor (NDF), acetylcholine receptor inducing activity (ARIA), glial growth factor (GGF), heregulin, among others), pleiotrophin, osteopontin, transforming growth factor-β (TGF- β), and vascular endothelial growth factor.[22]

With the abundance of NTFs known to affect nerve regeneration, it has become evident that the regenerative milieu of growth factors is complex and both spatially and time dependent. Indeed, factors acting in unison can be synergistic, which complicates the known actions of NTFs applied alone.[44,45] As such, techniques to apply both a single NTF and multiple NTFs within nerve conduits will be discussed later, but first the counterpart to the biological influences – namely the physical topographical cues – will be elaborated upon.

1.3.2 Topographical Cues

Uninjured nerves are highly linear in architecture – they organize as bundles and travel across large distances to innervate their end organs. However, the process of nerve regrowth is not so ordered; unguided nerves have very sporadic and curvilinear paths (with direction reversals possible, too) that make the journey to their endplates difficult. As such, guiding axonal extensions has great benefits in improving regeneration speed, accuracy, and decreasing neuroma formation.

Along this line, manipulations in the environment on which nerves regrow have been demonstrated to have significant effects on regeneration.[18,46] As one might expect, when the surface of the substrate has an aligned pattern on the scale of the native extracellular matrix (μm to nm), nerves are able to follow these paths. This can result in highly aligned neurite extensions depending on the alignment of the underlying structure, as demonstrated *in vitro* using dorsal root ganglion (DRG) growth assays.[47,48] Similarly, high degrees of alignment also occur when using channels or other forms of directional control such as microfluidic devices. In addition, changing the stiffness of the substrate or introducing "pillar-like" columns can provide advantages in attachment and migration too.[49]

These physical parameters of the topography are crucial for nerve regrowth, but perhaps equally important is the chemical makeup of the substrate. Hydrophobicity, hydrophilicity, polarity, and presence of functional groups have all been shown to influence growth, attachment, and survival.[11,18,46,50] Indeed, rat pheochromocytoma cells (PC-12) and DRGs have displayed markedly different growth profiles on materials like collagen, laminin, polycaprolactone (PCL), poly-l-lactic acid (PLLA), graphene-oxide incorporated PCL, and silk fibroin. These materials all contain different chemical moieties inherent to their structure, and it is the presence of these that

allow for interactions with growing axons. Thus, many strategies also exist for creating materials that have binding motifs or tethered growth factors to enhance growth. A detailed review of materials utilized in nerve regeneration will not be presented here, but for a look at the breadth of materials available one can refer to comprehensive reviews written on this subject.[11,18,46,50,51]

1.3.3 Cellular Support

In addition to growth factors and materials/scaffolds, the last fundamental element of tissue engineering is cells. Typically, cells are applied with the goal of becoming the functional unit of the engineered or regenerating tissue, whether that be through the use of primary cells or stem cells that differentiate into the epithelial cell type. Within peripheral nerve tissue engineering, however, cells are applied with the goal of augmenting the natural repair process. The implanted cells are thought to act as support cells that secrete growth factors (including NTFs) to recruit host cells (such as macrophages, Schwann cells, and endothelial cells), induce tissue remodeling, increase axonal regenerative rate, and direct axon growth. These cells add a layer of complexity for NTF-based nerve tissue engineering strategies because their secretome contains a multitude of growth factors – some that may not yet be defined – that may play a variety of roles. There are currently many cell types that have been used in this capacity (Figure 5), and they will be discussed in four main groupings: Schwann cells, neural stem cells, pluripotent stem cells, and mesenchymal stem cells (MSCs).

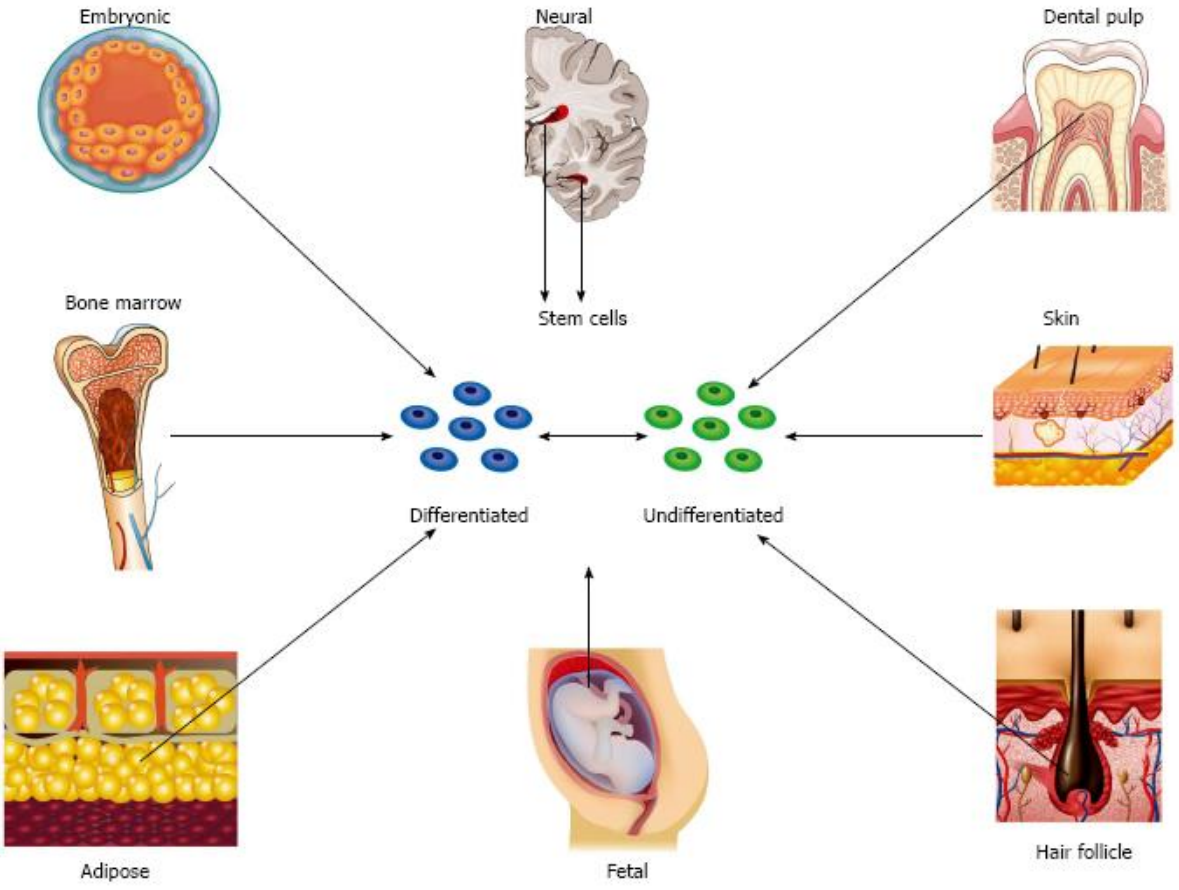

Figure 5. Stem cell sources used for peripheral nerve tissue engineering. Stem cells from the pictured sources are used either as undifferentiated stem cells or are induced to neural lineages before application. Adapted from Fairbairn et al.[52] through the CC BY-NC 4.0 license.

1.3.3.1 Schwann Cells

As the main support cells for peripheral nerves, Schwann cells are seen as a "gold standard" cell type to apply in regenerative treatments. Over the past few decades, many advances have been realized that make their clinical translation feasible – the ability to be isolated from human nerve,[53,54] the capability to be cultured and expanded,[55–58] and finally demonstration of efficacy and safety when transplanted autologously *in vivo*.[59–62] Indeed, there is extensive data that addition of Schwann cells to nerve conduits increases axonal regeneration, myelination, and return of function in various animal models, including non-human primates.[63–66] However, there are still drawbacks to using Schwann cells: namely time and cost. In order to obtain autologous Schwann cells, a donor nerve generally must be harvested to obtain live Schwann cells (such as the sural nerve). After this, they must be cultured and expanded to provide sufficient cell number for transplantation – a step that is lengthy, costly, and still being optimized. Thus, while Schwann cells represent an "ideal" cell type for cell-based augmentation of regeneration, they suffer similar drawbacks as autografts (the need for a second surgical site to harvest the cells) and may increase the amount of time needed before surgical intervention due to cell expansion. Thus, alternate cell sources have been sought out.

1.3.3.2 Neural Stem Cells

Among the alternate cell sources, perhaps the most logical "next step" is neural stem cells (NSCs) given that Schwann cells are derived from the neural crest. These cells are generally isolated from the central nervous system and cultured to form neurospheres *in vitro*. When transplanted *in vivo* with nerve conduits, results varied from larger myelinated axons, increased axonal count, improved functional outcomes (including electrophysiology), and outcomes

similar to autograft or normal nerves depending on gap size.[67–71] In addition, some studies report that these NSCs also differentiate into all neural support lineages: astrocytes, oligodendrocytes, and Schwann-like cells.[69] However, one drawback that remains with these cells (in addition to the need to isolate and culture from the CNS) is that neuroblastoma formation has been reported, which brings to question the safety of this treatment.[72] Thus, although NSCs provide another route for cell application, they suffer from many of the same drawbacks as Schwann cells.

1.3.3.3 Pluripotent Stem Cells

A cell type that addresses some of the limitations of NSCs and Schwann cells while retaining the capability to have augmentation with true neural lineage cells is the pluripotent stem cell. Pluripotent stem cells are those with the ability to differentiate into multiple lineages from different germ layers (for example mesoderm and ectoderm). In this class, embryonic stem cells (ESCs) and induced pluripotent stem cells (iPSCs) have been utilized for peripheral nerve regeneration.[73,74] Differentiation into neural-specific lineages is difficult and few well-established protocols are available, but nevertheless results are similar to those observed from NSCs and SCs.[75–81] In general regeneration is superior (in terms of either function or histological measures) in groups that receive cells, and there is evidence that that ESCs and iPSCs differentiated into NSCs also further differentiate into Schwann cells *in vivo*.[75,81] In addition, ESCs have also been shown to increase neuromuscular junctions and delay muscle atrophy for enhanced motor recovery when injected into the denervated muscle belly.[79] These pluripotent stem cells address the limitation of the need for harvest from limited donor tissue (such as peripheral nerve or CNS structures), but as with all pluripotent stem cell treatments teratoma formation cannot be ruled out. ESCs also have additional drawbacks due to the need for immunosuppression and ethical considerations related to destruction of embryos.

1.3.3.4 Mesenchymal Stem Cells

While the next class of stem cells that will be discussed do not possess the inherent ability to differentiate into ectodermal lineages, they are likely the cell source closest to clinical translation. Mesenchymal stem cells (MSCs) are multipotent cells that are known to be able to differentiate into bone, cartilage, and fat.[82] They have also been shown to be able to adopt a number of other phenotypes, such as muscle and neural-like lineages.[83] MSCs are found in many tissues and sources such as fat, bone marrow, synovium, hair follicle, dental pulp, skin, and blood, and they are found in higher number and easier to obtain than any of the cell sources listed earlier.

Bone marrow stem cells (BMSCs) are isolated from bone marrow and pose little ethical concern for autologous isolation. They have been shown to be able to produce a number of NTFs and differentiate into neural-like lineages (astrocytes, neurons, and Schwann-like cells) under appropriate differentiation conditions and protocols. In general, conduits that employ BMSCs (either pre-differentiated during *in vitro* culture or undifferentiated) experience increases in nerve regeneration outcomes, including greater myelination, larger axons, improved g-ratios, and functional performance too.[84–87] However, there are very few studies that show BMSC application to be superior to autografting when used as a single adjunct treatment to the conduit, but some studies demonstrating non-inferiority have been reported.[88–91] While BMSCs were one of the first MSCs to be described and applied in nerve regeneration, their autologous harvest from bone marrow (an invasive and painful procedure) makes other MSC sources more desireable.

Adipose stem cells (ASCs) are isolated from fat and are one of the easiest autologous MSC sources to obtain given the abundance of fat and high stem cell fraction within the tissue.[92]

Like BMSCs, they have also shown the capability to differentiate among neural lineages, albeit with even greater differentiation and proliferation capacities than their bone marrow counterparts. Again, conduits with supplemented ASCs perform superior to their cell-free versions with few exceptions that describe no benefit.[93–97] Importantly, there has been no demonstrated difference in using ASCs vs BMSCs in head to head comparison studies, and like BMSCs, ASCs have been shown in some studies to be equivalent to or superior to autografting.[98–100] These attributes make ASCs a more clinically relevant cell source than BMSCs given their equivalence in performance coupled with their ease of isolation and high stem cell fraction within the tissue itself.

In addition to the more commonly used MSCs of adult origin, fetal derived stem cells also display the ability to enhance nerve regeneration. Wharton's jelly derived MSCs (WJDSCs), amniotic fluid derived stem cells (AFDSCs), and umbilical cord-derived MSCS (UMDSCs) are three such fetal derived stem cells that have shown success *in vitro* or *in vivo*.[101–106] WJDSCs express NTFs *in vitro* and enhance dorsal root ganglion (DRG) neurite extension while both AFDSCs and UMDSCs have demonstrated successful enhancement of nerve regeneration in *in vivo* sciatic nerve gap models. These fetal cells possess the advantage that they are younger than adult MSCs and have not accumulated genetic damage or become partially senescent due to the natural aging process and environmental stresses. However, autologous use is at the moment not possible due to the need for storage of autologous tissue, and allogeneic use requires immunosuppression.

The last grouping of stem cells discussed here will cover the remaining stem cells of mesenchymal origin that have seen significant application in nerve regeneration: skin derived precursors (SKPs), hair follicle stem cells (HFSCs), and dental pulp stem cells (DPSCs). SKPs

are derived from the dermis and have characteristics reminiscent of embryonic neural crest cells (Schwann cells are derived from neural crest), which make their application appealing in nerve repair.[107] HFSCs display characteristics of neural crest cells as well given the neural crest origin of hair follicles, and HFSCs also exhibit pluripotency factors Nanog and Oct4.[108–110] These cells were found to differentiate into Schwann-like cells *in vivo* and significantly improve functional outcomes when implanted in murine models of nerve transection.[111–113] Lastly, DPSCs derive from deciduous teeth and were shown to differentiate into Schwann cells *in vitro* (dental pulp is also formed from the neural crest).[114] When implanted in rats *in vivo*, they supported axonal regeneration in a central nervous system spinal cord hemisection model.[115,116] These three sources are all readily available and minimally invasive, and present viable alternatives to the commonly used ASCs and BMSCs.

1.3.3.5 Clinical Consideration

Overall, of the cell sources mentioned in this section, MSCs remain the most clinically relevant given their availability, autologous nature, differentiation potential, and high abundance in tissue. In addition, they do not require immunosurpression if used autologously and face few ethical concerns. Of the MSCs, ASCs are the closest to clinical translation because they can be harvested and utilized with minimal manipulation, making their FDA regulatory status less stringent.

1.4 NERVE CONDUIT DESIGN STRATEGIES

Nerve conduit design strategies have evolved over the past few decades to better incorporate and utilize new knowledge about topographical cues, growth factor signaling, and cellular support. In this next section, current techniques to apply these will be discussed, with a focus on incorporation of growth factors and cells to the conduit design. For more information about structural designs for incorporating various topologies, please see the following reviews on the subject matter.

1.4.1 Strategies for Growth Factor Incorporation

As mentioned before, growth factors play an important role in enhancing and maintaining the nerve regeneration process. As such, techniques to control the loading, concentration, distribution, and release profile of these growth factors are constantly being developed.[117] There are at present a few major pathways for including growth factors into conduits: conjugation to the nerve conduit polymer structure,[118] physical interaction with the conduit material (such as electrostatic or specific binding),[119,120] inclusion of growth factor within microparticles,[121] inclusion within a lumen filler (such as a hydrogel material or nanofibers),[122–126] and lastly repeat injection of growth factors (Figure 6). These techniques all afford a degree of control and localization in the delivery process. Conjugation to the polymer can result in low efficiency of

retention of bioactivity for expensive growth factors, but allows for repeat signaling due to the tethered nature of the factor. Physical adsorption of proteins to the polymer is a facile way to introduce growth factor signaling, but usually persistence of these interactions are shorter lived than other methods and they are further complicated by high initial burst release and potential loss of bioactivity/bioavailability. Microparticles allow for a greater degree of control in the temporal release aspect of the growth factor up to weeks and even months, and they can be spatially localized during fabrication within the nerve conduit wall. Lumen fillers also afford the opportunity to another avenue and spatial location to introduce growth factors. These can be mixed in with a hydrogel, electrospun into nanofibers through coaxial spinning, or introduced through a combination of techniques mentioned above to name a few. Lastly, repeat injection of a specified amount of growth factor is possible, but the invasiveness and need for repeat procedures makes it highly undesireable.

Current growth factor incorporation strategies are sophisticated when it comes to releasing one, or a few growth factors. However, a few inherent limitations in these techniques is that incorporation of a multitude of growth factors may be infeasible or cost prohibitive, the initial loading amount sets an upper limit for total amount of available growth factor, and the array of released growth factors cannot differ from those that are loaded. These considerations make it difficult or impossible currently to implement a dynamically changing release profile that can respond to the various signals that may be present within the regenerating nerve environment – some of which may not yet be known or defined. As such, cell seeding presents an attractive adjunct or alternative to achieve growth factor-aided regeneration.

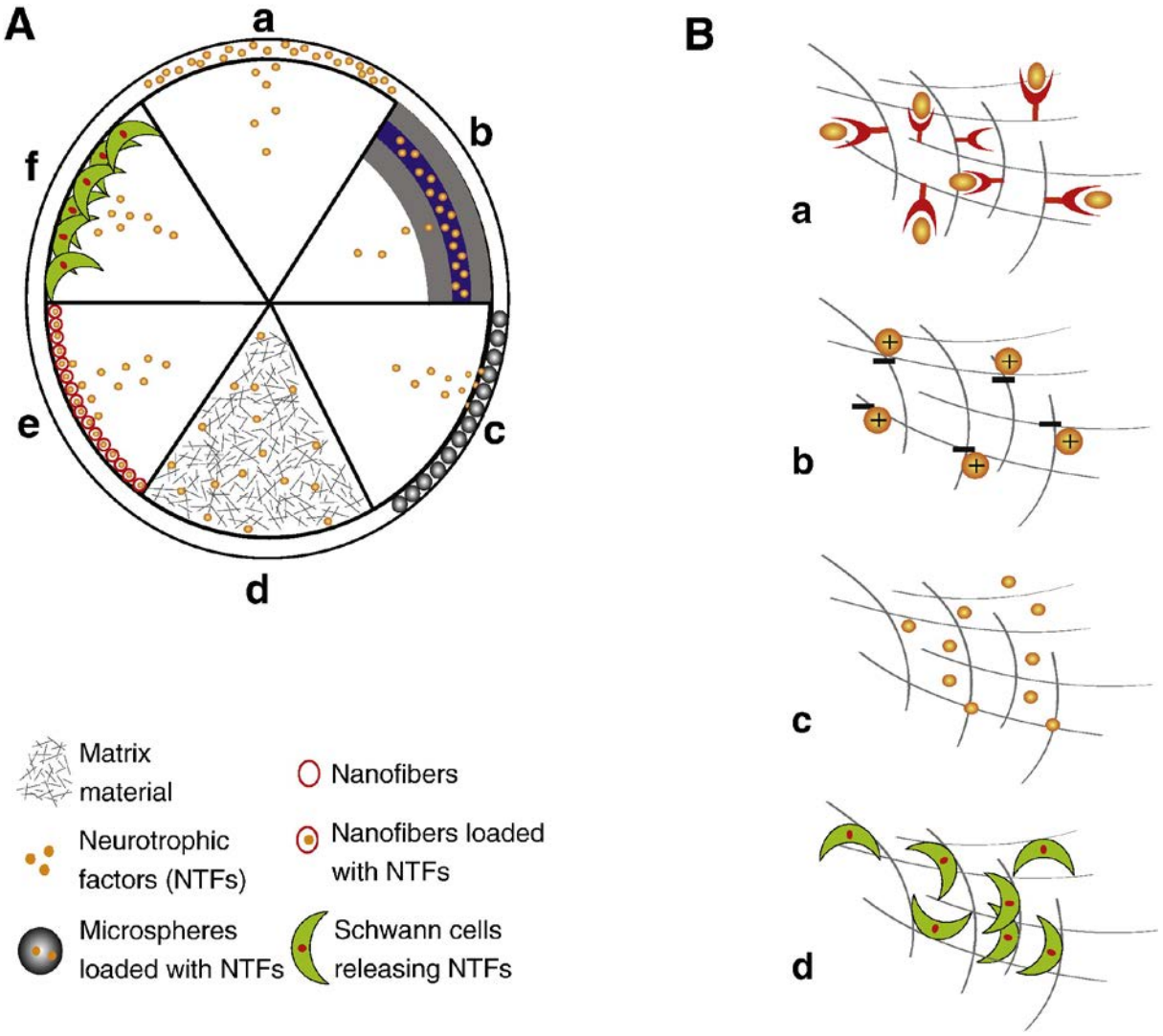

Figure 6. Growth factor delivery systems for nerve conduits. (A) Loading mechamisms for NTF release from nerve conduits. (a) NTFs within the wall polymer material; (b) NTFs within polymer layers coated onto the NC walls; (c) NTFs released from microspheres in nerve conduit walls; (d) NTFs loaded within an ECM conduit lumen filler; (e) NTFs spun within nanofibers on nerve conduit walls; (f) direct release of NTFs from Schwann cells seeded onto the nerve conduit (or other NTF-secreting cells). **(B)** NTF release mechanisms based on (a) binding affinity, (b) ionic interactions, (c) passive diffusion, and (d) cell-secretion. Adapted from Madduri et al.[117] with permission from Elsevier.

1.4.2 Strategies for Cell Incorporation

Cell seeding in nerve conduits is an attractive route to augment the natural nerve regeneration process.[52] However, as with any cell seeding process, there are challenges that must be met to successfully incorporate live cells. Namely, the process must be amenable to survival of the cell. This incorporates osmotic pressures, shear and stress, temperature, oxygen tension, and metabolic factors. Given these constraints, current cell seeding methods for nerve conduits are fall into a few general categories (Figure 7), which will be enumerated in this section.

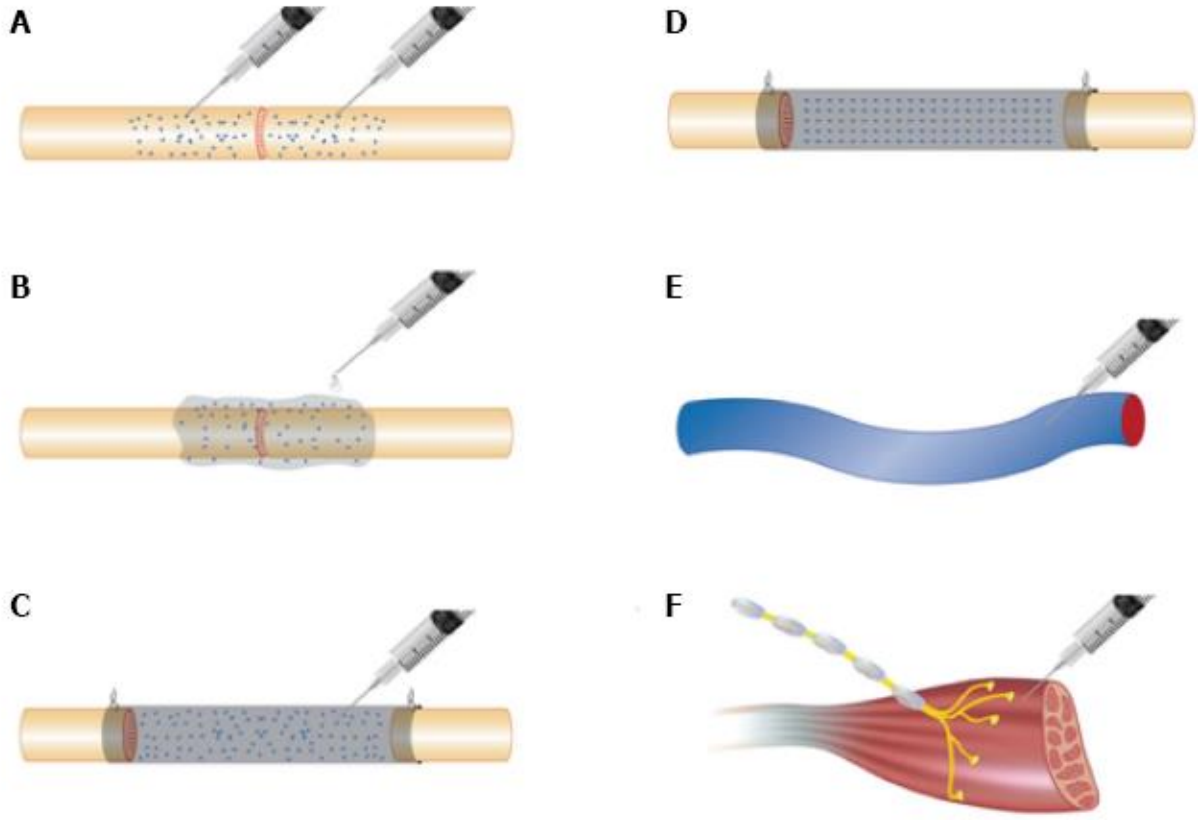

Figure 7. Methods for cellular augmentation of peripheral nerve regeneration. (A) Direct injection into nerve ends after primary repair. **(B)** Application in gel around nerve after primary repair. **(C)** Injection into nerve conduit lumen. **(D)** Seeding onto nerve conduit surfaces in *in vitro* culture before nerve repair. **(E)** Systemic injection. **(F)** Direct injection into muscular endplates.. Adapted from Fairbairn et al.[52] through the CC BY-NC 4.0 license.

Perhaps the most common technique to be applied for cellular augmentation of nerve conduits is direct injection of cells into the lumen.[52] In this method, the severed nerve ends are sutured into the nerve conduit on either end followed by injection of a suspension of cells into the lumen of the conduit. Here, the cells can be suspended in any aqueous carrier, such as salt

solution, cellular growth medium, or polymer. Although this method is the simplest, it does not allow for tight control of cell seeding number due to leakage from the conduit. In addition, spatial restriction or localization within a part of the conduit is also difficult and not currently achieved using this method. However, it still remains one of the most popular methods for introducing cells into conduits.

Another commonly applied technique involves attachment of cells onto the conduit surfaces.[52] Generally this is achieved by placing the fabricated conduit (which may be porous or solid) into a cell suspension in medium to allow for cells to penetrate throughout the scaffold and attach to its surfaces. This technique is generally applied to the whole scaffold by soaking the whole scaffold, which allows little control of cell number or spatial localization within the conduit. Theoretically, localized seeding could potentially be achieved by applying a small volume in a porous conduit at a specific location within the conduit.

The last group of seeding techniques for nerve conduits that will be discussed is polymer-encapsulated cell seeding.[127] Here cells are either suspended within a polymer and formed into a conduit through a mold or they can be 3D printed into the conduit too. Using this process, cells are found in the nerve conduit walls (trapped within polymer) as part of the nerve conduit body. This theoretically also allows for control of both cell density and spatial location, but spatial control has not been implemented yet to the best of this author's knowledge. In addition, for printed conduits where cells are mixed into the polymer conduits generally degrade quickly due to the requirement that it be suitable for cell survival thus possessing a high water content.

It should bear brief mention that besides nerve conduit augmentation, cells have been applied for nerve regeneration in various other methods as well. Direct injection into both the proximal and distal nerve ends or directly into a graft have been reported via

microinjection.[95,96,128–132] However, this can compromise some of the nerve architecture and cell localization is hard to achieve through this method. Another route is systemic injection with the idea that cells home to the site of injury and exert effects there. Lastly, injection into denervated muscle with the goal of targeting the neuromuscular junction has shown some success.

1.5 NERVE CONDUIT REQUIREMENTS

As alluded to earlier, live cell incorporation in nerve conduits faces additional challenges due to physical and biological criteria that the nerve conduit must possess to adequately guide the growing nerve in the *in vivo* environment. Among the conduit physical factors, degradation profile, flexibility, and suture retention strength are necessary for a functioning implant. Studies have shown that the conduit material should maintain structural integrity for at least 4 weeks to protect the growing nerve as well as be flexible so that kinks are not introduced into the channel.[133,134] In addition, sufficient suture retention strength is necessary to hold the conduit in place. On the biological side, the conduit must be biocompatible and not illicit an adverse reaction by the host such as a foreign body reaction. In addition, degradation of the conduit should not release toxic compounds that could either impede regeneration or elicit a host response. These constraints and requirements add an extra layer of complexity to the nerve conduit design process when cell-incorporation during fabrication is desired.

1.6 HYPOTHESIS AND AIMS

The research in this dissertation aims to effect nerve regeneration with the underlying assumption that a biodegradable and bioactivated conduit providing a directional neurotrophic factor (NTF) gradient may provide both structural as well as neurotrophic support for nerve regrowth. This builds on findings that mesenchymal stem cells (MSCs) have the capability to produce strongly neurotrophic factors (NTF) and influence neurite outgrowth. In addition, the immune tolerance, anti-inflammatory effects, and potential for production of a dynamically changing milieu of NTF responding to different stages of nerve regeneration afforded by MSCs make them ideal candidates for cell seeding in scaffolds. We look to harness these capabilities by encapsulating MSCs within electrospun composite scaffolds of various nanostructural complexities, with the ultimate goal of creating autologous cell-seeded scaffolds that can be customized for each patient. If successful, this would be the first time simultaneous cell seeding during fabrication of a nerve conduit will be achieved.

Thus, the overall hypothesis is that a method allowing for spatial localization of neurotrophically competent MSCs in a biodegradable and bioactivated nerve conduit will significantly augment nerve regeneration and allow for a greater regenerative response than classic homogenous/uncontrolled cell seeding distributions. This will be achieved through the following specific aims, which are detailed in the coming chapters:

Specific Aim 1 – Construction and characterization of novel biodegradable nerve conduits with encapsulated NTF-secreting cells.

Specific Aim 2 – Analyze *in vivo* nerve regrowth with NTF secreting spatially localized cell-seeded conduits.

2.0 CONDUITS HARNESSING SPATIALLY CONTROLLED CELL-SECRETED NEURTROPHIC FACTORS IMPROVE PERIPHERAL NERVE REGENERATION

2.1 INTRODUCTION

Peripheral nerve injury (PNI) affects over 300,000 people each year in the United States and is a significant cause of morbidity and lifelong disability despite surgical intervention [2]. Warfighters, in particular, are exposed to higher incidences of PNI due to battlefield injuries, and PNI morbidity leads to reduced military preparedness, early discharge, poor reintegration into civilian life, and has been implicated in higher rates of depression and suicide among these veterans [3,4]. Not only do PNIs cause loss of function and major disability, but they are also a huge economic burden for both the individual as well as society, costing the United States approximately $150 billion annually in healthcare dollars [5].

While there exist innate healing mechanisms for the repair of damaged nerves, complete transection of axons as well as all supporting tissues, termed neurotmesis, is associated with poor outcomes following injury [12]. Currently, the best treatment option for nerve defects is tensionless end-to-end repair given its predictable positive outcomes, but many times this is not an option due to the various conditions that must be met: repair immediately after injury, minimal gap <2.5 mm in length, good blood supply and soft-tissue coverage, and exact alignment of the opposing ends [1,11,16]. Alternative options such as autografting and allografting exist, but are limited by

donor site morbidity (with a chance for neuroma formation at both sites), availability, and immune rejection, with only a 40-50% success rate for the gold standard of autografting. Another promising regenerative route, the use of a biomaterial nerve conduit, demonstrates potential due to reduced neuroma formation, lack of axonal escape, and lack of donor-site morbidity, but is constrained by range (≤3 cm) and low functional recovery rates [18]. Thus, the ability to provide an efficient and effective method towards bridging the gap in nerve regeneration would be a huge step forward in the care of peripheral nerve injuries.

In the pursuit of an effective nerve conduit, many physical and biological strategies have been employed during fabrication [46,50,52,117,135,136]. On the physical side, electrospun nanofibers hold great promise due to their ability to be fabricated with aligned arrangements closely resembling native nerve ECM, and they have demonstrated the ability to guide neurite extensions [46,137–139]. On the biological side, neurotrophic factors (NTFs), such as brain derived neurotrophic factor (BDNF) and vascular endothelial growth factor (VEGF), have been shown to play an important role in facilitating axonal growth, guidance, and survival [22,140–143]. In addition, chemokine gradients are essential in driving Schwann cell migration into the regenerating nerve bridge and axon elongation [144–153]. Current methods of sustained delivery of growth factors by microparticles, along with other technologies, have demonstrated utility in experimental models of nerve repair, but these technologies have not yet addressed the dynamic time course of growth factor production, the use of anti-inflammatory cytokines, or the capability to supply a multitude of growth factors simultaneously or separately [117,136,154,155].

A potential route toward addressing these issues lies in the use of stem cells. Adult mesenchymal stem cells (MSCs) are multipotent cells that have the ability to differentiate into many lineages, including neural-like lineages [82,156]. Early transplantation experiments involving

these stem cells demonstrated that they supported nerve regeneration (originally believed to be due to transdifferentiation to neural lineages but more recently thought to be through production of NTFs), and they have also been shown to possess immunoregulatory functions, which could potentially decrease scar tissue infiltration into conduits and neuroma formation [52,93,157,158]. Indeed, studies utilizing nerve conduits seeded with MSCs reported both larger axons as well as greater amounts of myelination per axon [52].

While cell support demonstrates distinct benefits in conduit-mediated nerve regeneration, cell-seeding protocols typically either involve cell attachment in culture after fabrication, which can be lengthy (clinically undesirable) and potentially result in cell detachment *in vivo*, or injection into the lumen of the conduit, which is susceptible to leakage [52]. In addition, these methods do not allow for precise control of cell seeding number or cellular distribution within the conduit due to the random nature of cell attachment and injection, and the seeded cells are known to migrate out of the conduit, further confounding the dose- and location-dependent effect of the cells. These limitations have led to the inability to effectively produce and harness cell-secreted neurotrophic gradients.

In this study, we aim to overcome these challenges in cell application by allowing for control of spatial distribution and cell density through direct wall-encapsulation of cells during fabrication. We tested the efficacy of this encapsulation system in enhancing peripheral nerve regeneration both *in vitro* and *in vivo* in a rat sciatic transection model. Our *in vivo* results show that spatially restricted cell encapsulation in the implanted engineered conduit leads to improved Schwann cell migration into the nerve bridge and increased functional return compared to controls.

2.2 MATERIALS AND METHODS

All chemicals were purchased from Sigma Aldrich (St. Louis, MO, USA) unless otherwise specified. All procedures were performed according to the guidelines of the Institutional Animal Care and Use Committee at the University of Pittsburgh (Protocol No. 16036308).

2.2.1 Fabrication of Cell-Seeded PCL/GelMA Nerve Conduits

The composite PCL/GelMA scaffold was produced as previously described [143](Figure 8). Briefly, a dual-nozzle electrospinning setup with 14.0% w/v PCL (80 kDa) in 2,2,2-trifluoroethanol and 18% methacrylated-gelatin (GelMA) in 95% 2,2,2-triflurorethanol in water was used to produce random and aligned scaffolds. A 2.0 x 5.5 cm sheet of aligned scaffold and a 2.2 x 5.5 cm sheet of random scaffold was cut for each group, and subsequently exposed to UV irradiation for 30 minutes to sterilize. The aligned scaffold was then overlapped on top of the random scaffold by 2 mm, and approximately 20 μL of photoinitiator solution (8% methacrylated gelatin, 0.3% photoinitiator lithium phenyl-2,4,6-trimethylbenzoylphosphinate (LAP) in HBSS [Gibco, Waltham, MA, USA]) was applied to the overlapped region. This area was then irradiated with a visible light source supplying wavelengths of 395 nm (7202UV395, LED Wholesalers) for 40 seconds to cure the gelatin and bond the two sheets together. Following this, approximately 300 μL of photointiator solution was used to wet both scaffolds. 50 μL of photoinitator solution was then used to resuspend 6 million cells, which were then pipetted in three vertical stripes 1.2 cm apart and equidistant from the horizontal edges of the scaffold. This completed sheet was then rolled up around a hypodermic needle of 1.5 mm diameter, and subsequently photopolymerized with visible light for 2 minutes while rotating on the needle. The

construct was then removed, and 0.95 cm was removed from each end of the tube followed by cutting the remaining 3.6 cm into three 1.2 cm tubes such that the cell stripes fell into the central third of each conduit (2 million cells/conduit). These wall-encapsulated cellular conduits were then placed in culture medium (10% fetal bovine serum (FBS) [Invitrogen, Carlsbad, CA, USA], 1x PSF [Gibco] in Dulbecco's Minimal Essential Medium (DMEM) [ThermoFisher, Waltham, MA, USA]) until surgical implantation.

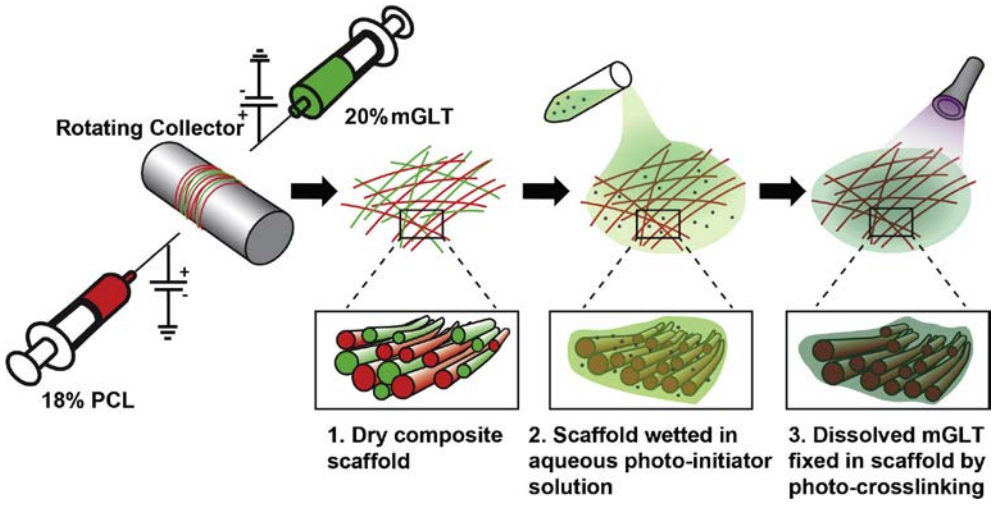

Figure 8. Schematic of fabrication of composite PCL/GelMA scaffold and subsequent cell-seeding procedure.

Adapted from Yang et al.[159] with permission from Elsevier

2.2.2 Cytoskeletal Fluorescent Staining and Calcein-AM Live Cell Staining

Day 8 cell-seeded nerve conduits were carefully unrolled as to not damage the seeded cells, and were washed in PBS, fixed in 4% paraformaldehyde, and incubated with 1% bovine serum albumin (BSA). Subsequently, they were incubated with Alexa Fluor 488 phalloidin (Life Technologies, Carlsbad, CA, USA) for 30 minutes at room temperature. Lastly, the construct was rinsed with PBS, nuclear counterstained with DAPI (Life Technologies), and imaged using an Olympus inverted microscope (Olympus IX81, Center Valley, PA, USA).

Live/Dead viability/cytotoxicity kit (Invitrogen) was used to visualize live cells via Calcein-AM staining, according to the product manual, following cell-seeded nerve conduit fabrication on Day 0. This construct was imaged using an Olympus SZX16 microscope.

2.2.3 Culture of DRG-Seeded Scaffolds on 2-D Cell-Seeded PCL/GelMA Multilayered Constructs

The composite scaffold described above was utilized for the following procedure. A 2.0 x 5.5 cm sheet of aligned scaffold and a 2.2 x 5.5 cm sheet of random scaffold was cut for each group. Approximately 300 μL of photointiator solution was used to wet both scaffolds. Following this, each scaffold was folded lengthwise (along the 5.5 cm side) into halves. The remaining 60 μL of solution was used to suspend 6 million cells, which was applied to the random and aligned scaffolds before folding, and between the scaffolds before the folded aligned scaffold was placed on top of the random one. The 4-layer construct was then exposed to visible light radiation for 3 minutes (1.5 minutes on each side) to photocrosslink the construct. After construction of the

completed multilayer scaffold, three cylinders of 12 mm diameter were punched out with a punch biopsy to yield ~2 million cells/scaffold.

DRGs were harvested from day 9 chick embryos using a previously described protocol [160]. A single DRG was placed on the aligned side of each circular scaffold and placed in a 12-well culture plate. The DRG explant constructs were cultured in basal medium (5% FBS, 1x Pen-Strep [ThermoFisher] in Basal Medium Eagle [ThermoFisher]). Medium changes were performed on days 2 and 4 with 2 mL per well in a 12-well plate.

2.2.4 Immunohistochemistry of DRGs

Cultured DRG explants were rinsed with wash buffer (0.05% Tween 20 in PBS) and fixed in paraformaldehyde for 20 minutes. After three additional rinses with wash buffer, the constructs were placed in 80 °C 10 mM citric acid with 10% ethanol for 1 hour, followed by three washes and subsequent blocking with 5% FBS for 1 hour at room temperature or overnight at 4˚C. After equilibration with wash buffer, anti-neurofilament heavy polypeptide antibody (Abcam, cat. Ab4680, Cambridge, MA, USA) was added at a 1:10,000 dilution overnight at 4˚C, followed by 2-3 washes, and incubation with secondary antibody (goat anti-chicken AlexaFluor 488 conjugated IgG, Invitrogen) at a dilution of 1:300 for 1 hour. The constructs were thoroughly rinsed and then imaged using an Olympus inverted microscope (Olympus IX81) equipped with a motorized stage controlled through MetaMorph (Molecular Devices, San Jose, CA, USA). Resultant mosaic images were stitched using Grid/Collection Stitching (ImageJ, NIH); the 10 longest NEFH-positive neurite extensions were measured from the surface of the original DRG cluster, as previously described [143].

2.2.5 ECM Hydrogel Preparation

Peripheral nerve ECM was prepared from sciatic nerves collected from market-weight pigs (Tissue Source; LLC, Lafayette, IN, USA). The tissue was then frozen for at least 16 hours at -80°C. The tissue was quartered longitudinally and cut into sections of < 5 cm. Decellularization was performed as previously described [161]. Enzymatic degradation products were produced from solid ECM scaffold material as previously described [161]. Enzymatic degradation products were aliquoted and lyophilized. Immediately before use, lyophilized degradation products were rehydrated using sterile water. Gelation was then initiated by adjusting the pH to 7.4 and the solution to 0.5 x PBS concentration through the addition of 0.2 N NaOH and 10 x PBS.

2.2.6 *In Vivo* Scaffold Implantation

For 1 to 6 week experiments, nerve conduits for implantation were either cell-free or wall-encapsulated with rat ASCs, which were DiI-labeled with Vibrant CM solution [Invitrogen) according to manufacturer's protocol. The sciatic nerves in Lewis rats were exposed and a 10 mm segment was removed using microscissors. Nerve stumps were sutured 1 mm into each end of the 12 mm conduit (for a gap of 10 mm) using 8-0 nylon suture. Following implantation, DiI labeled rat ASCs (2 million in 10 μl) were injected into cell-free conduits to represent the cell injection groups, or ECM hydrogel was injected to fill the conduit to represent groups that incorporate hydrogel. A total of n = 6 rats were used for each group for each time point.

2.2.7 Implant Harvesting and Immunohistochemical Analysis

Implants were harvested at specified experimental time points (either 1, 2, 4, 6, or 16 weeks). The harvested implants were then fixed in 10% buffered formalin phosphate for 2 days at 4°C, and then processed through a series of solutions: 10% sucrose for 4 hours at room temperature, 20% sucrose overnight at 4°C, and lastly 30% sucrose overnight at 4°C. After equilibration for 2 hours in Optimal Cutting Temperature gel (OCT) (Sakura Finetek USA, Torrance, CA, USA), 3 samples were transversely cut through the middle of the conduit and frozen-embedded in new OCT cut side down, while 3 other samples were embedded longitudinally in fresh OCT. All samples were stored at -80°C until sectioning. Transverse cryosections with a thickness of 16 μm were collected at every millimeter starting from the center of the conduit, and examined for cell distribution, while the longitudinally embedded samples were sectioned sagittally to assess continuity of nerve growth.

2.2.8 Rat Sciatic Functional Index Testing

Rats were placed in the Motorater System (TSE GmbH, Chesterfield, MO, USA) and acclimated for two days prior to testing. Videos were then recorded for rats walking across the length of the Motorater System. Simi Motion 9.2.1 software (Simi Reality Motion Systems GmbH, Unterschleissheim, Germany) was used to measure toe spread distances from acquired videos. SFI measurements from 4 steps were averaged for each rat.

2.2.9 Immunohistochemistry/Histology of Nerve Conduit Sections and Analysis

Sections were equilibrated in PBS for 10 minutes to remove OCT compound. They were then blocked for one 1h at room temperature with 0.1% Tween-20, 4% Goat Serum (Gibco) in Tris buffered saline (TBS). Following this, primary antibody was applied in block solution and left on overnight. Slides were subsequently washed 3x with 0.1% Tween-20 in TBS wash buffer, and secondary was applied in 0.5% Triton X-100 in TBS for 1h at room temperature. Slides were then washed 3x with wash buffer. Lastly, DAPI stain mixed in 0.5% Triton X-100 in TBS was applied for 10 minutes. After drying, slides were mounted and coverslipped with Vectashield hardset aqueous mounting medium (Vector Laboratories, Burlingame, CA, USA). The following primary antibodies were used: NF160 (1:250, mouse IgG1; Sigma), S100 (1:250, rabbit IgG; DakoCytomation), and Fluoromyelin Red (1:300, Invitrogen). The following secondary antibodies were used: goat anti-rabbit IgG Alexa 488/594/647 (1:220; Invitrogen) and goat anti-mouse IgG1 Alexa 488/594/647 (1:220; Invitrogen). Slides were imaged with an Olympus inverted microscope (IX81). In order to quantify Schwann cells and ASCs within cross-sections, aggregate fluorescent intensity or area was used as a surrogate. Within and between groups, exposure times and thresholding was kept consistent. Fluorescent channels were then analyzed using Fiji (ImageJ) applying over/under thresholding to limit analysis to the positive-staining areas. Myelin thickness and percent myelination was calculated using custom python code reported by Mokarram et al [162]. Briefly, the algorithm designates myelination status if 40% or more of an axon is encircled by Fluoromyelin positive tissue. Myelin thickness is computed using a rotating vector that measures the thickness of the Fluoromyelin positive tissue.

In addition to immunohistochemical analysis, 6 week explants were also analyzed qualitatively for cell infiltration and collagen production using Masson Trichrome stain

(American Master Tech, Lodi, CA, USA) following the manufacturer protocols. Collagen stains blue and nuclei stains red.

2.2.10 Isolation of Rat ASCs

Rat ASCs were harvested and isolated from 8 Lewis rats. First, fat was removed from rats and minced with scissors into fine pieces. These were then digested in 0.1% Collagenase Type 1 (Worthington, Lakewood, NJ, USA), 0.1% Trypsin IIS in HBSS under agitation at 180rpm for 3h at 37°C. The resulting mixture was then filtered through a 100 μm cell strainer. Cells were then pelleted by spinning at 400g for 5 min. Cells were resuspended in growth medium (10% FBS, 1X PSF, DMEM), filtered again through a 100 μm cell strainer, and re-pelleted again. Cells were then counted and distributed to T150 flasks, cultured, and expanded as previously described for human MSCs. Differentiation potential was assessed as previously reported for human MSCs [163]. Growth factor production was measured by ELISA from culture medium of confluent cells over a course of 48 hours.

2.2.11 Human Bone Marrow Stem Cell Isolation

hBMSCs were isolated from the femoral heads of patients undergoing total joint arthroplasty with IRB approval (University of Washington and University of Pittsburgh), and cultured and expanded as previously described [163]. Briefly, bone marrow was flushed out from the trabecular bone of the femoral neck and head using an 18-gauge needle and re-suspended in DMEM. The suspension was filtered through a 40 μm strainer and the flow-through was centrifuged at 300*g* for 5 min. After the supernatant was discarded, the cell pellets were re-suspended using growth

medium (GM, α-MEM containing 10% FBS, 1X PSF, and 1.5 ng/mL FGF-2 (RayBiotech, Norcross, GA, USA)), and then plated into 150 cm^2 tissue culture flasks at a density of 20,000-40,000 nucleated cells/cm^2, and medium was changed every 3 to 4 days. Once 70% to 80% confluence was reached, cells were passaged.

2.2.12 Generation of iMPCs

iMPCs were obtained as previously described [164]. Briefly, induced pluripotent stem cells (iPSCs) were derived from human adult bone marrow MSCs. iMPCs were derived from iPSCs by culturing on Matrigel (Corning, Corning, NY, USA) coated plates in mTeSR1 media (Stem Cell Technologies, Vancouver, Canada).

2.2.13 Neuroinductive treatment for MiMPs and MSCs

Cells were cultured on gelatin-coated flasks and maintained to approximately 70% confluency in normal MSC growth medium. Once cells reached 70% confluency, neuroinductive pre-treatment – 24 hours incubation in pre-treatment 1 medium (α-MEM, 10% FBS, 1X PSF, 1mM β-mercaptoethanol) was started. After 24 hours, medium was changed to pre-treatment 2 medium (α-MEM, 10%FBS, 1xPSF, 1mM β-mercaptoethanol, and 35ng/ml all-trans retinoic acid [RA]) every 24 hours for the next 48 hours. After a total of 72 hours in pre-treatment, culture medium was changed for neuroinductive medium (NIM) (DMEM/Ham's F-12 medium (ThermoFisher), 5% FBS, 1X PSF, 6 ug/ml all-trans RA, 10 ng/ml interleukin-1β (IL-1β; Peprotech, Rocky Hill, NJ, USA), 10ng/ml FGF, 20 ng/ml epidermal growth factor (EGF; Peprotech), 1X B-27 supplement (ThermoFisher), 0.5mM 3-isobutyl-1-methylxanthine (IBMX), 5 ng/ml platelet

derived growth factor (PDGF; Peprotech), 10 uM Forskolin, 50 ng/ml recombinant human neuregulin (hNRG1; R&D Systems, Minneapolis, MN)). This medium was then changed every 72 hours for a total of 2 medium changes for the duration of the NIM treatment. Conditioned medium for ELISA analysis was collected by culturing scaffolds in growth medium (10% FBS, 1X PSF, DMEM) for 2 days after NIM treatment.

2.2.14 Synthesis of Methacrylated Gelatin

15 g gelatin (type B) was dissolved in 500 mL water and placed in a 37° C shaker at 106 rpm for 2h or until dissolved. Subsequently, 12 mL methacrylic anhydride was added to the solution and it was placed back into the shaker overnight. The resulting solution was dialyzed against deionized water using 2000 NMWCO dialysis tubing for a total of 48 hours with at least 10 water changes. This was then frozen and lyophilized to obtain a foamy solid.

2.2.15 Synthesis of Photointiator LAP

The visible-light sensitive initiator lithium phenyl-2,4,6-trimethylbenzoylphosphinate (LAP) was synthesized as described by Fairbanks et al [165].

2.2.16 Scanning Electron Microscopy (SEM)

Nanofiber scaffold surfaces were examined by scanning electron microscopy (SEM, field emission, JEOL JSM6335F) operated at 3 kV accelerating voltage and 8 mm working distance.

2.2.17 Suture-retention test

Nerve conduits were fabricated as described in *Fabrication of Cell-Seeded PCL/GelMA Nerve Conduits*. A 4-0 Vicryl suture was passed through the walls of the conduit 1mm from the ends to generate a total of 2 loops (positioned across from each other when looking into the conduit lumen) at each end of the conduit. The two loops on either side of the conduit were secured to clamps on a material testing machine (Instron, Model 4502, Norwood, MA) and loaded under tension in a direction parallel to the length of the conduit. Conduits were preloaded to 0.4N and stretch was applied at a rate of 7.5 mm/sec.

2.2.18 Cellular Metabolism Assay

Over the course of 28 days, cell metabolic activity was assessed in wall-encapsulated cellular conduits with CellTiter 96® AQueous One Solution Cell Proliferation Assay [3- (4,5-dimethylthiazol-2-yl)-5-(3-carboxymethoxyphenyl)-2-(4-sulfophenyl)-2H-tetrazolium, inner salt; MTS, Promega, Madison, WI, USA]. The constructs with cells were cultured with MTS solution for 4 h, and absorbance at 492 nm was measured using a microplate reader (BioTek, Winooski, VT, USA).

2.2.19 Degradation Analysis

Cell-free conduits were placed in PBS at 37°C for up to 28 days. Conduits were weighed every 7 days after vacuum drying to determine mass loss.

2.2.20 Gene Expression of Various Topographies

2D random and aligned groups were made by seeding cells on top of multilayered constructs consisting of entirely random or aligned composite scaffold. 3D random, aligned, and random/aligned groups were produced by seeding cells within the multilayered scaffolds (fabrication described earlier in *Culture of DRG-Seeded Scaffolds on 2-D Cell-Seeded PCL/GelMA Multilayered Constructs*). In this experiment, 2D and 3D refer to the environment the cell experiences. These groups were cultured in growth medium (10% FBS, 1X PSF, DMEM) and gene expression was assessed on Day 3 and Day 7.

2.2.21 Analysis of Gene Expression by Real Time Reverse Transcription PCR (RT-PCR)

Total RNA of the cells within constructs was isolated by homogenizing in TRIZOL reagent (Invitrogen) and purified using RNeasy Plus Mini Kit (Qiagen, Germantown, MD, USA). Reverse transcription was achieved using SuperScript® VILO™ cDNA Synthesis Kit (Invitrogen) according to the manufacturer's protocol. Real-time PCR was performed using the SYBR Green Reaction Mix (Applied Biosystems, Foster City, CA, USA) with a StepOne-Plus thermocycler (Applied Biosystems). Gene expression levels of BDNF and VEGF were analyzed with primers purchased from Qiagen. All sample values were normalized to 18s rRNA using the $2^{-\Delta\Delta Ct}$ method.

2.2.22 ELISA

ELISAs were performed for human VEGF, BDNF, TGF-β, and IL-6 using DuoSet ELISA kits (R&D Systems). The same factors were assayed in from rat ASCs using PicoKine ELISA kits (BosterBio, Pleasanton, CA, USA). ELISA for induced vs non-induced cells within conduits was performed on conditioned medium from 2 days culture of conduits.

2.2.23 Slow Release of VEGF from Multilayered Scaffolds

2D multilayered scaffolds were fabricated as discussed in *Culture of DRG-Seeded Scaffolds on 2-D Cell-Seeded PCL/GelMA Multilayered Constructs* with the addition of VEGF into the photoiniator solution to yield a total amount of 10 ng per scaffold. Medium was completely changed between consecutive ELISA measurements of VEGF release.

2.2.24 Analysis of Cellular Movement in Conduits *in vitro*

Nerve conduits with wall-encapsulated cells were fabricated as described in *Fabrication of Cell-Seeded PCL/GelMA Nerve Conduits*. Cells were labeled with DiI prior to incorporation in scaffolds. These were cultured in growth medium (10% FBS, 1X PSF, DMEM) until their timepoints where they were fixed, embedded in OCT, and sectioned longitudinally. Images were obtained using an Olympus SZX16 microscope.

2.2.25 Statistical Analysis

All data were expressed as mean ± standard error of measurement (SEM). Statistical analysis was carried out in Prism 7 (GraphPad, Software, La Jolla, CA, USA). All analyses were performed using ANOVA with Tukey's HSD post-hoc testing unless specified otherwise. One-tailed Mann-Whitney testing was used to determine differences in distributions, and non-linear fitting was used to determine Gaussian and quadratic fitting. One-way ANOVA followed by Fishers LSD post-hoc testing against wall or control was used for Week 6 Schwann and myelin thickness/ratio, respectively. A threshold of $p<0.05$ was used to determine statistical significance.

2.3 RESULTS

2.3.1 Multilayered Nanofibrous Nerve Conduits Possess Suitable Physical Properties for *in vivo* Implantation

In order to achieve cell-friendly seeding during fabrication, we employed the combination of electrospun composite nanofibrous mats of co-spun polycaprolactone (PCL) and gelatin methacrylate (GelMA) with both random and aligned fibers for suture retention and neurite guidance, respectively (Figure 9A, Step 1). Gelatin, the denatured form of collagen, is derived from native extracellular matrix, and GelMA has been widely used for the fabrication of hydrogels by virtue of its ability to be photopolymerized as well as its excellent biocompatibility [166]. Despite the hydrophobicity of PCL, the presence of GelMA within the nanofiber mat allowed it to readily incorporate aqueous solutions, which instantly dissolved the GelMA and allowed for immediate seeding of cells onto and between the PCL fibers [159]. Of note, hydration of the composite scaffolds did not change the underlying random *versus* aligned architecture (Figure 10). Using this technique, we created bonded tubular structures resistant to delamination [159] with cells encapsulated within the walls and separated from the lumen of the conduit by bonding the two layers, applying cells in a GelMA solution (shown here as homogenous but could be in any spatial pattern), and rolling around a hypodermic needle of desired diameter (Figure 9A, steps 2-4).

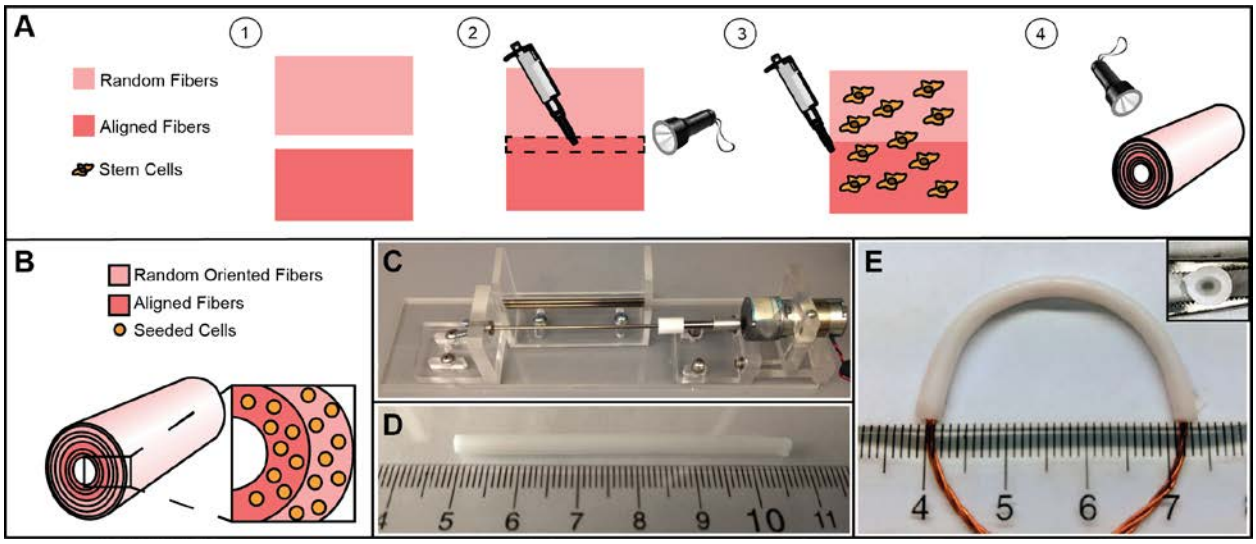

Figure 9. Construction of nerve conduits with wall-encapsulated cells. (A) Stepwise representation of process. (1) Composite random and aligned PCL/GelMA scaffolds are (2) overlaid and bonded with photointiator solution. (3) The rest of the scaffold is hydrated with photoinitiator solution, and cells are placed on the scaffold (homogeneous seeding is shown here but other seeding approaches are also achievable). (4) The sheet is rolled around a hypodermic needle of desired diameter and cured with visible light to bond layers. **(B)** Schematic of completed conduit – layers are removed in magnified view for clarity. **(C)** Prototype machine used to construct scaffold consisting of a slow-rotating motor, a platform, and hypodermic needle. **(D)** Macroscopic view of 5.5 cm long conduit. **(E)** Flexibility of conduit at 15.8 mm radius of curvature. Inset: conduit retains patency after full compression.

The resulting structure was then cured with visible light, to form a multilayered tube with cells localized between every layer (Figure 9B). Figure 9C depicts a simple apparatus suitable for construction of this structure (Figure 9D), with a more complex but user-friendly design in Figure 11. The conduit was elastic and flexible (Figure 9E) – shown at a radius of curvature of 15.8 mm, the smallest radius experienced under physiological human conditions at the cubital tunnel [167]– and after full compression of the lumen it retains patency (Figure 9E, inset).

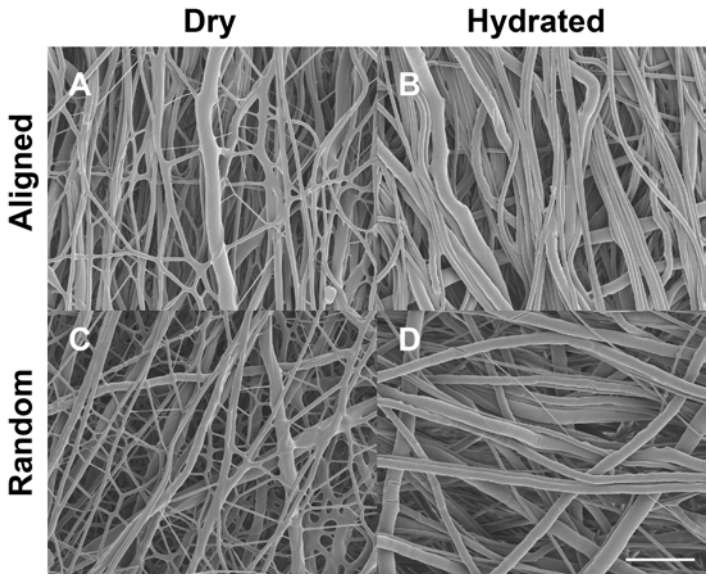

Figure 10. SEM images of composite PCL/GelMA electrospun scaffolds. SEM images of **(A)** aligned composite scaffold, **(B)** aligned scaffold with GelMA removed, **(C)** random composite scaffold, and **(D)** random scaffold with GelMA removed. Note the general retention of aligned and random architecture following hydration and removal of the GelMA sacrificial fiber. Scale bar = 10 μm.

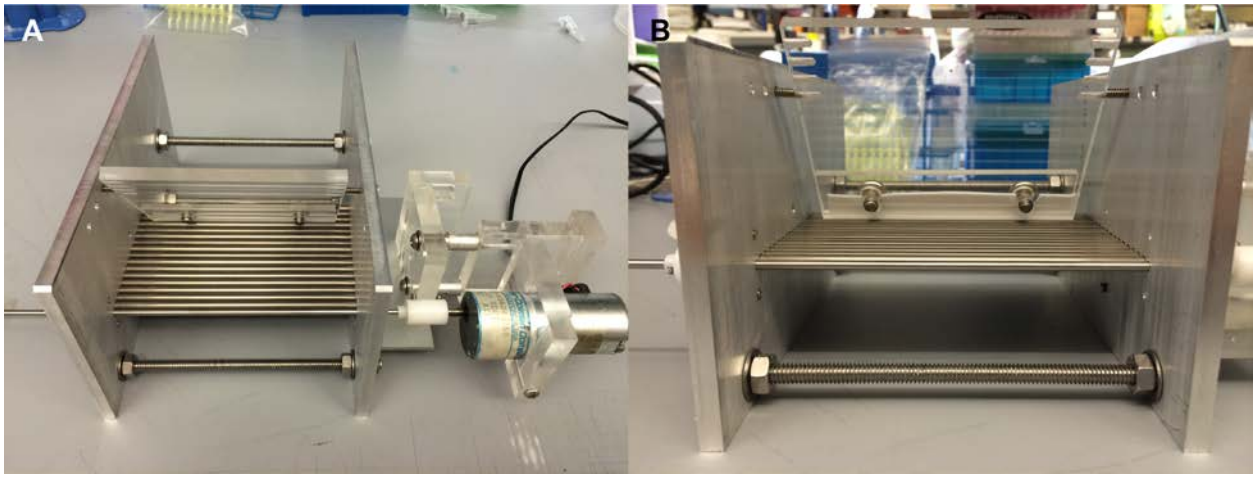

Figure 11. Machine designed to fabricate conduits with wall-encapsulated cells. (A) Top-down view of machine. **(B)** Head-on view of machine showing winding tube in front. The machine has three major components: a slow rotating motor, a winding tube (hypodermic needle of desired diameter), and a platform for the hydrated scaffold to move on. See 83 for design files.

In addition, conduits possessed suitable mechanical tensile suture retention strength (far exceeding the necessary 1.7 N [168–170]), and experienced conduit elongation rather than suture pull-through (Figure 12).

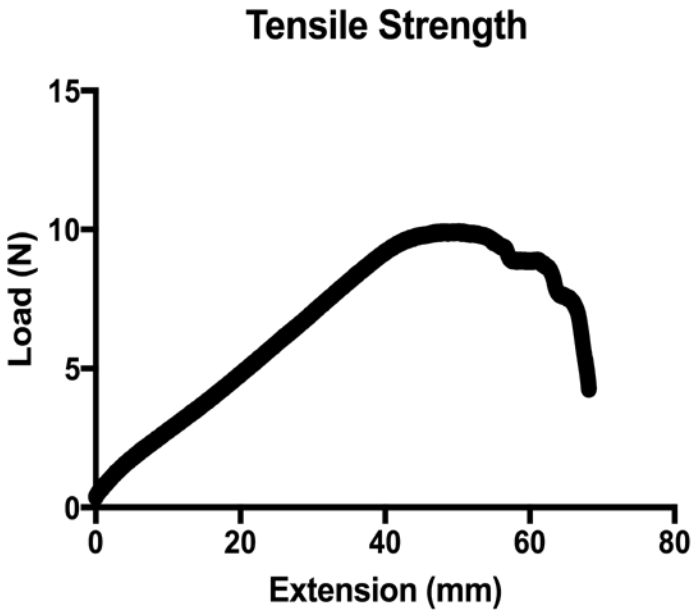

Figure 12. Suture retention strength of nerve conduit. A representative force-strain curve is depicted. Suture retention strength of the conduit was determined by applying tensile load through suture attachments to the conduit. A maximum of 10N was applied before the conduit elasticity was overcome. Instead of suture pull-through, the conduit stretched indicating sufficient suture retention capabilities.

Lastly, as expected, the properties of the conduits were consistent with the composition of a faster degrading GelMA component and slower-degrading PCL component, to avoid conduit collapse during the regeneration process (Figure 13).

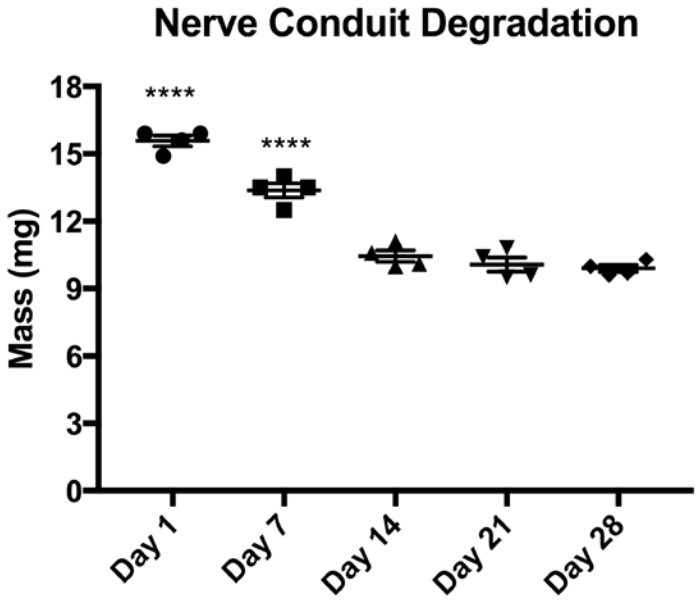

Figure 13. Nerve conduit degradation over 28 days. The graph depicts the dry mass of conduits over 28 days in PBS. The faster degrading component which is mostly gone by 14 days is GelMA, as expected, with the slower degrading PCL component remaining. ****, $p<0.0001$ compared to all other groups.

2.3.2 Nerve Conduits with concentric wall-encapsulated cells possess topographical cues, biological activity, and significantly enchance dorsal root ganglion (DRG) extension *in vitro*

Having established the physical suitability of the conduit for surgical manipulation and implantation, we sought to characterize the biological capabilities of this scaffold. In order to determine the effect of nanostructural cues, phalloidin staining was used to visualize the cytoskeletons of the seeded cells (Figure 14A-D). Figure 14 depicts the major cell morphologies and their spatial distribution within the nerve conduit. Three distinct cell populations were apparent: cells with randomly oriented processes, elongated aligned cytokeletons, and those with short retracted processes (Figure 14B-D, respectively). These cell morphologies corresponded to three microarchitectures of the biomaterials in the scaffold: random fibers, aligned fibers, and thin hydrogel between the PCL layers. Upon live staining with Calcein AM (Figure 14E), live cells were observed to exhibit a concentric distribution, further confirmed by visualizing DiI-labeled cells in cross-sections of the construct, showing their continuous concentric distribution between all layers **(**Figure 14F,G). Increased metabolic activity was also observed over the course of 28 days of culture, indicating cell proliferation and biomaterial biocompatibility (Figure 15).

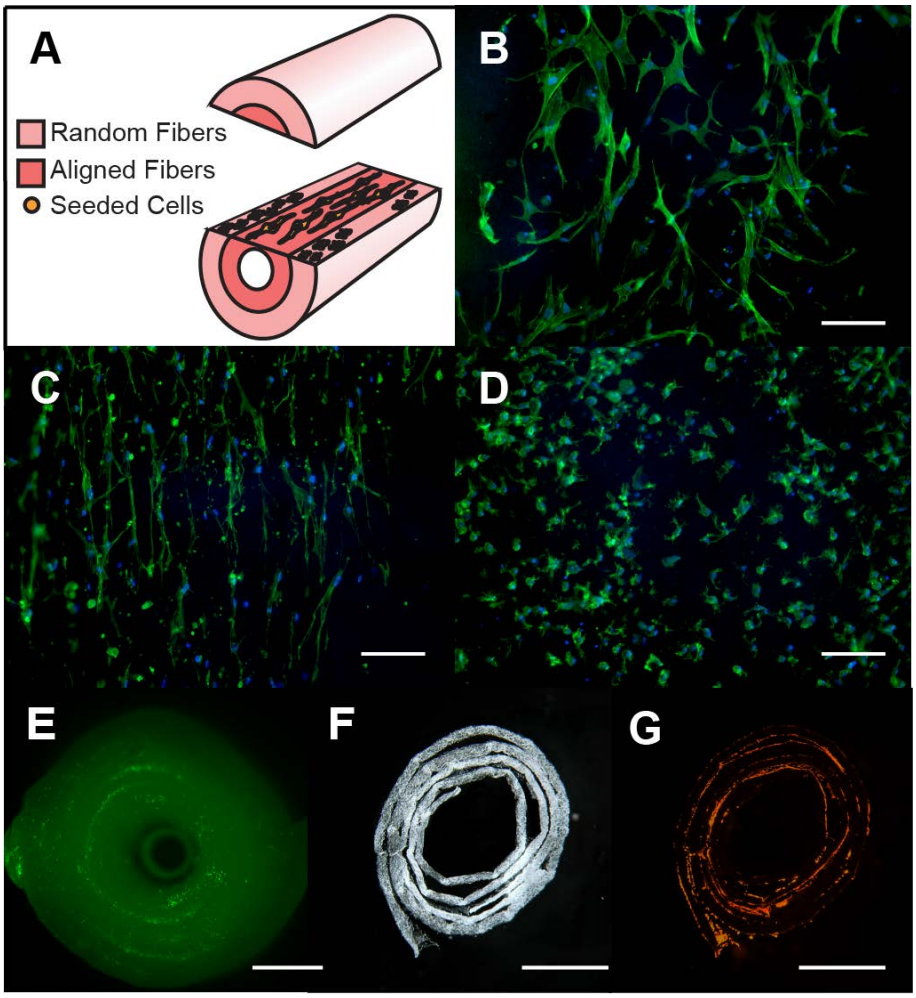

Figure 14. Cells seeded in conduit respond to topographical cues and are concentrically distributed. (A) Location of aligned and randomly oriented cells in conduit. **(B)** Cells with randomly oriented processes on random fibers. **(C)** Cells with aligned processes on aligned fibers. **(D)** Cells with short retracted processes in thin hydrogel layer between fiber layers. **(E)** Live cells are found to be concentrically distributed in conduit by Calcein-AM staining. **(F)** Transverse section of conduit demonstrating close adherence of layers without the use of suture or additional bonding agents. **(G)** DiI-labeled cells are clearly shown to reside between concentric fiber layers of sectioned conduit in **F**. Scale bar: 50 μm (B-D), and 500 μm (E-G).

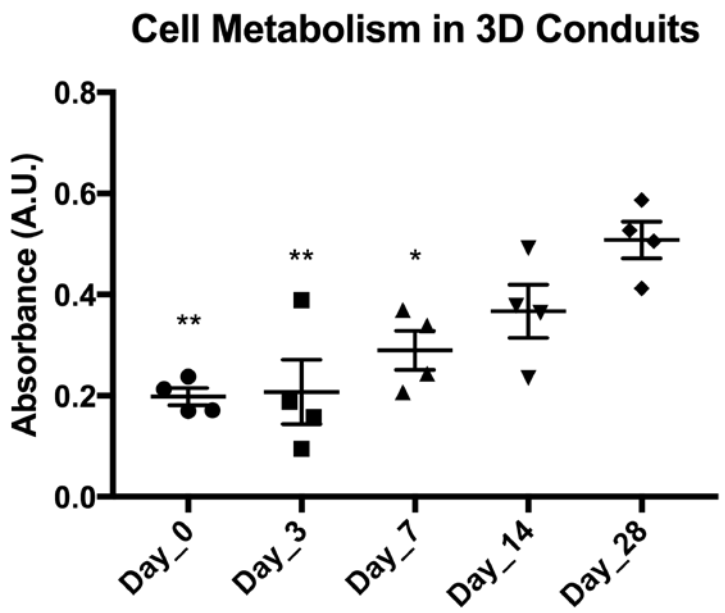

Figure 15. MTS assay of nerve conduit with wall-encapsulated cells over 28 days. The graph depicts the cellular metabolism of cells in the conduit as measured by MTS assay. Over 28 days metabolism increases, hinting at proliferation and biocompatibility. *, $p<0.05$ compared to day 28. **, $p<0.005$ compared to day 28.

In view of the importance of NTFs in nerve regeneration, we were particularly interested in the neurotrophic capabilities of the nerve conduit, particularly the effect of the conduit architecture on NTF production. Our results showed robust gene expression of BDNF and VEGF (two NTFs known to be produced by MSCs in abundance [140,143]) (Figure 16), and that seeded cells produced neurotrophic factors that permeated throughout the scaffold and were measureable by ELISA (Figure 17A). In addition, the GelMA hydrogel component of the scaffold itself showed capability as a delivery vehicle for loaded NTFs (Figure 17B).

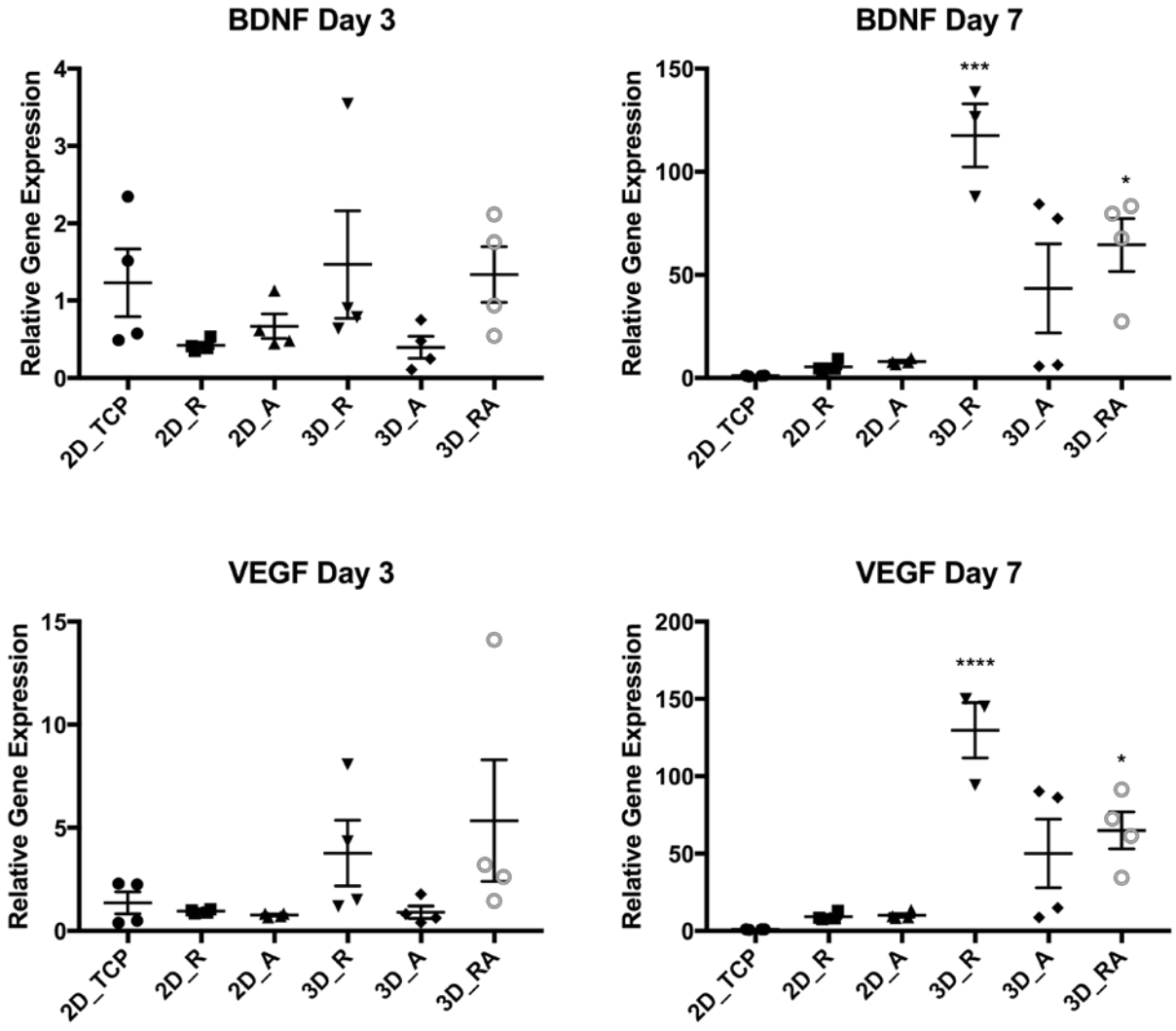

Figure 16. RT-PCR analysis of BDNF and VEGF gene expression of MSCs exposed to various 2D and 3D architectures over 7 days. All gene expression levels are normalized to culture on 2D tissue culture plastic (2D_TCP). No significant differences are found at day 3, but by day 7 3D architectures show a significant upregulation in neurotrophic gene expression. 2D_R, 2D random nanofibers. 2D_A, 2D aligned nanofibers. 3D_R, 3D multilayered scaffold with random nanofibers only. 3D_A, 3D multilayered scaffold with aligned nanofibers only. 3D_RA, 3D multilayered scaffold with half aligned and half random layers. *, $p<0.05$ compared to all 2D groups. ***, $p <0.001$ compared to all 2D groups. ****, $p < 0.0001$ compared to all 2D groups.

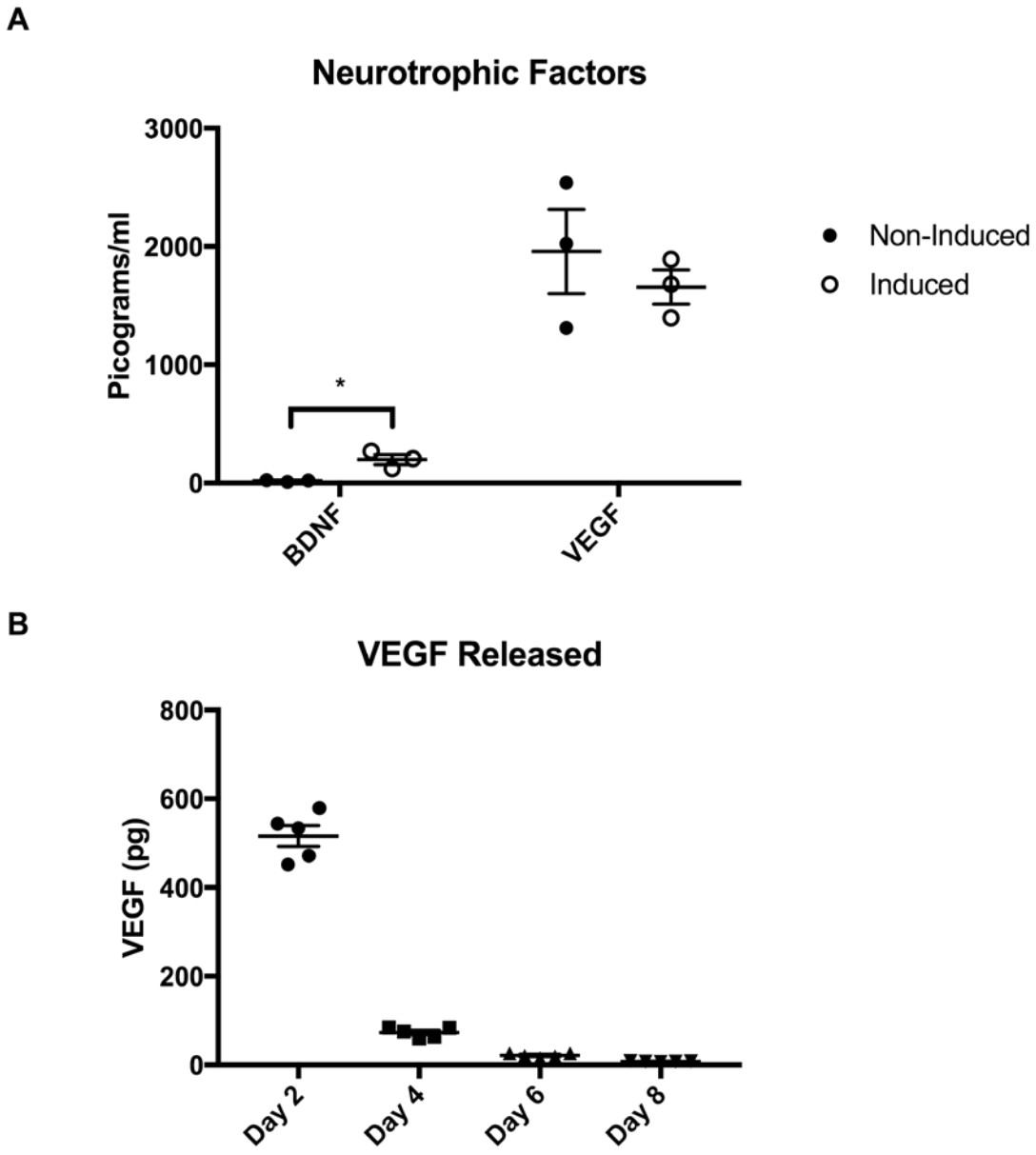

Figure 17. Neurotrophic factor release from nerve conduits with wall-encapsulated cells and cell-free conduits. (A) ELISA for BDNF and VEGF in medium of cultured nerve conduits with wall-encapsulated human bone marrow MSCs (neurotrophically induced and non-induced). **(B)** VEGF released into medium from nerve conduits fabricated with 10 ng growth factor mixed into the aqueous GelMA component. Note the potential for the aqueous phase to be used to deliver neurotrophic factors. *, $p<0.05$.

To assess the effect of the conduit on neurite outgrowth *in vitro*, chick embryonic DRG explants were cultured for 5 days on a 2-dimensional equivalent of the 3-D conduit for easy visualization, and neurite outgrowth was assessed by measuring and averaging the length of the 10 longest neurite extensions measured from surface of the original DRG cluster (Figure 18). Two different mesenchymal cell sources were used for cell seeding, bone marrow MSCs (BMSCs) and induced mesenchymal progenitor cells (iMPCs). iMPCs were derived from induced pluripotent stem cells (iPS cells), as described previously,[143] and were included to demonstrate versatility in terms of cell sourcing and cell incorporation into the nerve conduit using the procedure described here. These two cell types were also exposed to well-defined neurotrophic induction protocols described by our lab and others to optimize neurotrophic gene expression and inductive activity for neural-like differentiation [143]. As seen in Figure 18A, all groups with seeded cells significantly increased DRG neurite extensions compared to cell-free controls ($p<0.0001$). In addition, neurotrophically induced BMSCs (I_BMSCs) producing higher levels of BDNF (Figure 17A**)** significantly increased neurite extension length over uninduced BMSCs ($p<0.005$). Figure 18B-D depict representative images of control, I_BMSCs, and I_iMPCs. These results correlate well with our previous observation that neurotrophic factors found in the conditioned medium of cultured BMSCs and iMPCs could significantly increase DRG neurite length [143]. Taken together, these findings showed that conduits with wall-encapsulated cells displayed spatially and topographically specific cues and neurotrophic activity, indicated by significant enhancement of DRG neurite extension *in vitro*.

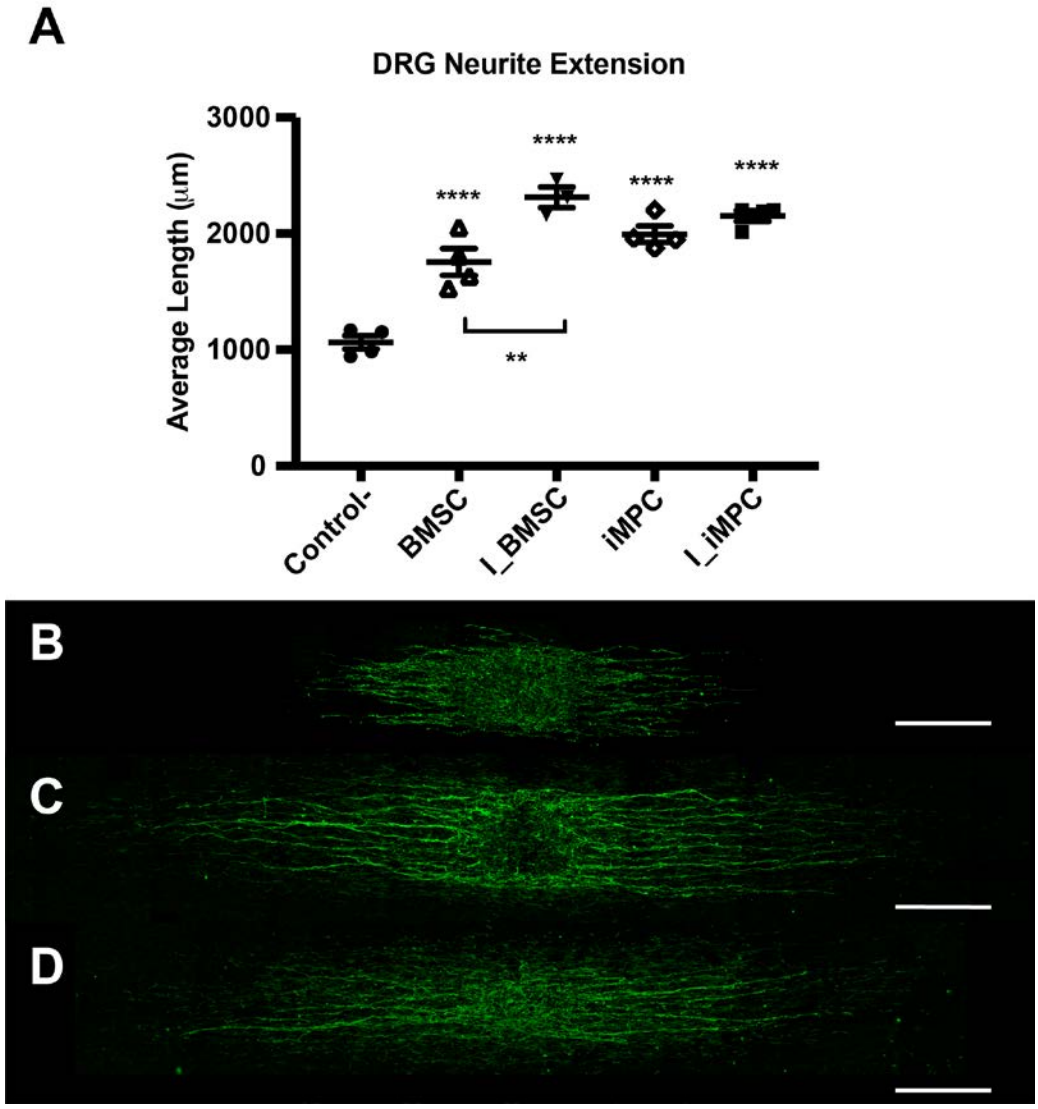

Figure 18. Wall-encapsulated cells significantly increase DRG neurite extension. (A) Average length of 10 longest DRG neurite extensions when cultured on scaffolds containing various wall-encapsulated cells. **(B-D)** Representative images of Control, I_BMSC, and I_iMPC groups, respectively. Control, cell-free multilayer scaffold; BMSC, human bone marrow stem cell; I_, neurotrophically induced; iMPC, mesenchymal progenitor cell derived from iPSCs. **, $p<0.005$, and ****, $p<0.0001$, compared to Control. Scale bar: 500 μm.

2.3.3 Cell Localization Follows Different Distributions in Wall-Encapsulation vs. Injection Methods *in vivo*

Given the effectiveness of the conduit system *in vitro*, we sought to test its *in vivo* characteristics – specifically its ability to control the spatial distribution of seeded cells. In the *in vivo* studies, to minimize xenogenic and allogeneic immune response, we chose to harvest and use adipose stem cells, a readily harvested MSC type, from Lewis rats, which were first analyzed and verified for their differentiation potential and production of growth factors of interest, such as interleukin-6, transforming growth factor-β (TGF-β), BDNF, and VEGF (Figure 19).

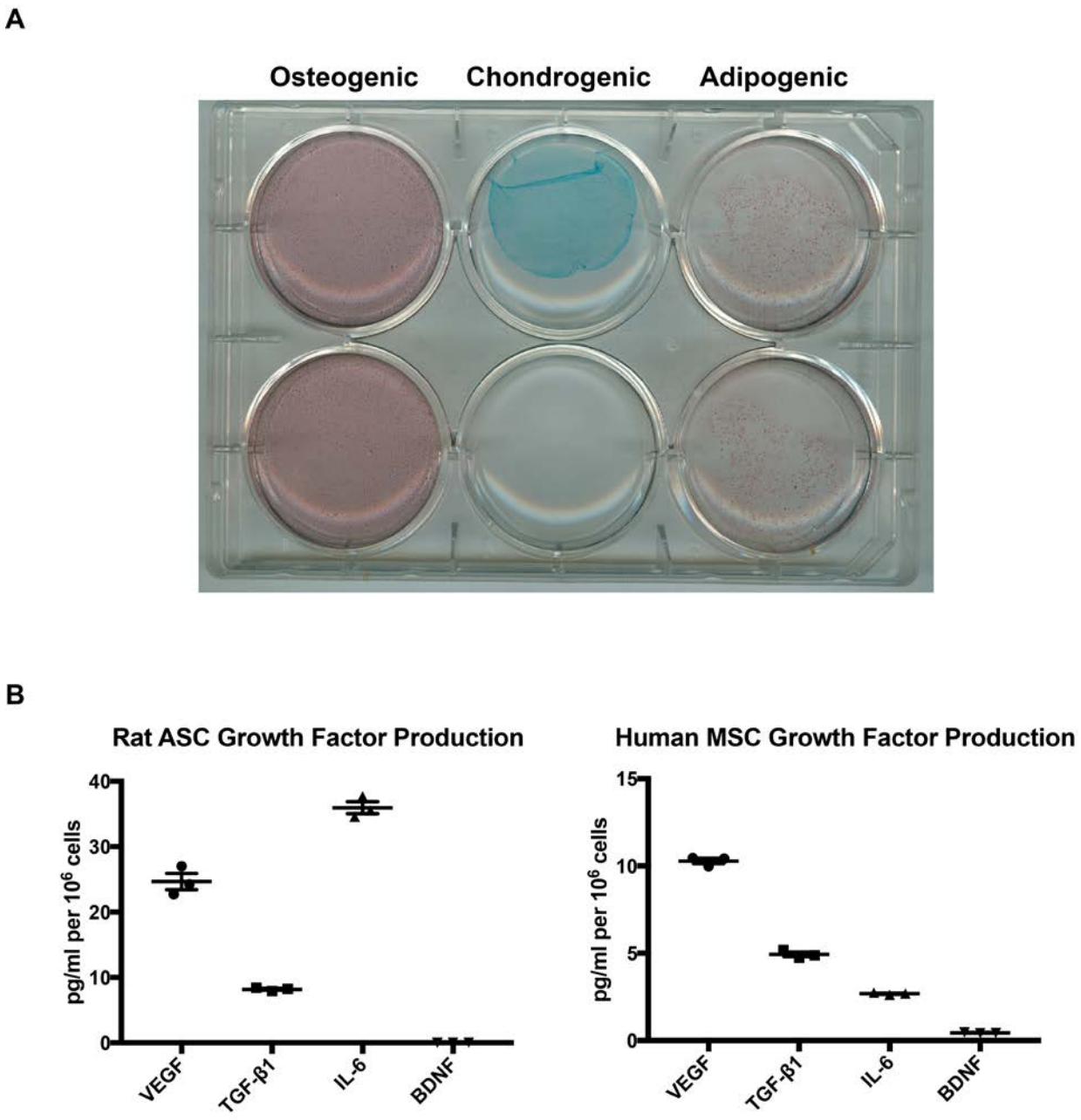

Figure 19. Characterization of differentiation potential and growth factor production of harvested rat ASCs. (**A)** Alizarin red, Alcian blue, and Oil Red O staining after culturing in medium to promote osteogenic, chondrogenic, and adipogenic differentiation of ASCs. **(B)** ELISA to compare VEGF, TGF-β1, IL-6, and BDNF in rat ASCs (used *in vivo*) and human bone marrow MSCs (used *in vitro*). The harvested ASCs were negative for BDNF.

The ASCs were DiI-labeled and used to assess the extent of cell migration, first queried *in vitro* upon wall encapsulation within the central third of the length of the nerve conduit. Over the course of two weeks, minimal migration from the center was observed and cells were retained within the walls of the conduit (Figure 20).

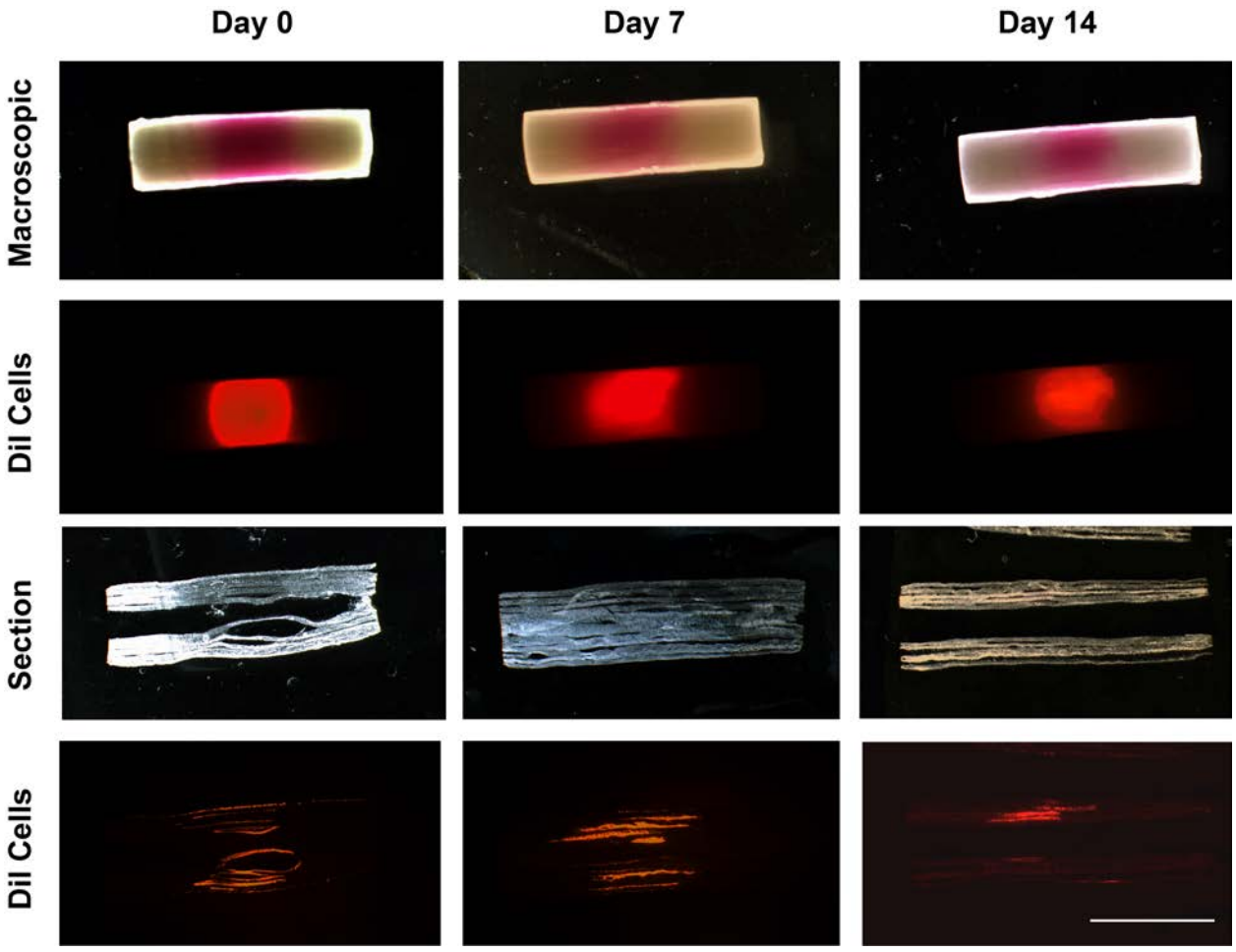

Figure 20. Qualitative assessment of cell migration in nerve conduits with wall-encapsulated cells *in vitro*. DiI-labeled cells were encapsulated in conduits and cultured for 7 or 14 days. It can be seen that both macroscopically and in sections, DiI labeled cells seem to be retained near site of original seeding over the course of two weeks. Scale bar = 5 mm.

Conduits with the same design (DiI labeled ASCs encapsulated within the central third of the conduit) were then implanted allogeneically into Lewis rats in a 1 cm sciatic nerve transection model (Figure 21), along with another cohort of rats that received cell-free conduits and a lumen injection of DiI labeled ASCs of the same quantity.

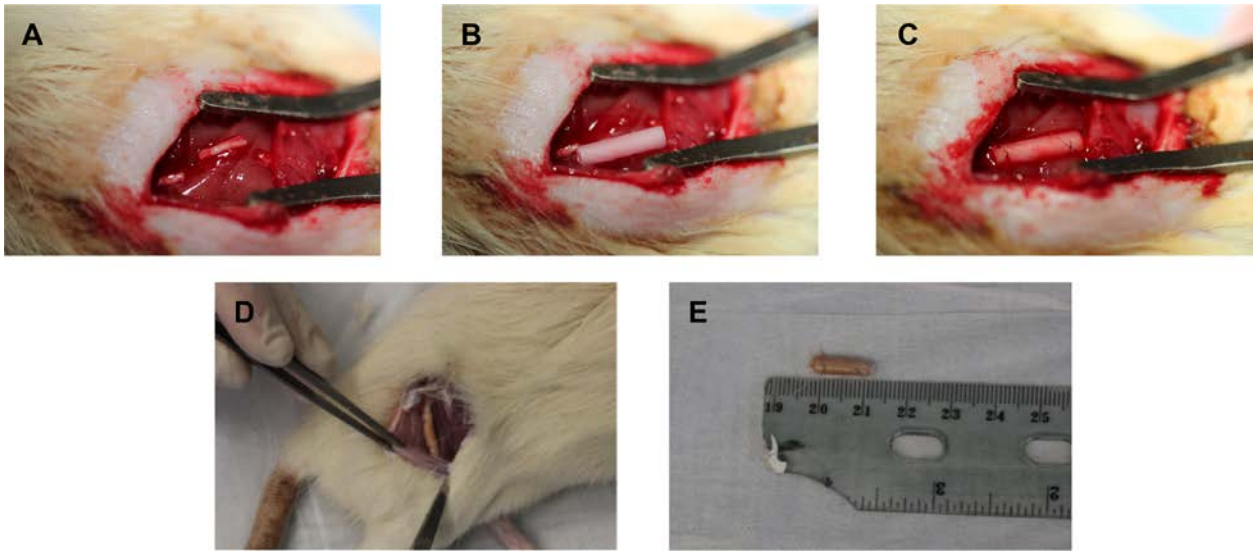

Figure 21. Implant and explant of nerve conduits. (A) 1 cm of sciatic nerve was removed and **(B)** a 1.2 cm long nerve conduit was placed in the gap. **(C)** Proximal and distal ends of the nerve were sutured 1 mm into each end of the tube. **(D)** Gross morphology of conduit attached to nerve at 6 weeks. **(E)** Gross morphology of nerve conduit explant at 6 weeks.

Over the course of 6 weeks, MSC retention was found to be remarkably different (Figure 22). Figure 22A shows representative longitudinal sections of resulting conduits at 1, 2, 4, and 6 weeks. Quantitation of the DiI signal from these sections showed that in the case of wall-

encapsulation, ASCs were retained for up to 4 weeks, while with injection the ASCs, cell abundance started to decline after just 1 week (Figure 22B). Direct comparison for a period of 6 weeks revealed significantly higher intensities at 2 and 4 weeks for wall-encapsulation *versus* injection, with $p<0.05$ and $p<0.005$, respectively (Figure 22C). These findings strongly suggest that cells persisted in wall-encapsulated conduits longer than those introduced via the conventional cell injection method.

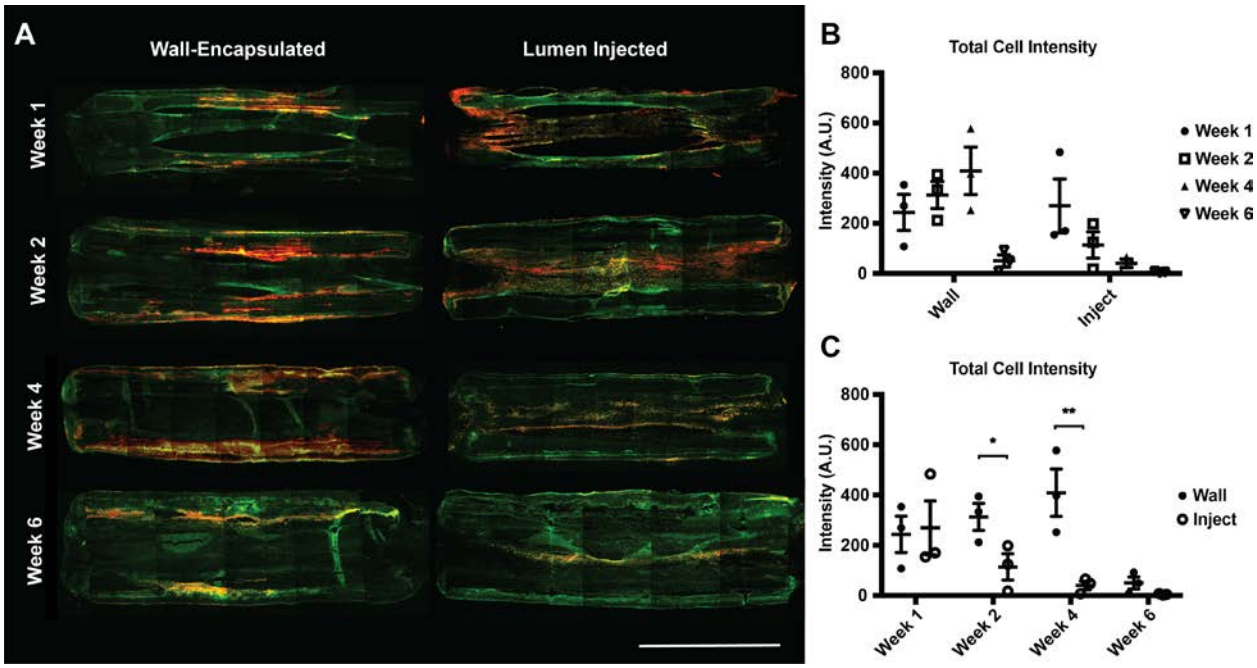

Figure 22. Cells are retained longer *in vivo* with wall-encapsulation compared to lumen injection. (A) Representative images of DiI labeled cells in conduits at 6 weeks. Red channel is DiI label while green is scaffold autofluorescence. **(B)** Total DiI-labeled cell intensity (A.U., arbitrary units) at 6 weeks for wall-encapsulated *versus* lumen injected cell groups, showing trends within groups. **(C)** Total DiI-labeled cell intensity across 6 weeks comparing between groups at each week. *, $p<0.05$; **, $p<0.005$. Scale bar: 5 mm.

Since there were significant differences seen at weeks 2 and 4, these time points were assessed in terms of both DiI labeled ASC cell intensity and Schwann cell intensity along the length of the conduit (Figure 23). Of note, implanted conduits did not elicit a foreign body reaction and they limited fibrous infiltration through the walls of the conduit (Figure 24). Conduits were serially sectioned transversely 4 mm proximally and distally from their center, stained, and analyzed for Schwann cells and ASCs (Figure 23A). Figure 23B demonstrates localization of seeded ASCs relative to migrating Schwann cells in wall-encapsulated conduits, while Figure 23C portrays those in lumen injected conduits – note the localization of ASCs to walls vs. lumen. Upon examination of ASC intensity along the length of the conduits at Week 4, Figure 23D,E clearly showed differing distributions. These are significantly different by Mann-Whitney testing ($p=0.0039$). Upon fitting to either quadratic or Gaussian distributions, wall-encapsulated conduits preferentially fit Gaussian with 84.74% probability and $r^2 = 0.4463$ while injected conduits preferentially fit quadratic with 91.17% probability and $r^2 = 0.3280$ (Figure 23D,E). These profiles described a migration outward from the center of the conduit and migration inward from ends of the conduit, respectively. Correlating these distributions with Schwann cell intensity at 2 weeks, there was a significant trend towards earlier Schwann cell migration into the center of the conduit in the wall-encapsulation group in comparison to the injection group, which showed very limited Schwann migration inwards ($p=0.0457$, Mann-Whitney)(Figure 23F). By 4 weeks, Schwann cells appeared to take on a unimodal distribution located near the center of the conduit in wall-encapsulated groups while they were more random in nature in the injection groups (Figure 23G).

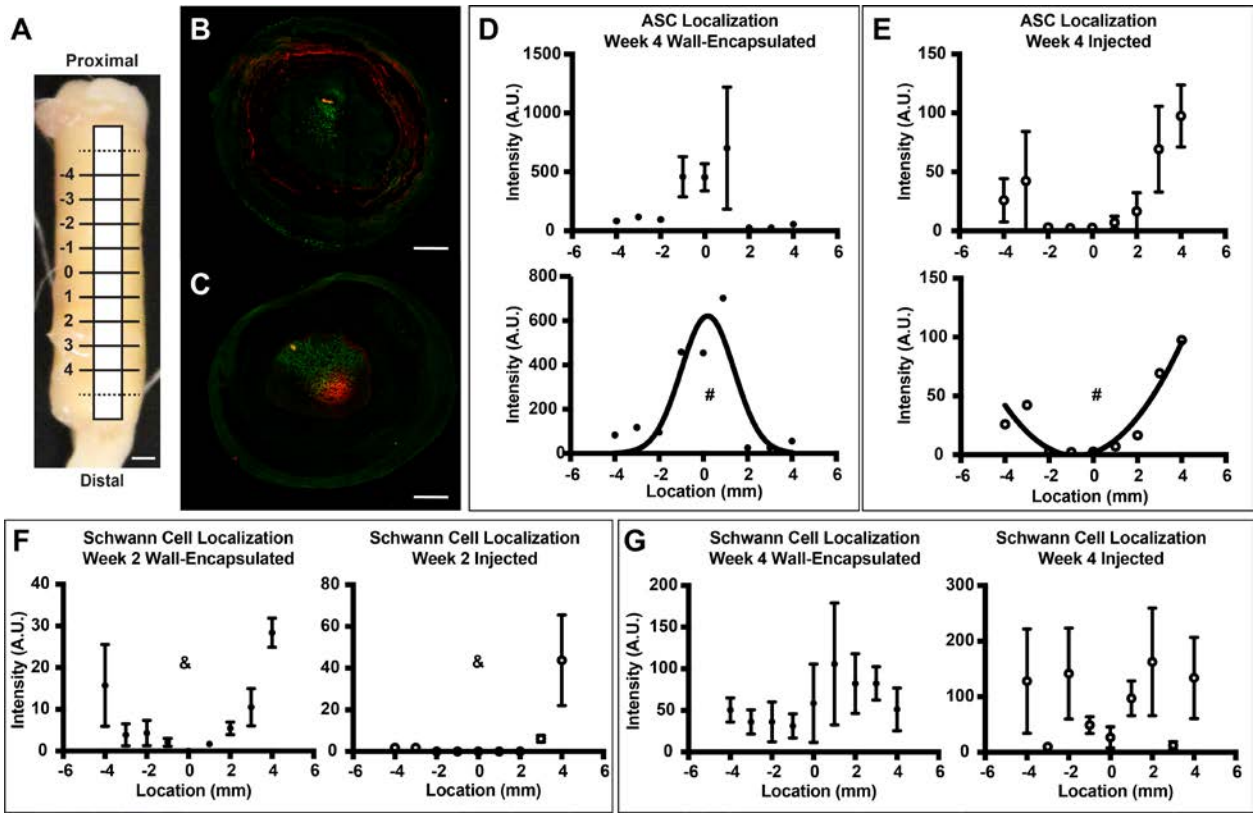

Figure 23. Conduits with centrally located wall-encapsulated ASCs drive directional Schwann cell migration. **(A)** Schematic of locations sectioned along explanted nerve conduits (4 mm out from the center proximally and distally) from 1 cm rat sciatic nerve transection model. Scale bar: 1 mm. **(B,C)** Representative micrographs depicting localization of Schwann cells (green) and DiI-labeled (red) wall-encapsulated or lumen-injected ASCs, respectively. Scale bar: 500 μm. **(D,E)** ASC spatial distribution along the length of explanted conduits in wall-encapsulation *versus* lumen injection at 4 weeks. Wall-encapsulated ASCs fit a Gaussian distribution while lumen-injected ASCs fit a quadratic distribution. **(F,G)** Schwann cell localization and distribution along the length of the explanted conduit at two weeks and four weeks, respectively. Schwann cells possess a stronger inward migration at two weeks in wall-encapsulation group, and by four weeks resemble a single peaked distribution near the center of the conduit, as opposed to those in the lumen injection group, which possesses no clear distribution pattern. #, $p<0.005$ between distributions (Gaussian, fit probability = 84.74% and $r^2 = 0.4463$; Quadratic, fit probability = 91.17% and $r^2 = 0.3280$). &, $p<0.05$ between distributions.

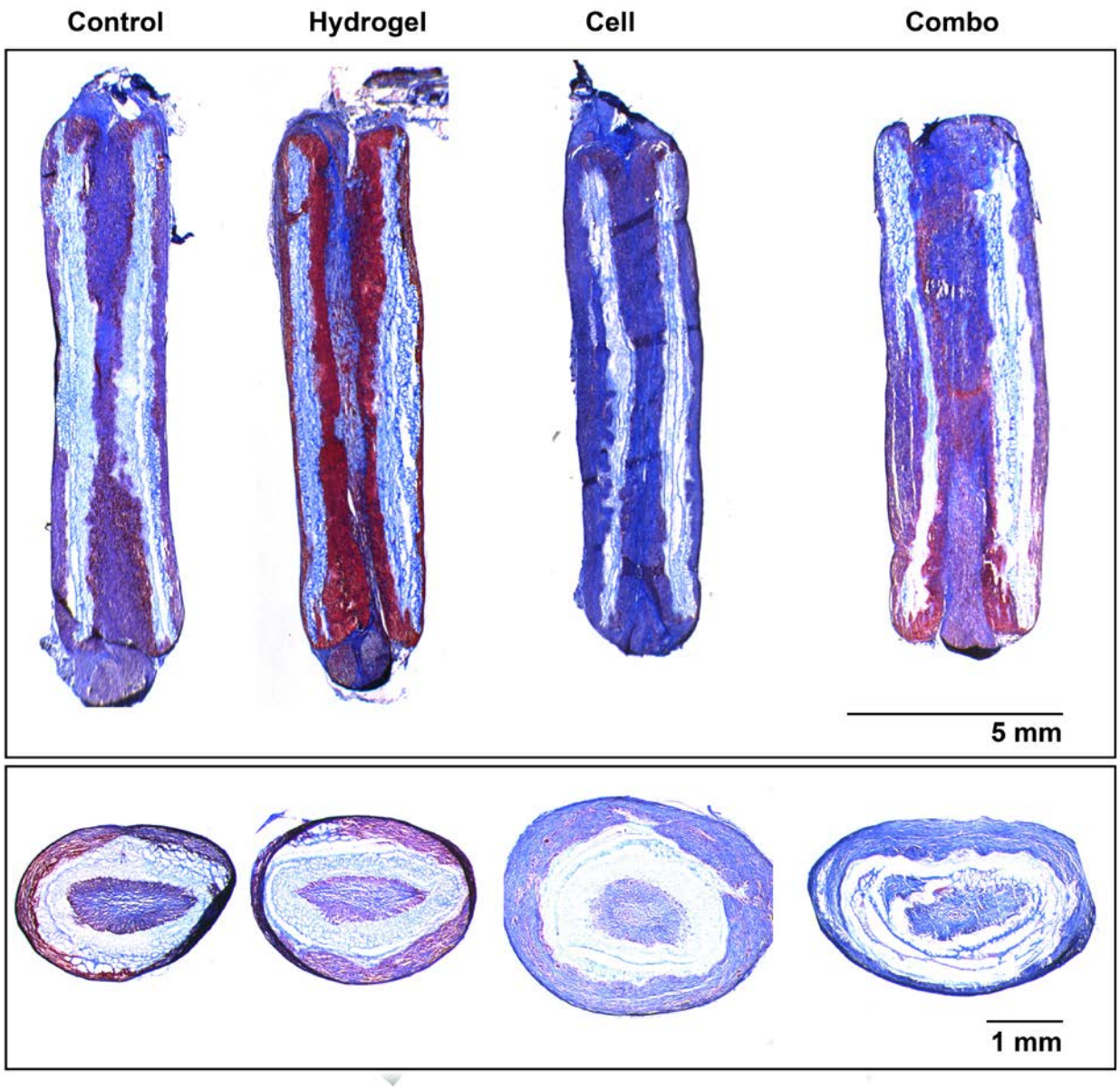

Figure 24. Masson Trichrome staining of 6 week nerve conduit explants. (Top, Bottom) Longtiduinal and transverse sections of conduits at the center, respectively. Blue stains for collagen while red stains nuclei. Note: the conduit itself also stains lightly blue. Control groups display a thin regenerating bridge through the conduit while cell and hydrogel + cell (combo) groups demonstrate much thicker regenerating bridges. Control and hydrogel conduits possess much less collagen production in their walls when compared to cell-containing groups, and it can be seen that cells do not infiltrate into the inner aligned layers of the conduit (evidenced by red staining only in the outer portion of the conduit walls).

Finally, at 6 weeks, complete bridging of the nerve conduit with Schwann cells was observed in the wall-encapsulation group (Figure 25A), and the Schwann cell area in the center of the nerve conduit was significantly higher in the wall-encapsulated group compared to both no-cell control and cell injection (Figure 25B), suggesting that Schwann cell migration was enhanced in wall-encapsulated groups.

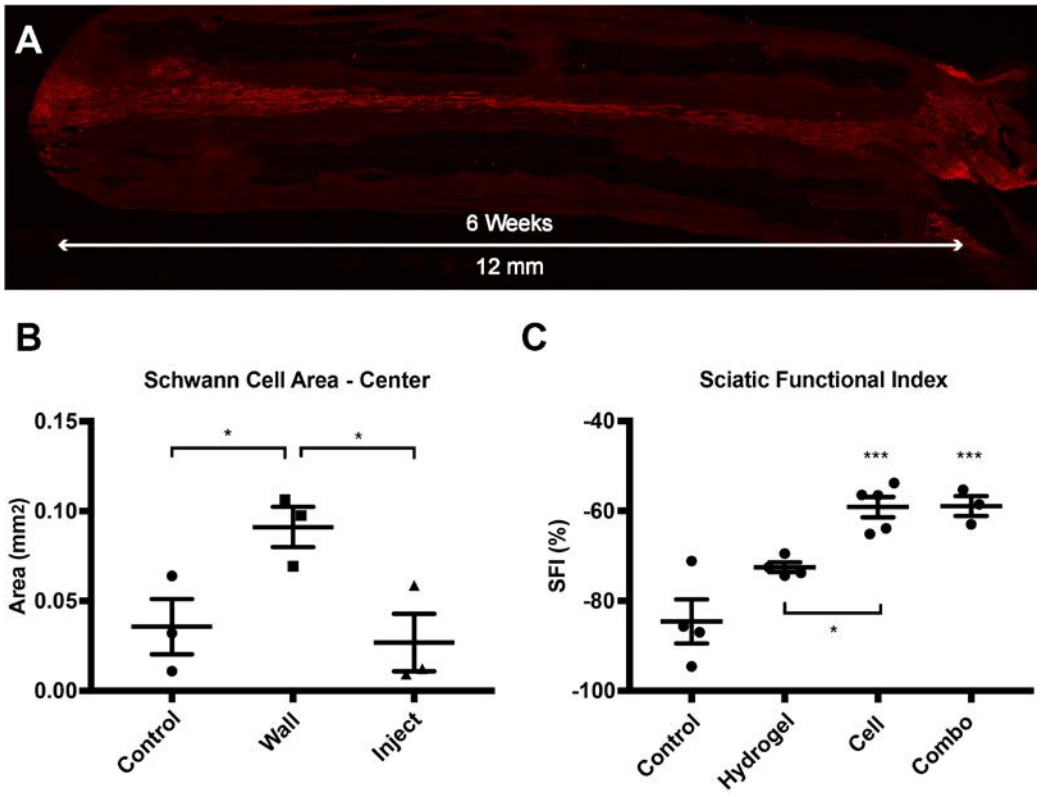

Figure 25. Conduits with centrally located wall-encapsulated ASCs improve functional return. (A) Image of Schwann cells bridging the nerve conduit with wall-encapsulated ASCs at 6 weeks in a rat 1 cm sciatic nerve transection model. Bar: 1 mm. **(B)** Schwann cell-positive area in cross-section of center of conduits in cell-free control, and wall-encapsulated and lumen injected cell groups. **(C)** Sciatic functional index at 16 weeks for cell-free control (control), nerve conduits with ECM hydrogel lumen filler (hydrogel), nerve conduit with wall-encapsulated cells (cell), or nerve conduit with wall-encapsulated cells plus ECM hydrogel lumen filler groups (combo). *, $p<0.05$, and ***, $p<0.001$, compared to Control.

2.3.4 Conduits with Wall-Encapsulated Cells Improve Peripheral Nerve Regeneration

To evaluate the significance of the ASC seeding dependent change in Schwann cell distribution, the ability of the different nerve conduits to effect functional recovery in a 1 cm rat sciatic nerve transection model was analyzed. Four groups were tested: conduits with or without wall-encapsulated cells in the central third of the conduit and with or without hydrogel filler. We chose to use a hydrogel filler derived from decellularized peripheral nerve to enhance the neurotrophic factor milieu within the nerve conduit [161]. At 16 weeks post-surgery, the wall-encapsulated cell group (cell) and combination of wall-encapsulated cells with hydrogel (combo) both presented with significantly higher sciatic functional index (SFI) when compared to control ($p<0.001$) (Figure 25C). In addition, the cell group also significantly increased SFI compared to the no-cell with hydrogel filler group (hydrogel) ($p<0.05$). The hydrogel *versus* control and combo *versus* hydrogel comparisons were both at the border of significance ($p=0.0627$ and $p=0.0505$, respectively). These results demonstrate that the presence of wall-encapsulated cells greatly enhanced functional outcomes.

Lastly, axon myelination at 16 weeks was also assessed to correlate with functional outcomes (Figure 26). MSCs have previously been shown to increase myelination when applied in nerve conduits [52]. Figure 26A depicts representative images of neurofilament, myelin, and DAPI staining while Figure 26B displays the same images with only the myelin channel for better visualization. The conduit was examined both at the center of the conduit, as well as at approximately 2 mm from the distal end of the transected nerve, given the known distal end of the nerve location of Wallerian degeneration. The cell group was seen to possess thicker axon myelination compared to control ($p<0.05$)(Figure 26C,D). The hydrogel group also exhibited increased myelination compared to control ($p<0.05$)(Figure 26C,D). The hydrogel group

displayed a significantly higher percentage of myelinated axons compared to control ($p<0.05$)(Figure 26E). The cell and combo group both had higher average myelination than control, but failed to reach statistical significance, likely due to lack of power ($p=.1361$ and $p=0.0896$, respectively)(Figure 26E). Overall, nerve conduits with wall-encapsulated cells were observed to significantly enhance functional return and axon myelination in rats 16 weeks post-repair.

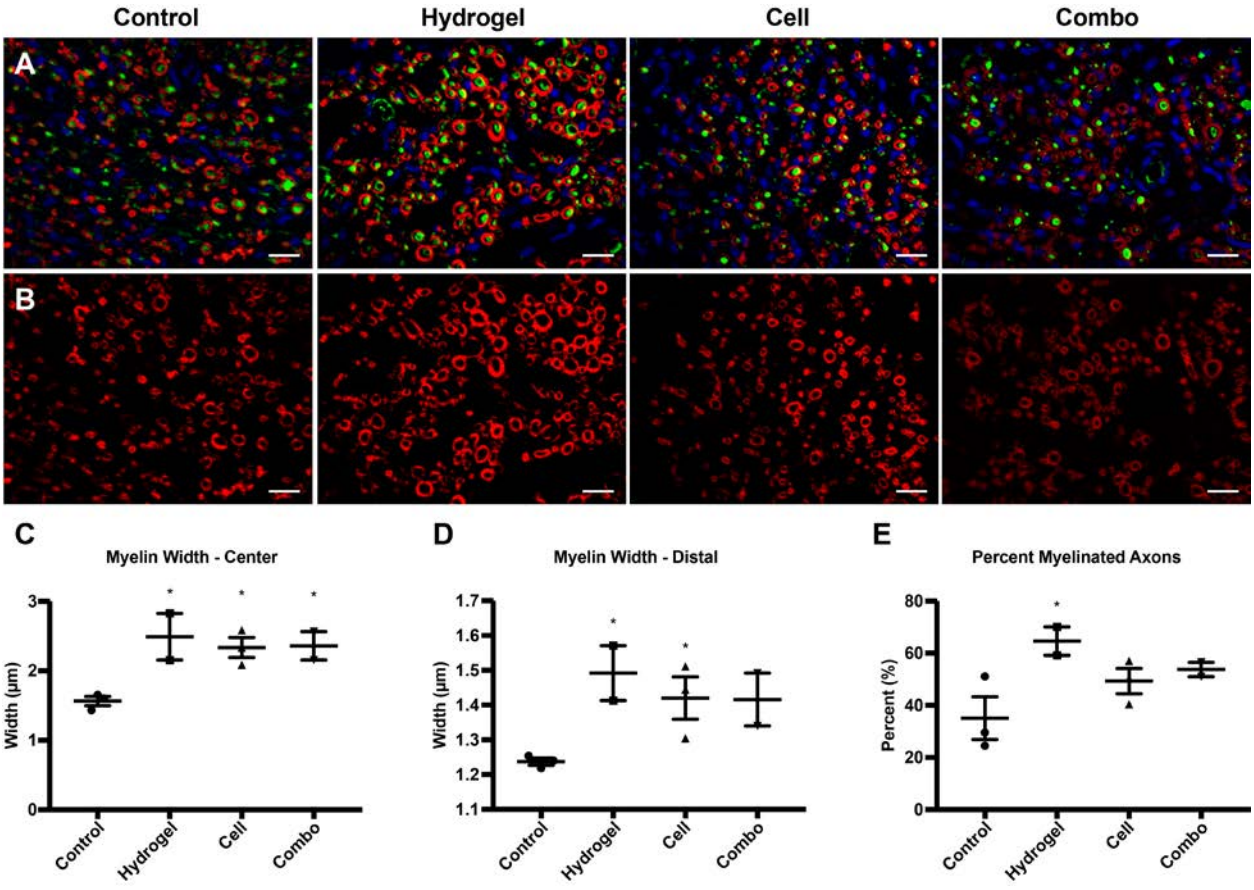

Figure 26. Conduits with centrally located wall-encapsulated ASCs improve axon myelination. (A) Representative images of nuclear, axon, and myelin staining at distal end of conduit for cell-free control (control), nerve conduit with ECM hydrogel lumen filler (hydrogel), nerve conduit with wall-encapsulated cells (cell), or nerve conduit with wall-encapsulated cells plus ECM hydrogel lumen filler groups (combo). Green, NF-160; red, Fluoromyelin; and blue, DAPI. **(B)** Myelin staining isolated from images in A for better visualization. **(C)** Myelin width at center of conduit. **(D)** Myelin width at distal end of conduit. (E) Percent myelinated axons in distal end of conduit. *, $p<0.05$, compared to Control. Scale bar: 15 µm.

2.4 DISCUSSION

In this study, we have examined the effect of nerve conduits harnessing cell-secreted neurotrophic gradients on the regenerative response of peripheral nerves. To achieve this, a versatile conduit fabrication method capable of incorporating cells in a spatially controlled manner was designed and its biological and physical characteristics were assessed *in vitro* for potential application *in vivo*. Using a 1 cm sciatic nerve transection model in rats, implants with cells wall-encapsulated along the central third of the conduit length were seen to direct a stronger migration of Schwann cells into the center of the conduit compared to their counterparts consisting of lumen-injected cells. This effect resulted in complete bridging of the conduit at 6 weeks by Schwann cells, and a significantly higher area of Schwann cell localization in the center of the conduit compared to both cell-free conduits and conduits with lumen-injected cells. At 16 weeks, rats with these wall-encapsulated cellular conduits presented with significantly increased sciatic functional index and axon myelination over controls. Taken together, these results strongly suggest that the use of spatially controlled cell seeding to produce neurotrophic gradients presents a potentially powerful strategy for cell application in improving peripheral nerve regeneration.

Cell incorporation within conduits has been accomplished through a variety of methods [52], but none thus far have allowed for the immediate and controlled incorporation described here (Figure 9). While electrospun nanofibers have been utilized as conduits with beneficial outcomes, techniques to incorporate cells within these fibers during fabrication are lacking. This is likely due to the fact that nanofibers do not accommodate compressive stress, which makes a

cell-friendly fabrication more difficult as thicker conduit walls must be obtained through longer spinning times to avoid conduit collapse *in vivo*. One way around the poor compressive properties is the use of multiple layers of nanofibers to improve conduit stability, as has been described in various studies [46,50,171–173]. However, simply increasing the number of layers and "sandwiching" cells between them is still not suitable for cell seeding because delamination of the layers occurs [159]. The key to the technique described here is in the use of the sacrificial GelMA fiber, which dissolves upon addition of an aqueous solution and allows the solution to permeate between remaining fibers. In this way, after solidifying the aqueous gel component by photocrosslinking, all layers are tightly bonded together and resist delamination. This leads to the cell morphologies and the concentric arrangement of cells observed in the final conduit (Figure 14). In addition, the gel component grants elasticity to the overall structure, which is lacking in a purely nanofibrous construct (Figure 9E).

This fabrication strategy was shown to significantly increase DRG neurite extension *in vitro* (Figure 18). We hypothesize that the increase in length is attributable to paracrine neurotrophic factor secretion as physical contact between the seeded cells and the DRG is lacking. Our results correlate well with reported observations of increased growth using conditioned medium derived from similar cells [143]. Further support is that VEGF and BDNF, two growth factors produced at high levels by these cell types, have been shown to significantly aid axonal extension [22,140–143]. In addition, there have been many descriptions of neurotrophic factors in the MSC secretome that enhance nerve growth [52,174]. Thus, our observations are in accordance with previous findings, and strongly suggest that wall-encapsulated cells exert their effects through neurotrophic factor secretion rather than other processes such as transdifferentiation [175].

Testing this cell encapsulation system against the standard cell injection method, we found that cells were retained effectively with encapsulation for up to 4 weeks (Figure 22). We hypothesize that the sudden drop from 4 to 6 weeks is due to loss of the bulk of the GelMA component (Figure 13), allowing cells to migrate out of the walls of the conduit. On the other hand, the number of cells introduced by injection decreased steadily over the course of 6 weeks, which agrees with previous observations that live injected cells are largely absent in the conduit site [99]. Utilizing cells located in the walls along only the central third of the conduit, we sought to create a biomolecular gradient [153] of cell-secreted NTFs with the highest concentration in the center that decreased towards the ends of the conduit due to diffusion of NTFs (Figure 23). This method of cell seeding led to a Gaussian distribution pattern instead of the quadratic distribution pattern observed with cell injection (Figure 23D,E). Interestingly, we found that this localization of cells and the associated, theoretical biomolecular gradient was sufficient to drive Schwann cells into the center of the regenerating nerve bridge as early as 2 weeks (Figure 23F). Studies utilizing carefully constructed growth factor gradients have also reported either increased axonal extension or increased Schwann cell migration, supporting our hypothesis that cell localization is capable of creating a cell-secreted neurotrophic factor gradient [145–149,152]. By 6 weeks, full bridging of the conduit with Schwann cells is observed (Figure 25A), with significantly higher Schwann cell-positive area in encapsulation *versus* injection and non-cell seeded controls (Figure 25B). Surprisingly, implanted ASCs were found to be negative for BDNF, and uninduced ASCs are not known to produce conventional Schwann chemotactic factors like GDNF in appreciable quantity [146,155]. Our observations, however, can be reconciled by the finding that TGF-β, which our implanted ASCs secrete (Figure 19B), drives Schwann cells into the regenerating nerve bridge during the nerve repair process [144].

At week 16, conduits with wall-encapsulated cells displayed enhanced functional return and axon myelination even in the absence of a lumen filler (Figure 25C, Figure 26). This increase in myelination is in accordance with observations that injected or seeded MSCs promote axon myelination [52]. It is noteworthy that the presence of a hydrogel lumen filler derived from decellularized peripheral nerve did not synergistically add to the capabilities of the cellular conduit. We hypothesize that this is because the hydrogel and cells both act through neurotrophic factor enhancement of nerve regeneration, such that the cell-secretome induced migration of Schwann cells is not further augmented by the NTFs found in the hydrogel (Note: The hydrogel was semi-solid in nature, and was thus unlikely acting as a ready medium for migrating cells).

Among the findings in this study, one aspect we find particularly interesting is the differing Schwann cell distributions at 2 and 4 weeks between wall-encapsulated and injected cells (Figure 23F,G). Despite the lack of a lumen filler, at both 2 and 4 weeks Schwann cells seem to be making their way to the center of the conduit in the wall-encapsulated groups. However, the distribution of Schwann cells in cell injection groups at 4 weeks shows no clear pattern and seems to be almost random in distribution, with the majority at least 2 mm away from the center. The sudden increase in Schwann density over the course of 2 weeks hints that although seeded-cells can provide directionality to migrating Schwann cells, the limiting factor in this lumen filler-free conduit may be the formation of the fibrin network for the Schwann cells to migrate through [18]. Future studies will assess the capabilities of the wall-encapsulated cellular scaffold with an aligned porous lumen filler to take advantage of the early Schwann cell migration towards the center of the conduit. Of note, regeneration of the nervous system can also be studied in non-mammalian species (85).

Lastly, we have shown here that a cell-seeded conduit using polycaprolactone and GelMA can be effective in enhancing the nerve regenerative response. However, this conduit fabrication method is not limited to these particular materials or cells. It is highly versatile, as different nanofibers can be incorporated and different photo-polymerizable aqueous gels can be applied during fabrication as long as a sacrificial nanofiber is present in the composite nanofiber scaffold. This method can be used to modulate various attributes, such as increased permissibility for Schwann cell attachment and migration (i.e. silk fibroin fibers [176]), inclusion of growth factors or microparticles within the gel component for controlled factor release (Figure 17B), or incorporation of slower degrading hydrogel component to enhance cell retention. Importantly, material properties can be modulated to affect cellular differentiation and function (141).

In designing this conduit fabrication strategy, we sought to harness the neurotrophic capabilities of MSCs by introducing increased control to the process of cell seeding with a versatile conduit fabrication method. Our results demonstrate the efficacy of this method, and support the hypothesis that MSCs enhance regeneration through paracrine factor secretion rather than transdifferentiation. Overall, this method presents a new approach for studying and maximizing the potential of cell application in peripheral nerve repair.

2.5 CONCLUSIONS

Cell incorporation in nerve conduits is a widely used strategy to enhance peripheral nerve regeneration. However, typical cell seeding procedures do not allow for the production of cell-secreted neurotrophic gradients. We have developed a versatile fabrication technique to seed cells with high spatial control within the walls of a conduit. We demonstrated that conduits utilizing cell-secreted gradients originating at the center of the conduit modulate and drive Schwann cell migration into the regenerative nerve bridge leading to improved regeneration and functional return. This method of utilizing a spatially restricted cell secretome is a departure from conventional homogeneous or uncontrolled cell distributions, and presents a new approach for studying and maximizing the potential of cell application in peripheral nerve repair.

3.0 SUMMARY AND FUTURE DIRECTIONS

Currently, peripheral nerve repair lacks adequate efficacy in the case of large segmental defects. These types of injuries, however, are becoming more prevalent especially in the battlefield. While welcome advances in protective armor and efficient air-evacuations have improved chances of survival when faced with heavy fire (gunshots, explosions, extremity trauma), they have not been able to protect against severe combat injuries. As such, these injuries are carried into civilian life and result in significant morbidity and functional disability. The need for effective strategies to restore function in cases of complete nerve transection are thus of critical importance.

The work presented in chapter 2 elaborates the development, construction, and *in vitro* and *in vivo* validation of a novel nerve conduit that addresses many of the limitations of previous techniques in terms of cellular augmentation. Conventional methods of cell seeding offer very little control over spatial location of seeded cells or injected cells, and along with this there is a lack of cellular retention as well due to cell migration out of the scaffold. The technique described here balances the need for structural stability, elasticity, and degradation with the constraints of a cell-friendly fabrication method while still allowing for spatial control. It is unique among current conduits due to this feature, and is versatile as the technique can be tailored with different materials and hydrogels to achieve a variety of degradation rates, mechanical strengths, and nerve permissive environments. In addition, this method can also

readily incorporate controlled release mechanisms such as microparticles or direct growth factor loading.

The *in vitro* and *in vivo* results point to the ability for cells encapsulated with this technique to exert pro-regenerative effects on damaged nerves, including significantly enhanced functional return and myelin width. While these findings are significant for the viability and efficacy of this method, the most important observation using this conduit is that Schwann cell migration into the bridge can be accelerated by a localized cell distribution at the center of the conduit. This implies that cellular application for peripheral nerve regeneration has not reached its full potential, and it opens up another avenue of study for nerve conduits – namely how and where to localize cells to maximize their benefit. Along this line, given the data that strongly suggests that neurotrophic factor secretion is the main mechanism of action of seeded cells in promoting nerve regeneration, optimizing cell type and secretion profile is another avenue to explore.

This new technology opens up many future directions for study. First, the ultimate goal of fabricating these conduits is to be clinically translated. As the conduit fabrication process currently stands, it can be used as a point-of-care treatment for peripheral nerve injuries given the immediacy of fabrication. However, to be clinically adopted the process must be simplified and the materials must be available off the shelf. This endeavor will require new device design and good manufacturing practice adoption and re-optimization of many manufacturing parameters.

More importantly, scientifically there are many questions to ask. Future studies should focus on how the use of aligned, porous, solid lumen fillers in conjunction with this technique to determine if these methods can act synergistically. One of the limiting steps in nerve regeneration is the formation of a solid substrate that can bridge the nerve gap, and thus

introduction of one from the earliest timepoint could greatly enhance the Schwann chemotactic effects seen. Additionally, larger animal models should be conducted to determine if the effect is more pronounced over a greater gap length – or if there is a limit to the effective range of the biomolecular gradient that is produced by the cells.

In conjunction with all of these explorations, vitally important is a look at the mechanism behind Schwann cell chemotactic migration into the center of the conduit. Mesenchymal stem cells are known to secrete hundreds of growth factors – and there are likely more that are still yet to be defined. This presents an opportunity to probe the secretome of various cell types and identify the Schwann chemotactic factors and neurotrophic factors that drive the regenerative augmentation seen with cell incorporation. The ability to separate these cells from the lumen and retain them within the walls allows us to parse out the paracrine effects vs contact-mediated effects and will greatly contribute to our understanding of cell behavior in this regenerative environment.

Overall, the work in this dissertation opens many potential avenues of study in peripheral nerve regeneration and has implications in other areas of tissue engineering where directionality and cell seeding localization can lead to differential effects. This is a step forward in maximizing the potential of cells in nerve tissue engineering, and in the coming decades this author is hopeful that we will see an emergence of stem cell-aided peripheral nerve regeneration therapies in the clinic.

APPENDIX A

MACHINE SOLIDWORKS DESIGN FILES

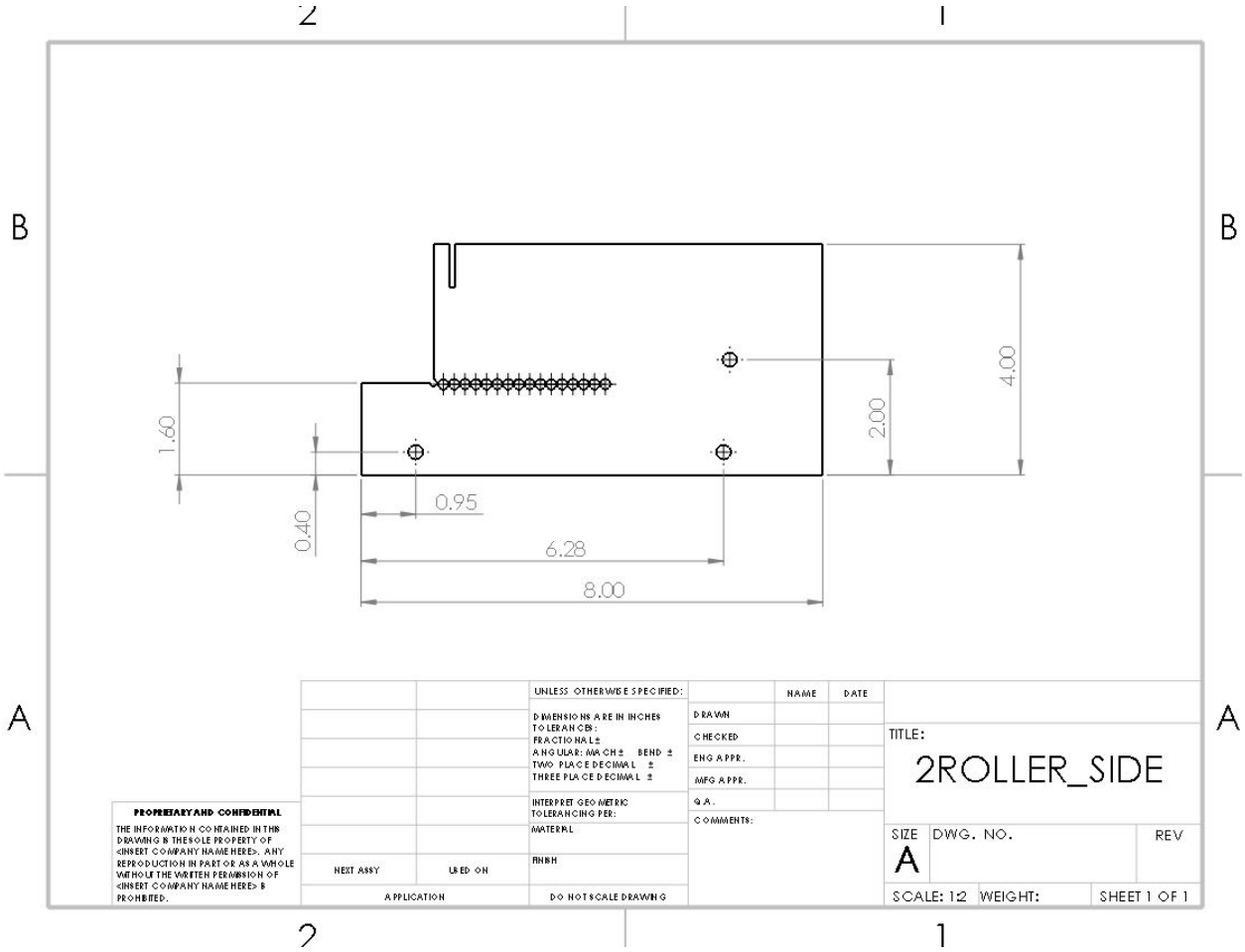

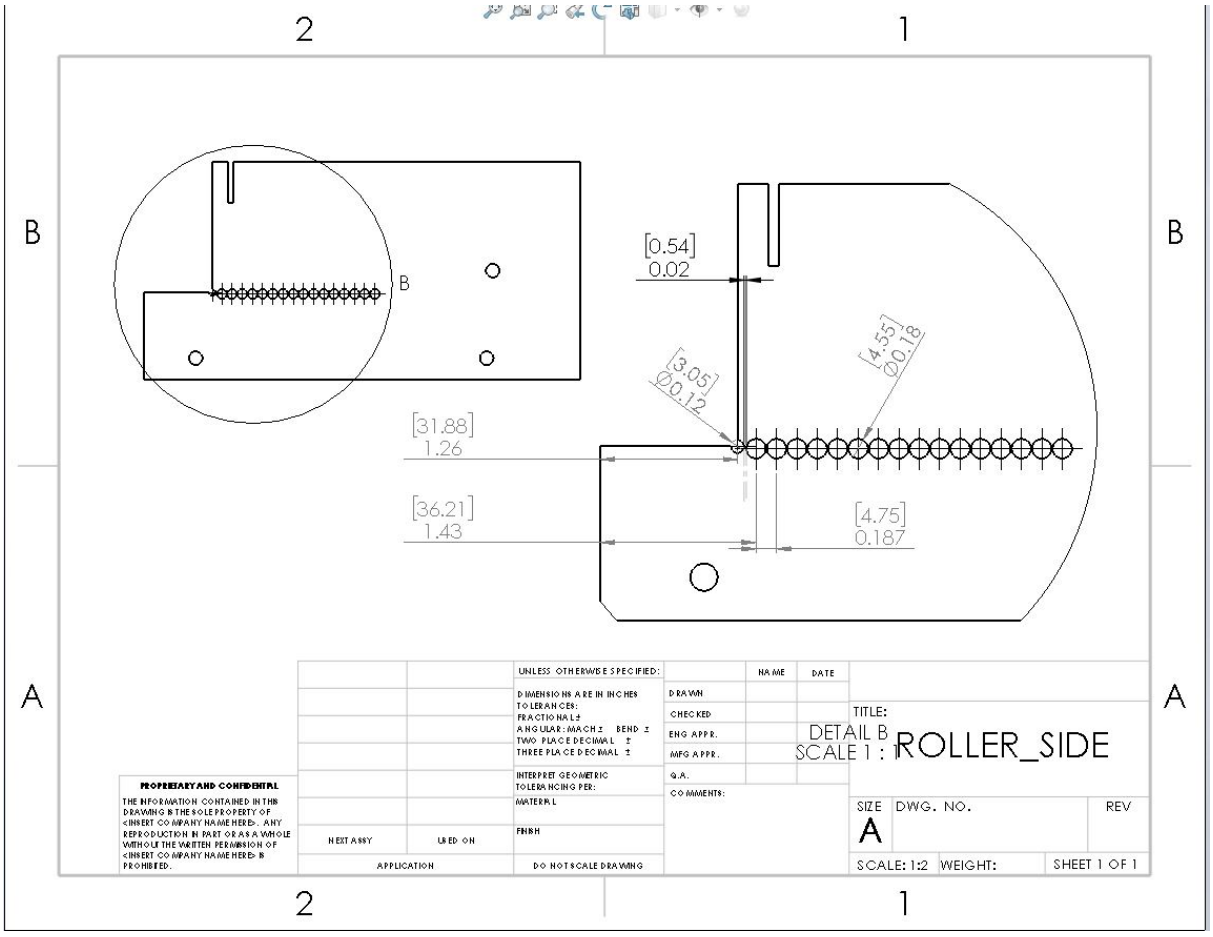
2
1
B
A
[0.54]
0.02
[3.05]
Ø0.12
[4.55]
Ø0.18
[31.88]
1.26
[36.21]
1.43
[4.75]
0.187
UNLESS OTHERWISE SPECIFIED:
DIMENSIONS ARE IN INCHES
TOLERANCES:
FRACTIONAL ±
ANGULAR: MACH ± BEND ±
TWO PLACE DECIMAL ±
THREE PLACE DECIMAL ±
INTERPRET GEOMETRIC TOLERANCING PER:
MATERIAL
FINISH
DO NOT SCALE DRAWING
NAME
DATE
DRAWN
CHECKED
ENG APPR.
MFG APPR.
Q.A.
COMMENTS:
TITLE:
DETAIL B
SCALE 1 : 1
ROLLER_SIDE
SIZE
A
DWG. NO.
REV
SCALE: 1:2
WEIGHT:
SHEET 1 OF 1
PROPRIETARY AND CONFIDENTIAL
THE INFORMATION CONTAINED IN THIS DRAWING IS THE SOLE PROPERTY OF <INSERT COMPANY NAME HERE>. ANY REPRODUCTION IN PART OR AS A WHOLE WITHOUT THE WRITTEN PERMISSION OF <INSERT COMPANY NAME HERE> IS PROHIBITED.
NEXT ASSY
USED ON
APPLICATION

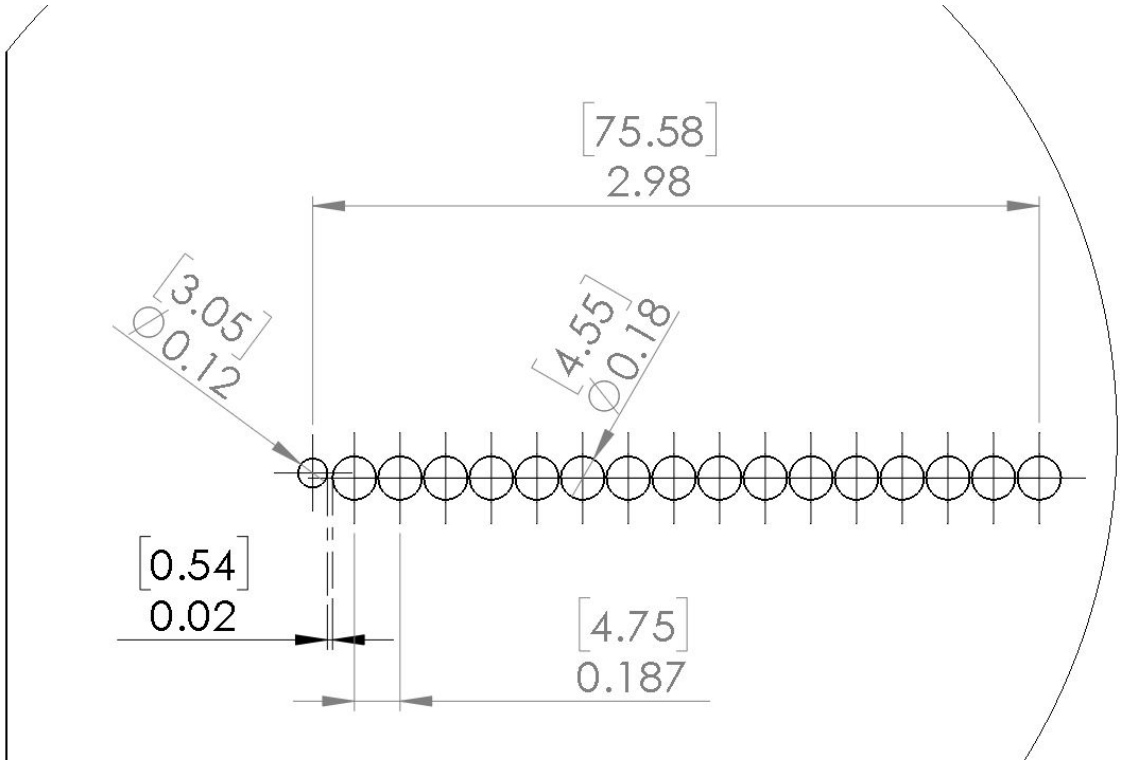
[75.58]
2.98
[3.05]
Ø0.12
[4.55]
Ø0.18
[0.54]
0.02
[4.75]
0.187

APPENDIX B

DIFFERENCES IN NEURAL STEM CELL IDENTITY AND DIFFERENTIATION CAPACITY DRIVE DIVERGENT REGENERATIVE OUTCOMES IN LIZARDS AND SALAMANDERS

Abstract

While lizards and salamanders both exhibit the ability to regenerate amputated tails, the outcomes achieved by each are markedly different. Salamanders such as *Ambystoma mexicanum* regenerate nearly identical copies of original tails. Regenerated lizard tails, on the other hand, exhibit important morphological differences compared to originals. Some of these differences concern dorsoventral patterning of regenerated skeletal and spinal cord tissues; regenerated salamander tail tissues exhibit dorsoventral patterning, while regrown lizard tissues do not. Additionally, regenerated lizard tails lack characteristically roof plate-associated structures such as dorsal root ganglia. We hypothesized that differences in neural stem cells (NSCs) found in the ependyma of regenerated spinal cords account for these divergent regenerative outcomes. Through a combination of immunofluorescent staining, RT-PCR, hedgehog regulation, and transcriptome analysis, we analyzed NSC-dependent tail regeneration. Both salamander and lizard Sox2-positive NSCs form neurospheres in culture. While salamander neurospheres exhibit

default roof plate identity, lizard neurospheres exhibit default floor plate. Hedgehog signaling regulates dorsalization/ventralization of salamander, but not lizard, NSCs. Examination of NSC differentiation potential *in vitro* showed that salamander NSCs are capable of neural differentiation into multiple lineages whereas lizard NSCs are not, which was confirmed by *in vivo* spinal cord transplantations. Finally, salamander NSCs xenogeneically transplanted into regenerating lizard tail spinal cords were influenced by native lizard NSC hedgehog signals, which favored salamander NSC floor plate differentiation. These findings suggest that NSCs in regenerated lizard and salamander spinal cords are distinct cell populations, and these differences contribute to the vastly different outcomes observed in tail regeneration.

Introduction

Along the evolutionary tree, regenerative capabilities are lost as evolutionary distance to mammals decreases [177,178]. From the ability to fully regrow limbs and organs observed in some species to the fibrotic scarring process observed in many mammalian responses, the healing response is vastly different in both mechanism and outcome [179]. In order to gain insight into these fascinating processes, the axolotl (*Ambystoma mexicanum*) has been extensively studied as a model organism in hopes of elucidating the mechanisms that allow for identical regeneration of many of its tissues [180–189]. Our understanding of factors that drive axolotl regenerative potential has grown considerably, but the leap towards effecting regeneration in evolutionarily distant mammals remains a challenge.

Between the axolotl and non-regenerating mammals, lizards sit as an intermediary species on the evolutionary tree and are thought to be the only amniotes capable of tail regeneration [190–192]. Lizards possess an "intermediary" ability to regenerate as well, with a peculiar set of morphological differences that distinguish lizard tail regenerates from the originals, unlike the faithfully regenerating salamander tails [190,193–195]. These differences include a striking lack of dorsoventral patterning in the lizard tail regenerate [196], and the key to understanding this unique arrangement of tissues lies in identifying the patterning signals involved.

Both lizards and salamanders follow similar mechanisms of tail development during embryonic development. The embryonic spinal cord and surrounding structures are formed and patterned by the neural tube [197,198]. The neural tube exhibits distinct domains: roof plate (characterized by expression of $Pax7^{+}$, BMP-2^{+}, $Sox10^{+}$, among others), lateral domain (Pax6+), and floor plate (Shh+, FoxA2+). The ventral floor plate expresses Shh that, along with the

notochord, induces differentiation of surrounding mesoderm into sclerotome, eventually forming the embryonic axial skeleton, while the dorsal roof plate expresses Wnt and BMP that antagonize Shh signaling and induce formation of the dermatome and myotome. These different domains lead to the formation of characteristic roof plate structures such as sensory dorsal root ganglia and floor plate structures such as motor neurons.

Lizards and salamanders also exhibit similar spinal cord and skeletal development during later stages of development. Dorsal roof plate cells of the neural tube give rise to the sensory interneurons with which neural crest-derived dorsal root ganglia (DRG) cells synapse, while ventral floor plate cells give rise to motor neurons. During skeletogenesis, sclerotome surrounding the notochord forms vertebrae centrums, neural arches form to enclose tail spinal cords, and hemal arches form around tail arteries. Thus, the general skeletal and central nervous architectures are similar between lizard and salamander tails, which makes the differences in regenerated tissues so surprising.

The regenerated salamander tail spinal cord – specifically the radial glia that line the central canal – has been shown to carry out many of the same roles during tail regeneration as the neural tube during embryonic tail development [183,199,200]. This ependymal cell population is enriched with neural stem cells (NSCs) and forms a tube that extends from the original tail stump and infiltrates the regenerating tail blastema. In many ways, this "ependymal tube" is the regenerative analog to the embryonic neural tube. Like the neural tube, the salamander ependymal tube exhibits distinct domains with defined signaling characteristics. In addition to Shh^+ floor plate, $Pax6^+$ and $Pax7^+$ regions demark the lateral plate and roof-plate, respectively, and DRGs are re-formed [185]. Shh produced by the floor plate induces surrounding tail blastema cells to differentiate into cartilage, thereby forming the regenerated salamander tail cartilage rod.

The regenerating salamander skeleton follows the same general developmental scheme as during embryonic development. The cartilage rod transitions into vertebrae centrums, and neural and hemal arches form to enclose regenerated tail spinal cords and arteries, respectively. The end result is a regenerated tail skeleton nearly identical to the original. In this way, dorsoventral patterning of the ependymal tube directly influences dorsoventral patterning of other regenerating tissues, including the skeleton.

While lizards also regenerate ependymal tubes and cartilaginous skeletons, they are morphologically simpler, and the end result is very different from the original tails. The regenerated lizard tail skeleton consists of a single, unsegmented cartilage tube that completely surrounds the ependymal tube [194]. Unlike the salamander cartilage rod, the lizard cartilage tube persists for the lifetime of the regenerate and never transitions into vertebral structures. We have previously shown that the lizard cartilage tube is induced by Shh produced by the ependymal tube, just like the salamander cartilage rod [196,201]. However, unlike the salamander ependymal tube, the lizard ependymal tube does not consist of distinct domains, and DRGs are not re-formed. Instead, the entire lizard ependymal tube expresses Shh, effectively designating the entire structure as floor plate. Thus, we hypothesize that the lack of dorsoventral patterning in the regenerated lizard tail is due to dominance of floor plate in the lizard vs salamander ependymal tube, and the goal of this study is to determine the reasons behind these differences. We report that cells participating in tail regeneration are not homogenous across species, specifically that differences in NSC populations found in the ependyma of spinal cords regenerated by lizards vs salamanders account, at least in part, for the divergent regenerative outcomes seen in these species with respect to skeletal and central nervous tissues.

Results

Lizards regenerate tails with skeletons and spinal cords that lack dorsoventral patterning and roof-associated structures. Both adult lizards and salamanders are able to regrow amputated tails and, upon gross observation, follow similar time courses in regeneration (Figure 37). Blastemas form by 14 days post amputation (DPA), and, by 28 DPA, regenerated tails are actively elongating. Maturity is reached past 56 DPA, at which point regenerated salamander tails appear similar to originals. Regenerated lizard tails, however, appear noticeably changed in appearance compared to originals, and further dissimilarities extend to regenerated tissues. Specifically, obvious differences in skeletal and central nervous tissues distinguish regenerated lizard tails from both original lizard and regenerated salamander tails (Figure 27). Original lizard and salamander tails contain similar vertebral and spinal cord structures as well as similar arrangements (vertebrae centrums ventral to spinal cords) (Figure 27A,B and Figure 38A). However, the regenerated lizard tail skeleton consists of an unsegmented cartilage tube that surrounds the regenerated spinal cord (RSC) (Figure 27A' and Figure 38B), while the regenerated salamander tail exhibits a segmented cartilage rod ventral to the RSC (Figure 27B'). This radial symmetry in regenerated lizard tails is the first indication that dorsoventral patterning is lost during the process of lizard tail regeneration. Similarly, while salamanders and lizards exhibit similar original tail spinal cord morphologies (Figure 27C,D and Figure 38A), another set of striking differences concerns the RSC: the total axonal area in lizard RSCs is greatly reduced (Table 2 and Figure 38D), and the characteristic butterfly shape is lost compared to the original (Figure 27C,E and Figure 38A,C). Salamanders, on the other hand, regenerate spinal cords that are similar to the originals in both axonal area (Table 2) and shape (Figure 27D,G). In addition, dorsal root ganglia are not regenerated in lizards (Figure 27E and Figure 38C). Instead,

regenerated tissues are innervated by extensions of peripheral nerves from DRGs within original tail regions proximal to tail amputation sites (Figure 27F). Unlike lizards, salamanders are able to regenerate DRGs (Figure 27G) [183]. Overall, there is a striking lack of roof plate and roof plate-associated structures (i.e. DRGs) within lizard regenerates, which we hypothesize is responsible for many of the differences exhibited by regenerated lizard tails.

Salamanders regenerate ependyma with roof plate, floor plate, and lateral domains, while lizards regenerate ependyma with floor plate only. Based on observations of the lack of roof-plate associated structures in regenerated lizard tails, we next probed the identity of the lizard ependymal tube. Previous studies have shown that spinal cords and ependymal tubes of original and regenerated salamander tails, respectively, expresses roof plate, floor plate, and lateral domains [185]. As a corollary to this, we investigated the expression patterns of Pax7, Pax6, BMPs, FoxA2, and Shh in original and regenerated lizard tails (Figure 28). Both original and regenerated salamander spinal cords contained ependyma with distinct $Pax7^+$ $BMP\text{-}2^+$ roof plate, Shh^+ $FoxA2^+$ floor plate, and $Pax6^+$ lateral domains (Figure 28A-D, E-H), while original and regenerated lizard ependyma only expressed floor plate markers Shh and FoxA2 (Figure 28I-L, M-P and Figure 39A-H). Note: analysis of lizard embryonic neural tubes was included as both validation of lizard antibodies and to emphasize resemblances in marker distributions between the embryonic neural tube and the salamander, but not lizard, ependymal tube (Figure 28Q-T and Figure 39I-L). Immunofluorescence results were verified by Western blots, which indicated that Pax7 was found to be missing in regenerated lizard but not salamander spinal cords (Figure 40). Taken together, these results strongly suggest that salamanders, but not lizards, regenerate roof plate ependymal tube domains and more closely recreate the morphology and signaling environment patterned by the neural tube during embryonic development.

Salamander spinal cord NSCs exhibit roof plate identity while lizard NSCs exhibit floor plate identity. Seeking to analyze the sources of patterning molecules within regenerated tails, we turned our attention to the cells within lizard and salamander ependymal tubes. The ependymal tube of the regenerated salamander tail is derived from populations of $Sox2^+$ NSCs found within original tail spinal cord ependyma, and these NSCs form neurospheres in response to FGF stimulation in culture [183]. We have identified similar $Sox2^+$ NSCs within the original lizard spinal cord ependyma that also formed neurospheres in culture (Figure 29A-D and Figure 41A,B). We also analyzed Pax7, Pax6, and Shh expression to determine the positional identity of salamander versus lizard NSCs *in situ* and after neurosphere formation *in vitro* (Figure 29E-P and Figure 41C-H). Both salamander and lizard spinal cords contained $Sox2^+$ NSCs. Salamander NSCs were detected in $Pax7^+$ roof plate, $Pax6^+$ lateral domain, and Shh^+ floor plate, (Figure 29E-G) while lizard NSCs were detected among floor plate only (Figure 29H-J and Figure 41C-E). In vitro, both salamander and lizard neurospheres were predominantly $Sox2^+$, indicating high NSC content. Salamander neurospheres were $Pax7^+$ $Pax6^-$ Shh^-, (Figure 29K-M) while lizard neurospheres were $Pax7^-$ $Pax6^-$ Shh^+ (Figure 29N-P and Figure 41F-H). Western blot analysis verified observed staining patterns (Figure 40).

Next we compared lizard and salamander tail spinal cord NSC proliferation both *in vivo* and *in vitro* (Figure 42 and Figure 43). 5-ethynyl-2'-deoxyuridine (EdU) incorporation/staining assays were used to visualize proliferating $Sox2^+$ NSC populations in original and regenerating (14, 28, and 56 DPA) tails along their lengths (proximal, middle, and distal). Salamander $Sox2^+$ NSC populations included more proliferative cells than lizards for all time points and positions, including original tails. 14 DPA samples, which correspond to the blastema stage of regeneration, exhibited the most numbers of proliferative NSCs for both lizards and salamanders.

Similarly, 28 DPA samples, which correspond to lengthening tails, exhibited higher numbers of proliferative NSCs than distal regions. In original, proximal 28 DPA, 56 DPA salamander samples, dorsal roof plate-localized $Sox2^+$ cells are more proliferative than ventral floor-plate cells, while no such dorsal/ventral bias was observed in lizards. These *in vivo* results were mirrored *in vitro* (Figure 42). In culture, salamander NSCs, which exhibit roof plate phenotypes, exhibited higher levels of EdU incorporation than lizard NSCs, which exhibit floor plate phenotypes (42.8% for salamanders versus only 7.9% for lizards). These results suggest a possible roof vs floor plate dependency on NSC proliferation.

Hedgehog signaling regulates dorsoventral patterning of salamander, but not lizard, ependymal tubes during tail regeneration. We next sought to test whether the ependymal tube was responsive to modulation of hedgehog signaling. Previous studies in salamanders found that hedgehog signaling controls both cartilage rod induction and ependymal tube dorsoventral patterning during tail regeneration [185]. The lizard cartilage tube is under similar regulation by hedgehog [196], and here we tested whether these similarities extend to the lizard ependymal tube. The hedgehog inhibitor cyclopamine was administered systemically to both lizards and salamanders (n=6) for 3 weeks following tail amputations, and the resulting regenerated tails were analyzed for Pax7 and Shh expression as indicators of ependymal tube dorsoventral patterning and for collagen type II (Col2) expression as a marker for cartilage formation (Figure 30). As expected, tails regenerated by salamanders treated with vehicle control developed ependymal tubes that expressed $Pax7^+$ roof plate and Shh^+ floor plate as well as $Col2^+$ cartilage rods in the ventrum (Figure 30A,B). Lizards treated with vehicle control developed ependymal tubes exhibiting circumferential Shh^+ expression and characteristic $Col2^+$ cartilage tubes (Figure 30G,H). Cyclopamine treatment inhibited cartilage formation in both lizards and salamanders, as

indicated by the loss of Col2 expression in the regenerated tails of both species (Figure 30C,I). In salamanders, cyclopamine also dorsalized ependymal tubes, with marked enhancement of Pax7 expression and reduction of Shh expression (Figure 30D). Like salamanders, cyclopamine treatment inhibited cartilage formation in lizards with complete disappearance of cartilage tubes (Figure 30I). However, unlike salamanders, lizard ependymal tubes did not respond to cyclopamine treatment. The entire ependymal tube remained positive for Shh expression, and Pax7 levels remained undetectable (Figure 30J). These results suggest that hedgehog signaling in regenerating lizards is not opposed by a dorsalizing signal, which is contrary to salamanders where a balance between roof and floor plate signaling exists.

We also tested the effects of the hedgehog agonist SAG on regenerated lizard tail ependyma and cartilage patterning. SAG treatment induced sparse ectopic cartilage formation in 1 out of 3 regenerated salamanders, whereas the response of lizard ectopic cartilage formation to SAG treatment was particularly strong, with extensive cartilage infiltration into various tail regions (3/3 samples). (Figure 30E,K). Interestingly, muscle regeneration was also substantially impaired in the SAG-treated animals (Figure 44). In salamanders, SAG treatment consistently resulted in ventralization of the ependymal tube (Figure 30F). Pax7 expression in dorsal regions was abolished and replaced by Shh, effectively converting the entire ependymal tube into floor plate - similar to the native lizard situation. Again, unlike salamanders, lizard ependymal tubes did not respond to SAG treatment (Figure 30L). Shh expression was maintained by the entire tube and Pax7 expression remained undetectable. Taken together, these results suggest that hedgehog signaling regulates dorsoventral patterning in the salamander, but not lizard, ependymal tube. The striking differences in responsiveness between lizard cartilage and ependymal cells to exogenous hedgehog inhibition and stimulation are particularly interesting.

The strong responsiveness of lizard cartilage to both SAG and cyclopamine treatments indicated effective treatment methods on lizard regenerated tails, and yet no changes in ependymal tube dorsoventral patterning were observed compared to vehicle controls. This is in direct contrast to dorsoventral patterning of the salamander ependymal tube, which was strongly influenced by hedgehog signaling. These results offer the first evidence of the pervasive and persistent properties of lizard NSC floor plate identity.

We next investigated the same signaling pathways *in vitro*, asking how these populations responded to hedgehog signaling when removed from the regenerating tail environment (Figure 31 and Figure 45). Default roof plate salamander neurospheres were unaffected by cyclopamine treatment and maintained high levels of Pax7 and undetectable Shh expression levels (Figure 31B). In contrast, administration of SAG resulted in the replacement of Pax7 with Shh expression (Figure 31C). These results correlate well with the *in vivo* findings where a fine balance exists between salamander ependymal tube roof and floor plate signaling, and stimulation of hedgehog signaling expands floor plate at the expense of roof plate. However, lizard neurospheres seemed to follow a different model. Cyclopamine administration did not abolish Shh, nor did SAG signaling cause an appreciable difference by immunostaining (Figure 31D-F and Figure 45). Immunostaining results were verified by Western blots (Figure 31G,H) and corroborated by real time RT-PCR gene expression analysis, in which a significant decrease in Shh expression was observed with SAG administration along with a small increase in Shh upon cyclopamine treatment (Figure 46). These results point to a model where Shh is constitutively expressed by lizard NSCs, and a negative feedback mechanism exists to control Shh gene levels. Notably, Pax7 levels were at the limit of detection or undetectable in all cohorts of lizard NSCs. Taken together, the *in vivo* and *in vitro* results from our experiments in Figure

30, Figure 31, Figure 45 and Figure 46 suggest that lizard NSCs are distinctly different compared to salamander NSCs in the way they work to pattern the regenerating tail.

Figure 32 summarizes our hypothesis on the differences between salamander and lizard NSC populations. Salamander NSCs are found in all domains (roof, lateral, and floor) within the original tail spinal cord. In the absence of hedgehog signaling, salamander NSCs exhibit roof plate markers, and are subsequently ventralized by Shh signaling in order to create the roof, lateral, and floor plate domains observed in the regenerated ependymal tube. NSCs isolated from the original adult lizard spinal cord ependyma (expressing only floor plate) maintain their default floor plate signaling even in the absence of hedgehog signaling. Lizard NSCs are unable to dorsalize, and their inherent floor plate identity is propagated into the regenerated tail.

Unlike salamanders, lizards do not regenerate new spinal cord neurons. Given the disparities in lizard vs salamander NSC positional identities and the markedly decreased axonal staining levels in lizard tail regenerates, we next compared the differentiation capacities of salamander and lizard NSCs into multiple neural lineages. First we demonstrated differences in differentiation capacities *in vivo*. Salamander and lizard spinal cords were transplanted into regenerating tails to observe the differentiation capabilities of transferred NSCs. As expected, original salamander spinal cords proximal to amputation sites exhibited Sox2, β-tubulin (neural), and glial fibrillary acidic protein (GFAP) staining (Figure 33A), while regenerated salamander spinal cords also exhibited these lineages (Figure 33B)– indicating reconstitution of multiple neural lineages. Implanted salamander spinals cord proximal to the amputation site contained no β-tubulin staining (Figure 33E) – as one would expect due to loss of innervation of the neurons – but the regenerated cord again displayed the full range of neural lineages (Figure 33F). These results suggest that even standalone populations of regenerating and differentiating salamander

NSCs are capable of reconstituting multiple neural lineages. These results differ drastically from those observed with lizard NSCs. Original lizard spinal cords proximal to amputation planes exhibited robust β-tubulin and GFAP staining (Figure 33C), while regenerated lizard spinal cords demonstrated only spotty axon staining (Figure 33D). Interestingly, implanted spinal cords, whether they were proximal or distal to the amputation site, did not exhibit any neural staining except for GFAP (Figure 33G,H). These results suggest that the NSC populations within the lizard spinal cord do not have the ability to reconstitute multiple lineages (only $GFAP^+$ astrocytic lineages), and that axons in the regenerate likely arise from extension of axons proximal to the amputation site rather than NSC differentiation.

Again, to probe the behavior of these NSCs outside the regenerative environment, we cultured salamander and lizard neurospheres and subsequently exposed them to differentiation conditions to test their differentiation potential *in vitro*. Strikingly, differentiated salamander neurospheres were positive for β-tubulin (neuron marker) and GFAP (astrocyte marker) [202] while differentiated lizard neurospheres only expressed GFAP (Figure 34 and Figure 47). In addition, we verified the differentiation behavior of lizard NSCs through real time RT-PCR and found that only GFAP was significantly upregulated with concomitant downregulation of neural stem cell marker Sox2 and lineage markers neurofilament heavy (NEFH, neuronal lineage) and Sox10 (oligodendrocyte) (Figure 48). The ability of salamander neurospheres to differentiate into multiple lineages is consistent with observations by Mchedlishvili et al. who described the ability of salamander NSCs to reconstitute both the CNS and PNS [183]. Our findings, however, suggest that lizard NSCs are lineage restricted in their differentiation capacity. These results correlate well with our *in vivo* observations that exogenous spinal cord implants harboring $Sox2^+$ ependymal cells are not able to reform a spinal cord within the regenerated tail – they only

express GFAP just as they do during *in vitro* differentiation. Overall, we see that lizard NSCs are not only restricted to floor plate domains, but they are also restricted to $GFAP^+$ neural lineages – a complete divergence from the versatile salamander NSCs.

Salamander NSCs are ventralized within the lizard tail microenvironment by hedgehog signaling. With the finding that lizard NSCs were restricted in lineage potential and patterning identity, we asked if the introduction of $Pax7^+$ salamander NSCs would be sufficient to induce a different regenerative response in the regenerating lizard ependymal tube. Of note, we also tried the reverse experiments with lizard NSCs injected into salamander tails, but found that they did not survive the aquatic environment. We first verified that isolated lizard NSCs were in fact able to reconstitute the regenerating ependymal tube *in vivo* (Figure 49). NSCs pre-labeled with the membrane dye DiI were injected into original spinal cord ependyma of amputated lizard tails. After 28 days, regenerated tail ependymal tubes were assayed for co-localized on DiI and Sox2 expression. DiI^+ $Sox2^+$ cells were found throughout the ependymal tubes of regenerated tails. These results demonstrated incorporation of injected NSCs into regenerated lizard tail spinal cords.

Next, we sought to induce a different patterning identity in the regenerating lizard ependymal tube through the introduction of $Pax7^+$ salamander NSCs. To avoid rejection of xenogeneic cells and to test for the role of hedgehog signaling in cell fate, we opted to inject DiI-labeled, *in vitro* cultured NSCs into the spinal cords of amputated lizard tails treated with the immunosuppressant Tacrolimus with or without cyclopamine treatment (Figure 50). As controls, lizard NSCs were also injected under the same conditions. Following tail regeneration, DiI-labeled salamander cells were found to have been ventralized within the regenerating ependymal tube (Figure 35A). However, when Shh signaling was inhibited with cyclopamine, the

xenogeneic salamander NSCs retained Pax7-positivity and Shh expression was spatially limited, reminiscent of embryonic dorsal-ventral patterning (Figure 35B). As controls, lizard NSCs were also injected into separate animals and subjected to the same treatments (Figure 35C,D). As expected, regardless of the microenvironment the lizard NSCs remained Shh-positive. These results taken together indicate that the native microenvironment created by regenerated lizard spinal cord NSCs is non-conducive to roof plate differentiation given its strong ventralizing Shh expression.

Salamander NSCs differentiate into neural lineages within the lizard microenvironment. Lastly, we tested the ability of salamander NSCs to differentiate into neurons within the microenvironment of the regenerating lizard tail (Figure 36). Salamander NSCs were expanded *in vitro*, labeled with DiI, and injected into amputated lizard tails during treatment with Tacrolimus. Regenerated tails were then assayed for differentiation of DiI-labeled cells intro neuronal and astrocyte lineages. As controls, lizard NSCs were injected under the same conditions into lizard tails, and salamander NSCs were also injected back into salamander tails to verify their functionality in the microenvironment of the regenerating salamander tail. Note: The condition involving injection of DiI-labeled lizard cells into salamander tails was attempted, but lizard cells did not survive within salamanders and were not detected in regenerate salamander tails. As expected based on findings by Mchedlishvili et al [183], DiI-labeled salamander NSCs injected into salamander tails were able to differentiate into neurons (evidenced by βIII-Tubulin/DiI co-localization) and astrocytes (GFAP/DiI co-localization) (Figure 36A,B). Interestingly, DiI-labeled salamander NSCs injected into lizard tails retained their abilities to differentiate into both neurons and astrocytes (DRGs were not observed) (Figure 36C,D). In contrast, DiI-labeled lizard NSCs injected into lizard tails expressed only GFAP with

characteristic absence of β-tubulin (Figure 36E,F). Instead, we observed sparse β-tubulin^{+} DiI^{-} axons running within the regenerated spinal cord, presumably derived from extensions of the axons proximal to the amputation site (Figure 36E). These results suggest that lizard Sox2^{+} GFAP^{+} NSCs only contribute to the Sox2^{+} GFAP^{+} cells of the ependymal tube, and based on our observations, are not found in any other neural structure, again indicating a restriction in neural differentiation capacity compared to salamander NSCs.

The effect of the regenerated lizard and salamander tail microenvironments on differentiation of DiI-labeled salamander NSCs into roof and floor plate lineages were also tested (Figure 51). Salamander NSCs injected into salamander tails contributed to both Pax7+ roof plate and Shh+ floor plate domains (Figure 51A). In contrast, both salamander and lizard NSCs injected into lizard tails exhibited Shh expression and no indication of Pax7 expression (Figure 51B,C). Overall, these results indicate that salamander NSCs retain their ability to differentiate into neurons despite taking on floor plate identity within the ventralizing regenerated lizard tail microenvironment and suggest that the inability of lizard NSCs to differentiate into neural linages is a property inherent to lizard NSCs and not a product of the lizard tail microenvironment.

Discussion

In the present study, we examined the role of Sox2-positive NSCs in driving divergent tail regeneration outcomes in lizards versus salamanders. These NSCs are critical to regeneration, as newly regenerated spinal cord cells are wholly derived from NSCs in both lizards and salamanders. The first clues that phenotypic differences exhibited by the regenerated lizard tails were linked to deficiencies in NSC populations were based on observations that salamanders regenerate roof plate structures, in particular sensory neurons, while lizards do not. Further investigation revealed that salamander and lizard NSCs are distinct populations of cells with differing regional identities and differentiation capabilities. NSC hedgehog signaling is responsible and necessary for correct establishment of dorsoventral progenitor domains within the regenerating ependymal tube of salamanders. In addition, the Shh signals produced by both the salamander and lizard ependymal tubes are responsible for patterning the axial skeletons in the regenerated tails of both these species, similar to the induction and patterning of the axial skeleton by the embryonic neural tube during development [185,196–198,201]. Here, we show that the floor-plate restricted differential potential of lizard NSCs results in lack of dorsoventral patterning and roof-plate structures within the lizard regenerate. Thus, the disparities between both the regenerated lizard central nervous and skeletal systems compared to those of regenerated salamander tails can be linked to distinct differences in NSC populations.

Salamanders and lizards present distinct models of regeneration, as evidenced by the lack of roof plate-associated structures in lizard regenerates (Figure 27 and Figure 38). On examination of the ependymal tubes, we confirm that as reported by Schnapp et al. and Mchedlishvili et al. the salamander ependymal tube expresses floor plate and roof plate markers *in vivo* [183,185], while we see that the lizard only expresses floor plate markers (Figure 28 and

Figure 39). However, *in vitro* we found that salamander NSCs exhibit an exclusively default roof plate expression that is dependent on Shh signaling to ventralize patterning (Figure 29 and Figure 41). This dependency is reminiscent of the fine balance of patterning molecules in the embryonic neural tube, and we also saw this *in vivo* where the ependymal tube dorsalizes in the absence of hedgehog signaling and floor plate structures such as the cartilage rod are lost (Figure 30, Figure 31, and Figure 45), as demonstrated earlier by Schnapp et al as well [185]. This is in contrast to adult lizard ependymal tube and NSCs, which only express floor plate marker Shh *in vitro* and *in vivo* (Figure 28, Figure 29, and Figure 39, Figure 41), which correlates well with our previous studies [196,201]. (Of note, dorsoventral patterning of the embryonic lizard neural tube resembles those of the spinal cord and ependymal tube in salamander, a species that exhibits neoteny. However, this resemblance is limited to neuroanatomy, not regenerative strategy, as axolotls are amphibians while lizards are amniotes) Neither lizard ependyma nor NSCs dorsalize in response to abolished hedgehog signaling, although Shh-dependent cartilage tube formation is inhibited *in vivo* upon treatment with cyclopamine (Figure 30, Figure 31, and Figure 45). Indeed, SAG treatment in salamander tails mimics the natural rampant hedgehog signaling in lizard tails and results in ependymal tube dorsoventral patterning similar to the lizard regenerate, whereas cyclopamine treatment in lizards fails to abolish the patterning effects of unchecked Shh signaling and does not cause the regenerated tail to become more faithful to the original. This discrepancy in NSC activity clearly points to a difference in NSC behavior. Overall, the observations *in vitro* and *in vivo* are congruent with the structures and segmentation seen in the corresponding regenerates [190,194,195], and suggest that NSCs are responsible for inducing and patterning the lizard and salamander regenerate.

The observations that salamander NSCs exhibit a default roof plate identity *in vitro* while lizard NSCs default towards a floor plate identity raises the question of whether floor-plate cells are being out-competed *in vitro*. Taking a look at EdU staining *in vitro*, we see evidence that this could potentially be the case: 42.8% of roof-plate salamander NSCs are actively proliferating after 2 hours Edu incorporation whereas only 7.9% of floor-plate lizard NSCs are (Figure 42). In addition, *in vivo* EdU staining over a course of 8 weeks demonstrates that while in general the salamander is more proliferative (particularly at later time points like 8 weeks), it seems that roof plate-localized $Sox2^{+}$ cells are more proliferative than floor plate cells, especially in more proximal tail regions. However, the default roof plate identity could also be due to a lack of inductive signal for hedgehog expression that may be present ventrally within the salamander microenvironment but is lost when NSCs are isolated for *in vitro* culture. A full study on the proliferative capacities of these populations as they pertain to regeneration is beyond the scope of this study and will be addressed in future studies.

Interestingly, we found the differentiation potential of lizard NSCs to be limited when compared to the salamander [183]. Indeed, *in vitro* assays of differentiation and *in vivo* spinal cord transplantation show that lizard NSCs have limited ability to take on terminal neural fate (Figure 33, Figure 34, and Figure 47). Other studies suggest that proliferating neural stem/progenitor are responsible for neurogenesis in regenerating lizard tails, but we observe that neurogenesis originates from the proximal spinal cord independent of resident NSCs [203,204]. This in part explains the lack of sensory and motor neuron regeneration in the spinal cords of newly formed lizard tail. Instead, sensory nerves of regenerated lizard tails arise from hypertrophied dorsal root ganglia proximal to the amputation site similar to mammal peripheral nerve regeneration [190,194,195]. The lack of lizard NSC neural differentiation capabilities represents a divergence from

cognate neural stem cells capable of forming multiple neural lineages, even among non-regenerating mammals [205–212]. A possible explanation for the restriction in lineage capabilities could lie in the fact that the lizard tail spinal cord originates from a secondary neural tube formed from a mesodermal source whereas the salamander tail spinal cord forms as part of the primary neural tube of ectodermal origin. Although lizard NSCs do not differentiate into neurons, they still reconstitute the regenerating ependymal tube similar to salamander NSCs (Figure 36E,F and Figure 49). However, lizard NSCs contribute to a strongly ventralizing environment, as evidenced by salamander neurosphere ventralization within the lizard tail (Figure 35A and Figure 51). Only with hedgehog signaling blockade is roof-plate expression maintained and spatially segregated patterning observed within the regenerated lizard tail environment, which points to a possible pathway to restore appropriate patterning in the regenerate.

These observations and findings beg the question: what is the identity of lizard NSCs? Curiously, it is known that neural differentiation from stem cells, in particular oligodendrocyte lineage, is dependent on Shh expression in various species, including mice and zebrafish [213,214]. At the same time, Shh has been shown to inhibit neural differentiation while upregulating proliferation in postmitotic precursor neural cells at late fetal stages (of note, Shh overexpression is also thought to be responsible for some primitive neuroectodermal tumors) [215,216]. This is further complicated by the finding that Shh signaling requires upregulation of Sulfatase1 in a temporal fashion to effectively induce neural progenitors in zebrafish [217]. We posit that lizard NSCs are in fact “cognate” NSCs that lack expression of a regulating gene for Shh expression, which leads to suppression of differentiation and the phenotypically non-identical patterns of tail regeneration observed. This partly stems from observations that neotenic salamander NSCs are able to differentiate into neurons even after being ventralized by the lizard microenvironment,

indicating that the "defect" is likely intrinsic to the lizard NSCs (Figure 36 and Figure 51). In addition, the fact that lizard NSCs in original adult tails are solely floor-plate while embryonic tails express all domains hint that perhaps expression of a gene may be lost in adulthood (of note, axolotol NSCs have been found to express Nogo-A and Nogo receptor during regeneration, which could potentially also be genes of interest)[218] (Figure 28 and Figure 39). Future studies will therefore probe the identities of embryonic lizard NSCs vs adult lizard NSCs. However, for now we recognize that these cells are not true NSCs, and we find the term "Sox2-positive ependymal progenitor cells" to be more fitting for this population until further evidence proves otherwise.

In studying lizards vs. salamanders, we seek to discover the key pathways that delineate the species in terms of regeneration potential in order to shed light on pathways lost in mammalian healing. We have demonstrated here that Sox2-positive NSCs are in part responsible for the lack of patterning observed in the lizard regenerate. We recognize that an inherent limitation in our study was our inability to target only NSC cell populations *in vivo* to knock down Shh expression in a localized manner to really probe the sole contribution of the NSCs to patterning. Unfortunately, given the reproductive cycle of the lizard, transgenic approaches are not yet available to us. We will look towards developing techniques to implant NSCs/neurospheres into the regenerating spinal cord to overcome these limitations, and future studies will now focus on modulating lizard NSC behavior and probing their identity in order to effect improved regeneration.

Materials and Methods

All reagents/chemicals were purchased from Sigma Aldrich (St. Louis, MO, USA) unless otherwise specified.

Salamander and lizards. All experiments were carried out with the salamander *Ambystoma mexicanum* and repeated with two lizard species, the mourning gecko *Lepidodactylus lugubris* and the green anole *Anolis carolinensis*. The choice to include the two lizard species is twofold: First, the gekkonid *L. lugubris* and the iguanid *A. carolinensis* represent the two main lizard families used in regeneration research, and their simultaneous inclusion and the fact that we observed nearly identical behaviors in the cell and tissue types tested allowed for higher confidence that the conclusions made here apply to regenerative lizards as a broad group. Second, distinctive traits exhibited by each species facilitate specific experimental methods. For example, the calcified cartilage tubes of regenerated *Anolis carolinensis* tails facilitated spinal cord implantation studies, while the high productivity of the parthenogenetic *Lepidodactylus lugubris* allowed for the generation of enough source material for generating NSCs used in injection studies. All lizard and salamander studies were performed according to the guidelines of the Institutional Animal Care and Use Committee at the University of Pittsburgh, protocol numbers 15114947, 16128889, and 18011476. In this study, we used adult lizard and salamander tail regenerates at 2, 4, and 8 weeks post-amputation. Lizards and salamanders follow similar time courses in their tail regenerations (Figure 37) and comparing time-matched samples limited bias during inter-species comparisons.

Isolation of NSCs and generation of neurospheres. To generate lizard and salamander neurospheres, spinal cords were isolated from original lizard and salamander tails, and dissociated and expanded as previously reported [196,201]. Briefly, the spinal cords were cut into

small pieces, digested, filtered, myelin was carefully aspirated, and lastly the pellet was resuspended in neurosphere medium and plated at a density of approximately 40,000 cells/well. After 4 weeks, primary neurospheres were utilized for further experiments. See SI text for further information.

Injection of neurospheres. After 4 weeks in culture, neurospheres were collected, trypsinized, and resuspended in phosphate buffered saline (PBS) (Gibco, Waltham, MA, USA). To track the cell *in vivo* they were labeled with DiI-labeling with Vibrant CM solution (Invitrogen, Carlsbad, CA, USA) according to manufacturer's instructions, and resuspended at a density of 10,000 cells/µl for injection into the ependymal tube. Recipient animals were treated with 50µl intraperitoneal injection of Tacrolimus (Selleckchem, Houston, TX, USA) Q48hrs at a concentration of 20µg/ml. 2-3µl of cell suspension containing 10,000 DiI-labeled NSC/µl were injected into the spinal cord with a 36G needle, and the animals were allowed to return immediately to their enclosure and resume normal activities. See SI text for further information.

Injection Regimen. Salamanders were anesthetized prior to intraperitoneal injection by exposure to Benzocaine (RND Center INC. La Joya, Ca, USA) at a concentration of 0.5mg per liter and allowed to recover from anesthesia in fresh water prior to returning to their enclosure. Lizards were not anesthetized prior to injection. Injection regimen for treatment groups consisted of intraperitoneal injections every other day for three weeks of either Shh agonist (SAG) (Selleckchem), Cyclopamine (LC Laboratories, Woburn, MA, USA), or vehicle control as follows: SAG group – 50µl to 100µl of SAG at a concentration of 800µg/ml [219]; Cyclopamine group – 50µl to 100µl of cyclopamine at a concentration of 500µg/ml. Vehicle control - 100µl of 2% dimethyl sulfoxide (DMSO)(Life Technologies, Carlsbad, CA, USA) for molecular biology diluted in PBS (Gibco).

Differentiation Assay. Neurospheres were differentiated by plating onto glass slides coated with laminin /poly-l-lysine and culturing in neurosphere medium without bFGF and heparin (standard differentiation medium). An oligodendrocyte favoring protocol was also used, which involved culturing in standard differentiation medium with supplementation of SAG (50 ng/mL) and PDGF (25 ng/mL) (Peprotech, Rocky Hill, NJ, USA). After two weeks of culture, samples were fixed in 4% PFA and processed for IHC.

Tail Sample Collection. Samples were collected after two, four, or eight weeks following original tail amputation. Salamanders were anesthetized by exposure to Benzocaine (RND Center INC.) at a concentration of 1mg per liter. Regenerated tails were amputated with a number 22 scalpel blade. The animals were allowed to recover from anesthesia in fresh water prior to returning to their enclosure and normal activity. Lizard tails were collected by amputation with a number 22 scalpel blade followed by immediate return to enclosure and normal activity.

Immunohistochemistry (IHC). Lizard and salamander tissue samples were analyzed by IHC as previously described [220]. See Table 3 for IHC antibody specifics. All IHC images of sagittal sections are presented dorsal towards the top, ventral bottom, distal right, and proximal left. Transverse sections are presented with dorsal on top and ventral on bottom.

Statistical Analysis. Statistical analysis was performed using Prism 7 with one or two-way ANOVA with pairwise Tukey's multiple comparison test for data with multiple groups. A P value of <0.05 was deemed to be statistically significant. All values and graphs are shown as mean ± SD.

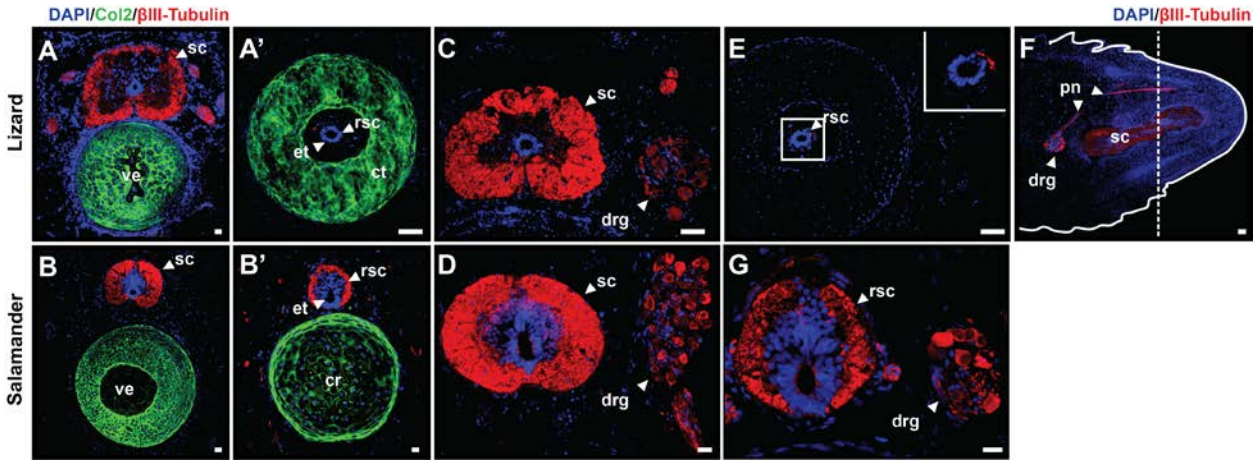

Figure 27. Salamanders (*A. mexicanum*) regenerate spinal cords with roof plate-associated structures while lizard (*L. lugubris*) do not. Collagen Type 2 and βIII-Tubulin immunostaining of original lizard and salamander tail cross sections **(A,B)** and regenerated lizard and salamander tail cross sections demonstrating cartilage tube in lizards and cartilage rod in salamanders in regenerates, respectively **(A', B'). (C, D)** βIII-Tubulin immunostaining of original lizard and salamander tail spinal cord cross sections along with associated dorsal root ganglia. **(E-G)** Immunostaining for βIII-Tubulin in regenerated lizard **(E, F)** and salamander **(G)** tails. Lizard peripheral nerves are derived from existing nerves proximal to the amputation site (marked with a dashed line), while salamanders regenerate discrete dorsal root ganglia. All regenerates are 8 weeks post-amputation. c, cartilage; cr, cartilage rod; ct, cartilage tube; drg, dorsal root ganglion; et, ependymal tube; fp, floor plate; pn, peripheral nerve; rp, roof plate; rsc, regenerated spinal cord; sc, spinal cord; ve, vertebra. Scale bar = 50 μm.

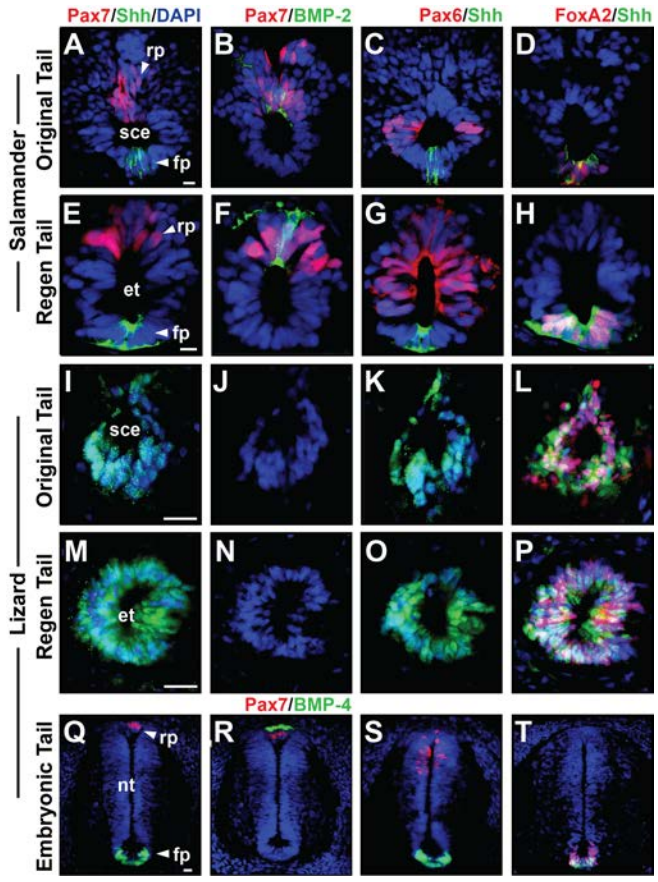

Figure 28. Salamanders (*A. mexicanum*) regenerate ependymal tubes with roof plate, floor plate, and lateral domains while lizards (*L. lugubris*) contain floor plate only. Cross sections of **(A-D)** original salamander tail spinal cord ependyma, **(E-H)** regenerated salamander tail ependymal tubes, **(I-L)** original lizard tail spinal cord ependyma, **(M-P)** regenerated lizard tail ependymal tubes, and **(Q-T)** embryonic lizard tail neural tubes immunostained for roof plate (Pax7, BMP-2/4), lateral plate (Pax6), and floor plate (FoxA2, Shh) markers. Original and regenerated salamander ependymal tubes exhibit roof, lateral, and floor plate domains, while original and regenerated lizard ependymal tubes only contain floor plate. The embryonic lizard tail neural tube, however, also contains all three domains. All regenerates are 8 weeks post-amputation. et, ependymal tube; fp, floor plate; nc, notochord; nt, neural tube; rp, roof plate; sce, spinal cord ependyma. Scale bar = 50 μm.

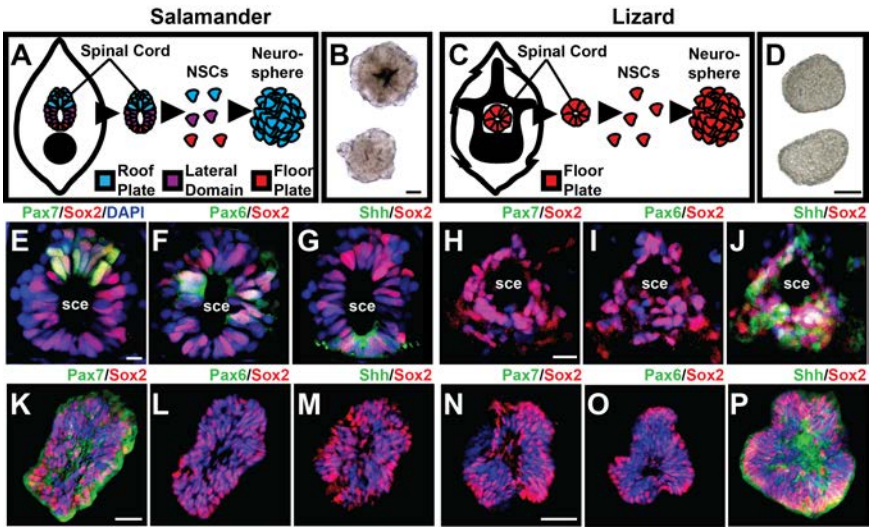

Figure 29. Salamander (*A. mexicanum*) NSCs exhibit roof plate identity while lizard (*L. lugubris*) NSCs exhibit floor plate identity. (A-D) Summary schematic of NSC neurosphere formation: salamanders default to roof plate and lizards default to floor plate. **(B, D)** Light microscopy of neurospheres formed in vitro for salamanders and lizards, respectively. **(E-G)** Roof (Pax7), lateral (Pax6), and floor (Shh) plate immunostaining of Sox2+ NSCs in salamander tail spinal cord ependyma. **(H-J)** Roof, lateral, and floor plate staining of Sox2+ NSCs in lizard spinal cord ependyma. **(K-M)** Roof, lateral, and floor plate staining of in vitro cultured salamander neurospheres. Note the absence of lateral and floor plate markers. **(N-P)** Roof, lateral, and floor plate staining of in vitro cultured lizard neurospheres. Note the absence of lateral and roof plate markers. Neurospheres were isolated from original tails. sce, spinal cord ependyma. Scale bar = 50 μm.

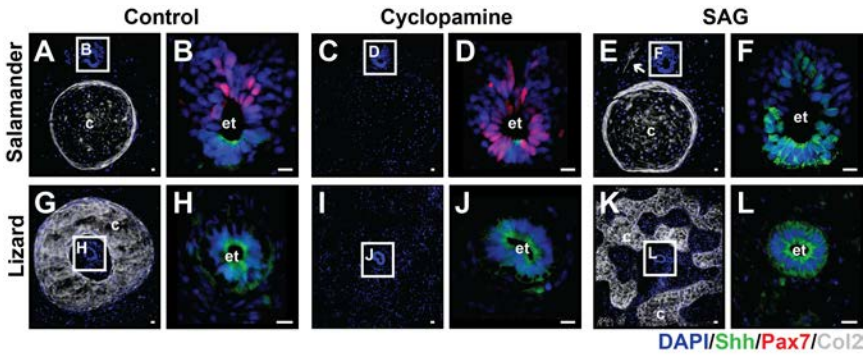

Figure 30. Hedgehog signaling is necessary for the correct establishment of dorsal ventral progenitor domains in the ependymal tube during tail regeneration. Pax7, Shh, and Col2 staining of control regenerated tails **(A,B,G,H)**, cyclopamine-treated regenerated tails **(C,D,I,J)**, and SAG-treated regenerated tails **(E,F,K,L)** in salamanders (A. mexicanum) **(A-F)** and lizards (L. lugubris) **(G-L)**, respectively. Ependymal tubes enclosed in a white box are shown in magnified view to the right of the corresponding image. All regenerates are 4 weeks post-amputation. c, cartilage; et, ependymal tube. Scale bar = 50 μm.

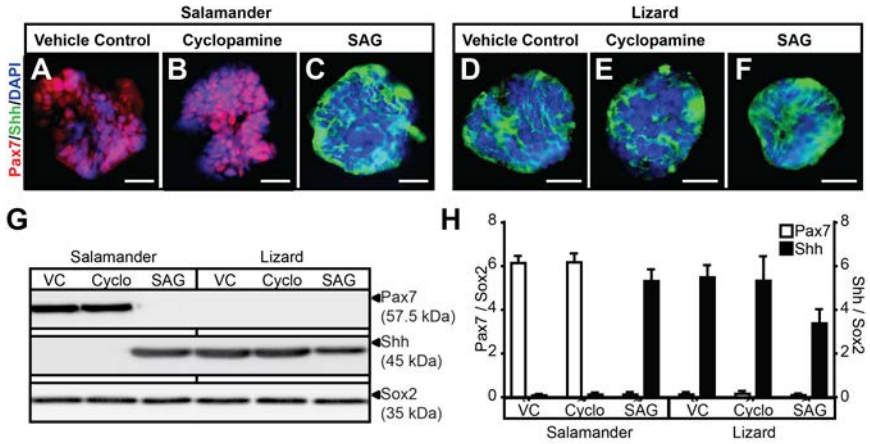

Figure 31. Ventralization of salamander (*A. mexicanum*), but not lizard (*L. lugubris*), neurospheres is regulated by hedgehog signaling. (A-C) Roof (Pax7) and floor plate (Shh) staining of in vitro salamander neurospheres treated with control, cyclopamine, and Shh agonist (SAG). Pax7 and Shh expression is responsive to SAG treatment. **(D-F)** Roof (Pax7) and floor plate (Shh) staining of in vitro lizard neurospheres treated with control, cyclopamine, and Shh agonist (SAG). Shh expression is unaffected by treatments. **(G)** Western blot analysis of Pax7, Shh, and Sox2 in salamander and lizard neurospheres treated with vehicle control (vc), cyclopamine (cyclo), and SAG. **(H)** Quantification of Western blot intensities. Neurospheres were isolated from original tails. N=3. Scale bar = 50 μm.

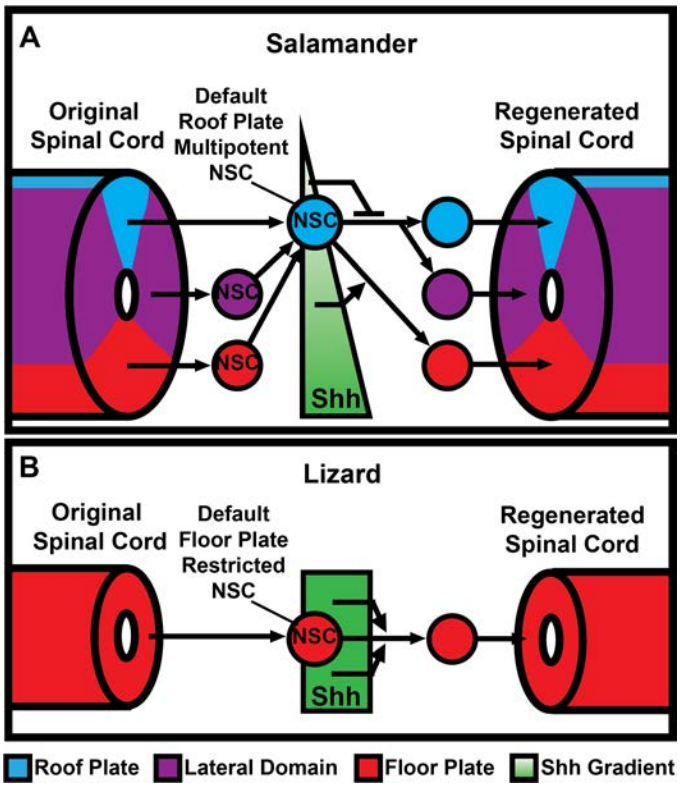

Figure 32. Hypothesized patterning signals found in salamander and lizard NSCs. (Top) The ependyma of the original salamander tails harbor NSCs that contain organized roof, lateral, and floor plate domains, which are default roof plate within their environment and upon explant and culture in vitro. They are responsive to hedgehog signaling and ventralize according to a hedgehog gradient, and in this fashion drive regeneration and patterning in the salamander tail regenerate. **(Bottom)** The lizard original tail ependyma is composed of solely floor plate NSCs, which remain floor plate on explant and culture in vitro. They remain floor plate regardless of perturbations in hedgehog signaling, and pattern the regenerated lizard tail as such.

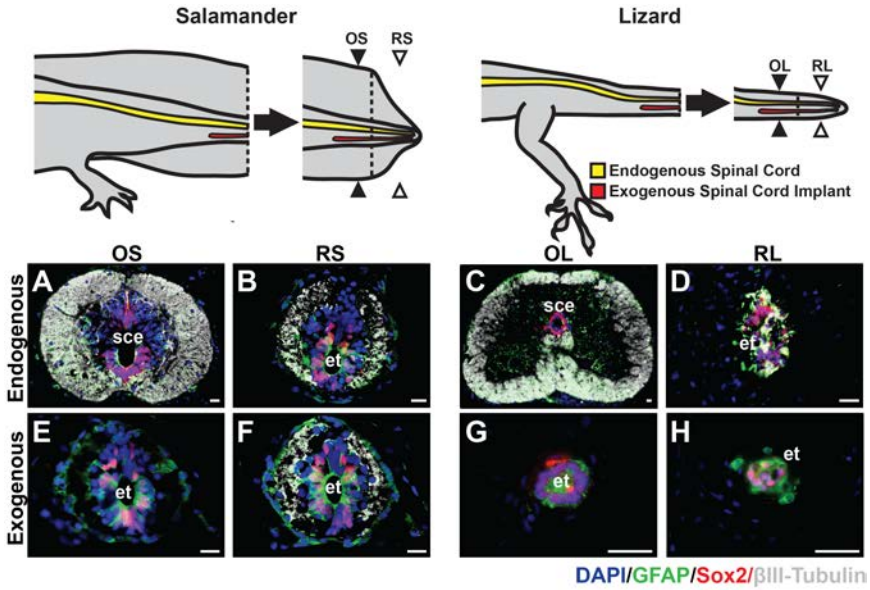

Figure 33. Salamanders (*A. mexicanum*) regenerate new neurons during tail regeneration, while lizards (*A. carolinensis*) do not. Exogenous spinal cords were allogeneically implanted into salamander and lizard tails followed by re-amputation. βIII-Tubulin, GFAP, and Sox2 staining of spinal cords proximal to amputation site **(A,C)/(E,G)** and distal to amputation site **(B,D)/(F,H)** in the endogenous/exogenous spinal cord of the salamander and lizard tail, respectively. Exogenous spinal cords in the salamander are able to reconstitute multiple neural lineages, whereas in lizards they cannot. All regenerates are 4 weeks post-amputation. OL, original lizard spinal cord; OS, original salamander spinal cord; RL, regenerated lizard spinal cord; RS, regenerated salamander spinal cord. Scale bar = 50 μm.

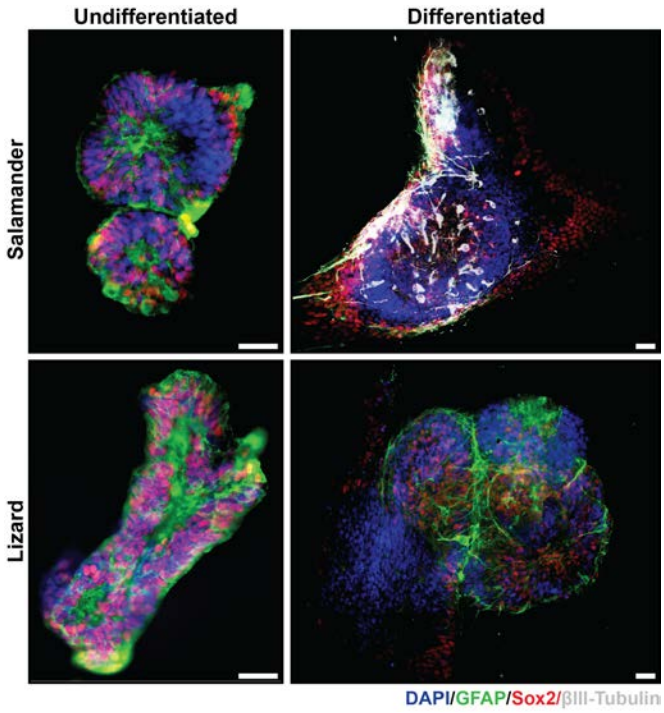

Figure 34. Salamander (*A. mexicanum*) NSCs are capable of neuronal differentiation into neurons whereas lizard (*L. lugubris*) NSCs are not. βIII-Tubulin, glial fibrillary acidic protein (GFAP), and Sox2 staining of differentiated and undifferentiated salamander and lizard neurospheres. Note the inability to form axons. Scale bar = 50 μm.

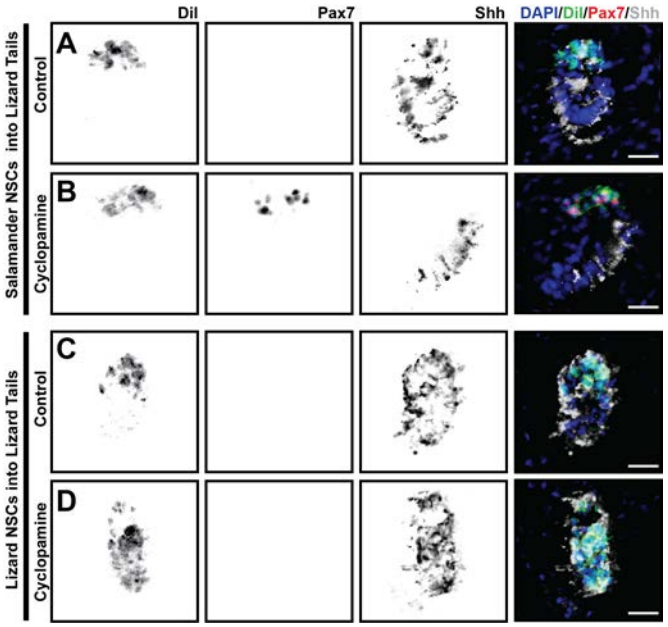

Figure 35. Salamander (*A. mexicanum*) NSCs are ventralized within the lizard (*L. lugubris*) tail microenvironment. Salamander and lizard neurospheres were cultured in vitro, DiI labeled, and injected into the spinal cord of an amputated lizard tail. **(A-D)** Transverse sections of the regenerated ependymal tube stained for roof-plate marker Pax7 and floor-plate marker Shh with or without cyclopamine treatment for the lizards. Note the Pax7-negativity of salamander NSCs in non-cyclopamine treated lizards vs. the corresponding Pax7-positivity and patterning segregation in cyclopamine treated lizards. All regenerates are 2 weeks post-amputation/NSC injection. Scale bar = 50 μm.

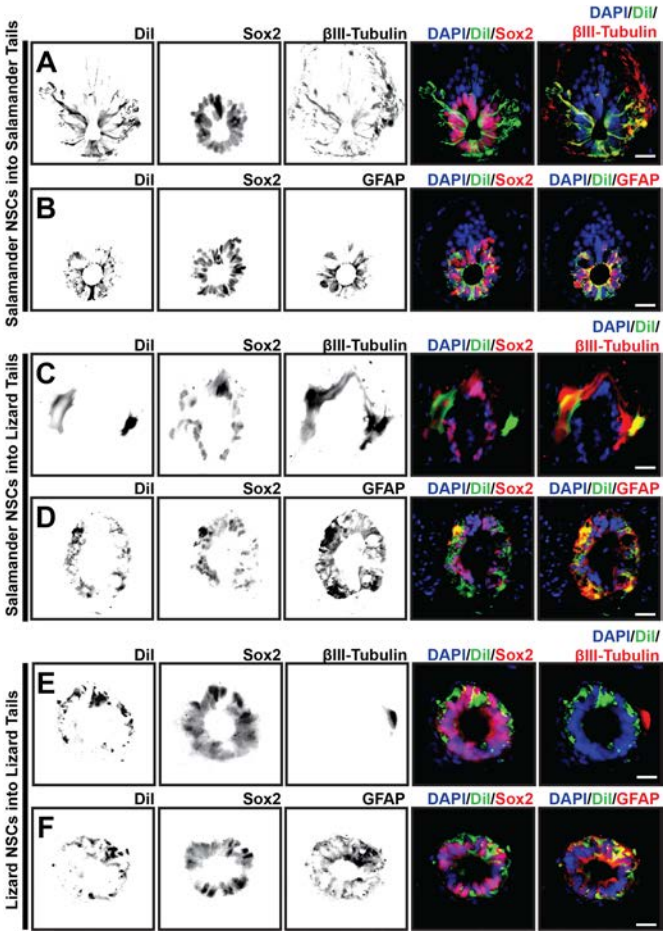

Figure 36. Salamander (*A. mexicanum*) NSCs differentiate into neural lineages within the lizard (*L. lugubris*) tail microenvironment. Salamander and lizard neurospheres were cultured in vitro, DiI labeled, and injected into the spinal cord of an amputated salamander or lizard tail. **(A-F)** Transverse sections of salamander **(A-D)** or lizard **(E,F)** regenerated ependymal tubes stained for Sox2 and βIII-Tubulin **(A,C,E)** or GFAP **(B,D,F)**. Salamander NSCs co-expressed DiI and βIII-Tubulin/GFAP when injected into either salamander or lizard tails. Lizard NSCs did not co-localize expression of DiI and βIII-Tubulin. Of note, lizard NSCs injected into salamander tails were non-viable. All regenerates are 4 weeks post-amputation/NSC injection. Scale bar = 50 μm.

Supplementary Materials and Methods

Animal Technical and Procedural Information. *Ambystoma mexicanum* salamanders utilized were male at 1 year of age, *Lepidodactylus lugubris* lizards were female at 8 months of age, and *Anolis carolinensis* were male at 1 year of age. *A. mexicanum* were purchased from sal-site and used 1 year later (RRID:AGSC_100J)(8-12 cm juvenile). For the parthenogenetic *L. lugubris*, the founding gecko was collected from Hawaii (Poipu Beach, Kauai) in 1988 and exported to Dan Martindale of Chaotic Nights Reptiles. We received 4 geckos in August 2014, and our entire colony is established from these 4 geckos. Lastly, *A. carolinensis* was purchased from Connecticut Valley Biological Supply Company catalog L62406.

All experiments were performed with at least n=3 experimental replicates for each species and timepoint. With the exception of Figure 7, all lizard experiments in main figures were performed with *L. lugubris*, and similar experiments were performed with *A. carolinensis* (presented in the supplemental information) to confirm similarity between lizard species. *L. Lugubris* is an all-female species that is parthenogenetic, diploid, and capable of tail regeneration. As such, it is the only lizard species that possesses the last two traits, and because offspring are genetically identical we can take advantage of cell/tissue transplantation among all animals in a colony without rejection. Hence, we seek to establish the *L. Lugubris* as an equally viable lizard model to the *Anolis carolinensis*.

Due to the lack of autotomy planes in the salamander, we chose amputation to use for both species. Regardless of whether amputation or autotomy occurs, regeneration occurs through the same sequence and outcomes are virtually identical except for some evidence that an autotomized tail may be slightly longer. This trait of reduced axon area is found in both methods

too, and is not specific to the *L. lugubris* as it can be seen in a number of other species such as the *A. carolinensis* and the leopard gecko (*Eublepharis macularius*).

Injection of Neurospheres. After 4 weeks in culture, neurospheres were collected and centrifuged for 5 minutes at 380g. The supernatant was removed and the neurospheres were resuspended in 5 ml HBSS w/o Ca/Mg (HyClone Laboratories, Logan, UT, USA) and centrifuged again. Neurospheres were then resuspended in 550 µl of Trypsin 0.25%/EDTA (Life Technologies) and incubated for 5 min. 10 µl DNAse I at 10 mg/ml were added and the solution was homogenized by pipetting up and down gently with a P1000 pipette for 5 minutes. 55 µl of 50mg/ml Trypsin Inhibitor and 5 ml of neurosphere medium were added. The cell suspension was centrifuged and resuspended in phosphate buffered saline (PBS) (Gibco). To track the cell in vivo they were labeled with DiI-labeling with Vibrant CM solution (Invitrogen) according to manufacturer's instructions. After a 20 minute incubation, cells were washed three times with PBS to remove traces of DiI and resuspended at a density of 10,000 cells/µl for injection into the ependymal tube. Recipient animals were treated with 50µl intraperitoneal injection of Tacrolimus (Selleckchem, Houston, TX, USA) Q48hrs at a concentration of 20µg/ml.

Lizard tails were sprayed with ethyl chloride, air dried, and amputated with a size 22 scalpel 0.5cm from the base. 2-3µl of cell suspension containing 10,000 DiI-labeled NSC/µl were injected into the spinal cord with a 36G needle, and the animals were allowed to return immediately to their enclosure and resume normal activities.

5-ethynyl-2'-deoxyuridine (EdU) incorporation. For *in vivo* incorporation experiments, animals were provided with the thiamine analog EdU for labeling of proliferating cells via intraperitoneal injection (150 µl for salamanders and 50 µl for lizards). EdU (Life Technologies, Carlsbad, CA, USA) was allowed to incorporate into dividing cells for four hours before

sacrifice. Sample were cryosectioned and stained for EdU according to the manufacturer's instructions. For the *in vitro* EdU incorporation experiments, primary neurospheres were cultured for 4 weeks before being exposed to EdU at 10 μm for 2 hours. Samples were then processed for flow cytometry according to manufacturer's protocols with Ghost Dye (Tonbo Biosciences, San Diego, CA, USA) viability stain to sort for live cells.

Isolation and generation of neurospheres. Spinal cords were cut into small pieces and incubated in L15 medium (Gibco, Waltham, MA, USA) containing 30 U/mL papain, 0.5 mg/mL BSA, 0.24 mg/mL cysteine, 40 μg/mL DNase I type IV, and 1.0 mg/mL trypsin inhibitor for 1h at room temperature. The solution was then homogenized by repeatedly passing the solution gently through a 1 mL pipette tip. Digestion was then stopped by adding an equal amount of ovomucoid inhibitor [1.0 mg trypsin inhibitor, 0.5 mg/mL BSA, and 40 μg/mL DNase I type IV in L15 medium (Gibco)]. The cell suspension was then added into 9.4 ml neurosphere medium [2 μg/mL heparin, 20 ng/mL bFGF (RayBiotech, Norcross, GA, USA), 1x ITS (Gibco), and 1x B-27 (Gibco) in DMEM/F12 + Glutamax medium (Gibco)] with 1x Pen/Strep added (Gibco). The solution was then filtered through a 100 μm filter, transferred back into a 15 mL conical tube, and subsequently centrifuged for 5 min at 380×g. The pellet was resuspended in 2 ml 0.9 M Sucrose solution and centrifuged at 750×g for 30 minutes. Myelin was carefully aspirated, and the pellet was resuspended in neurosphere medium and plated at a density of approximately 40,000 cells/well. After 4 weeks, primary neurospheres were utilized for further experiments.

Analysis of Gene Expression by Real-Time RT-PCR. Total RNA of cells residing within spinal cord tissue was isolated using TRIZOL reagent (Invitrogen, Carlsbad, CA, USA) and purified using RNeasy Plus Mini Kit (Qiagen, Germantown, MD, USA). Total RNA of cultured lizard and salamander neurospheres was isolated and purified using RNeasy Plus Mini Kit.

Reverse transcription reactions were performed using Superscript® VILO™ cDNA Synthesis Kit (Invitrogen) according to the manufacturer's manual. Real-time PCR was performed using the SYBR Green Reaction Mix (Applied Biosystems, Foster City, CA, USA) with a StepOne-Plus thermocycler (Applied Biosystems). All sample values were normalized to GAPDH using the $2^{-\Delta\Delta Ct}$ method. See Table 4 for primer sequences.

Quantification of Positive Axon Staining Area. Total positive axon staining area was quantified using Fiji (ImageJ, NIH) applying over/under thresholding to limit analysis to the positive-staining areas.

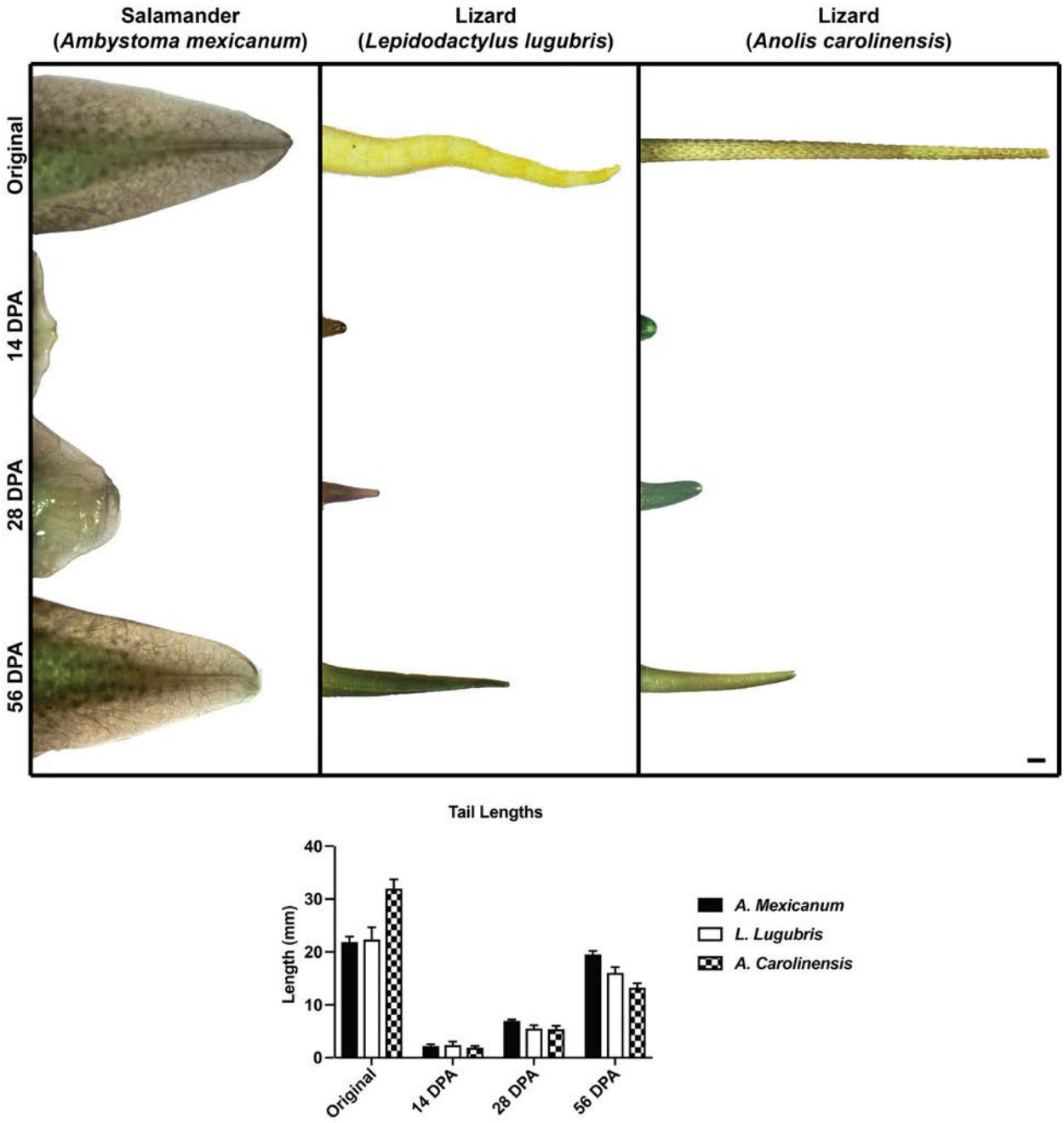

Figure 37. Gross morphology and tail length measurements of regenerating salamander (*A. mexicanum*) and and lizard (*Lepidodactylus lugubris and Anolis carolinensis*) tails. Tails were amputated and measured at various timepoints post-amputation. Scalebar = 2 mm.

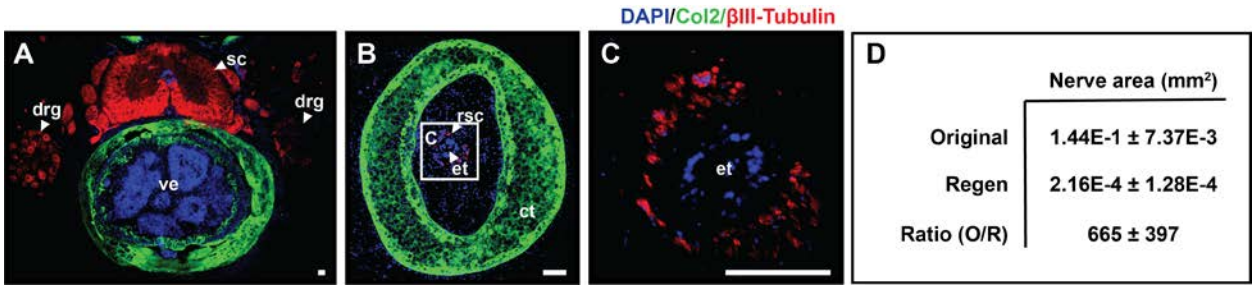

Figure 38. Lizards (*A. carolinensis*) do not regenerate roof-plate derived structures. Collagen Type 2 and βIII-Tubulin immunostaining of original tail cross sections **(A)** and regenerated tail cross sections **(B)** demonstrating the cartilage tube in the regenerates. **(C)** βIII-Tubulin immunostaining of regenerated tail spinal cord cross sections. **(D)** Quantification of total βIII-Tubulin positive staining area in the original and regenerated spinal cords. Note the greatly diminished area of axonal staining compared to original tails. All regenerates are 8 weeks post-amputation. c, cartilage; ct, cartilage tube; drg, dorsal root ganglion; et, ependymal tube; rsc, regenerated spinal cord; sc, spinal cord; ve, vertebra. Scale bar = 50 μm.

Table 2. Quantification of βIII-Tubulin-positive axonal staining area (mm2) in original (O) and regenerated (R) spinal cords for lizard (*L. lugubris*) (L) and salamander tails (*A. mexicanum*) (S).

	Lizard	Salamander	P value (L vs. S)
Original	6.52E-2 ± 3.50E-3	8.03E-2 ± 8.30E-3	p = 0.0079
Regenerated	1.63E-4 ± 1.35E-4	1.78E-2 ± 2.36E-3	p < 0.0001
Ratio (O/R)	401 ± 334	4.52 ± 0.762	p = 0.0276

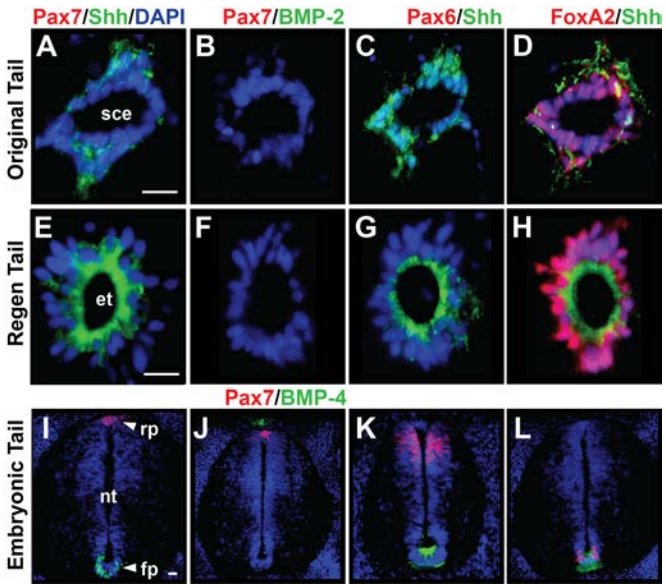

Figure 39. Lizards (*A. carolinensis*) regenerate ependymal tubes with floor plate domains only. Cross sections of **(A-D)** original tail ependymal tubes, **(E-H)** regenerated tail ependymal tubes, and **(I-L)** embryonic tail neural tubes immunostained for roof plate (Pax7, BMP-2/4), lateral plate (Pax6), and floor plate (FoxA2, Shh) markers. Original and regenerated ependymal tubes only contain floor plate. The embryonic lizard tail neural tube, however, also contains all three domains. All regenerates are 8 weeks post-amputation. et, ependymal tube; fp, floor plate; nc, notochord; nt, neural tube; rp, roof plate; sce, spinal cord ependyma. Scale bar = 50 μm.

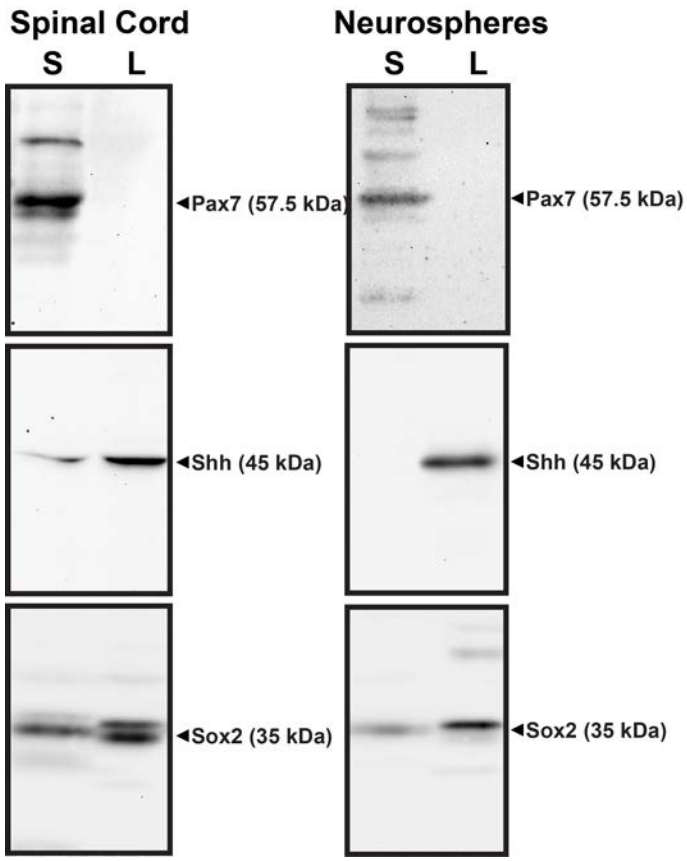

Figure 40. Western blot analysis of Pax7, Shh, and Sox2 in salamander (*A. mexicanum*) and lizard (*L. lugubris*) spinal cords and neurospheres. Pax7 is characteristically absent in lizard spinal cord and neurospheres, while Shh is high in both sources. Salamander spinal cords express both Pax7 and Shh while neurospheres only express Pax7. Sox2 was used to confirm NSC identity and is present in all samples.

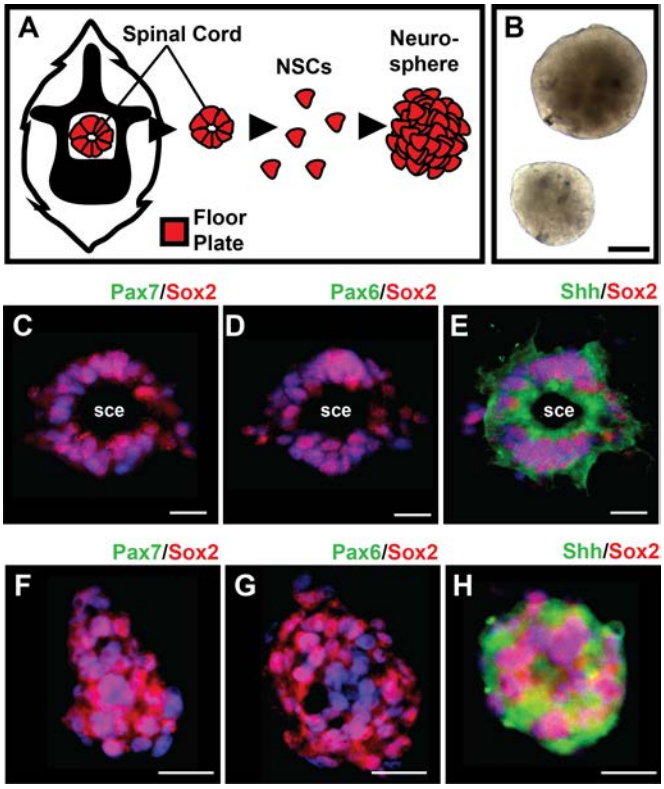

Figure 41. Lizard (*A. carolinensis*) NSCs exhibit default floor plate identity. (A) Summary schematic of NSC neurosphere formation: NSCs default to floor plate. **(B)** Light microscopy of neurospheres formed in vitro. **(C-E)** Roof (Pax7), lateral (Pax6), and floor (Shh) plate immunostaining of Sox2+ NSCs in ependymal tubes. **(F-H)** Roof, lateral, and floor plate staining of in vitro cultured neurospheres. Note the absence of lateral and roof plate markers. Neurospheres were isolated from original tails. sce, spinal cord ependyma. Scale bar = 50 μm.

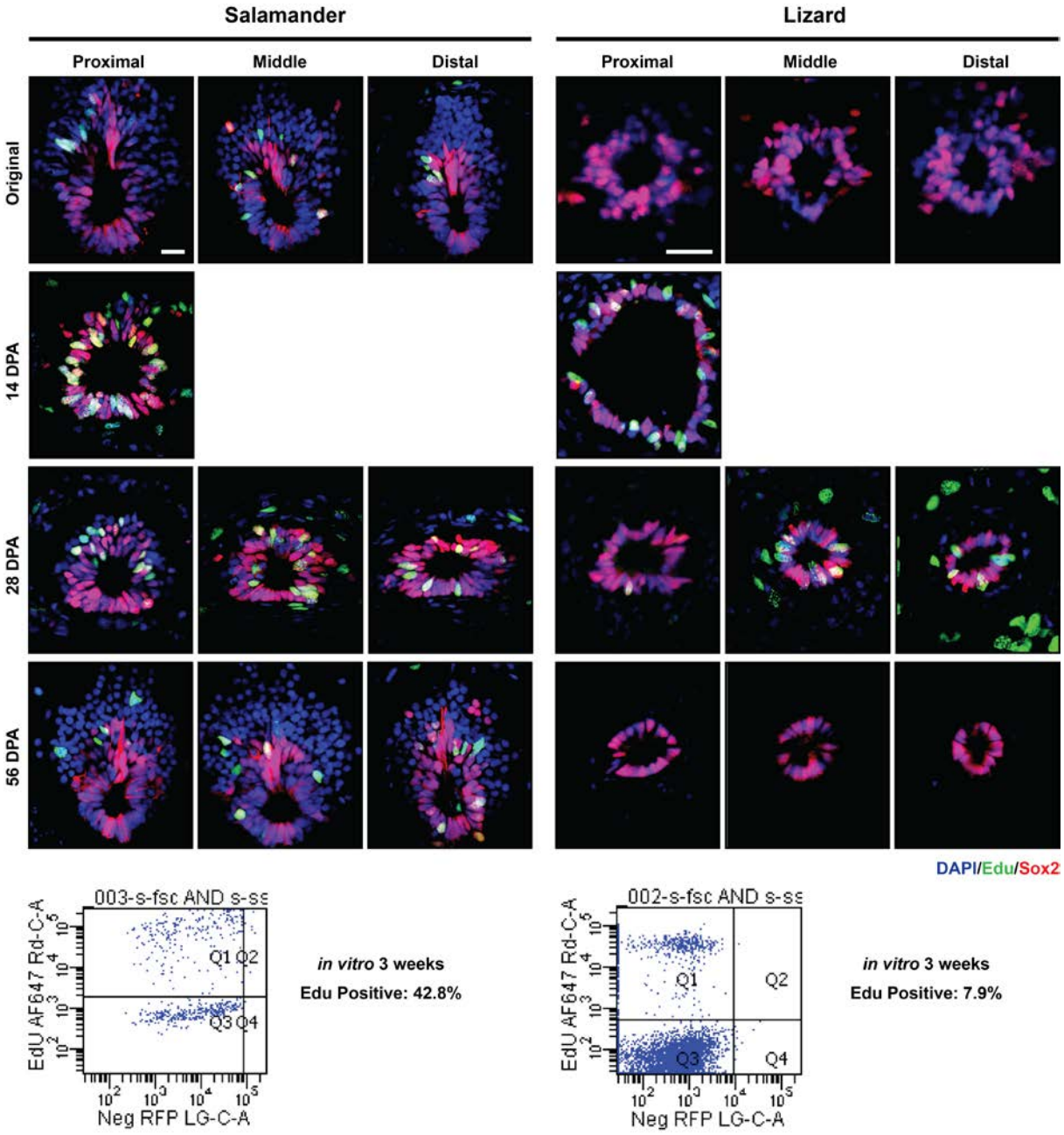

Figure 42. In vitro and in vivo salamander (*A. mexicanum*) and lizard (*L. lugubris*) NSC proliferation assessed by EdU incorporation. Salamander and lizard tails were amputated and allowed to regenerate for the specified timepoints before labeling with EdU and harvest. In addition, NSCs were isolated from slamaanders and lizards and cultured in vitro for 3 weeks before labeling with EdU. In both in vitro and in vivo experiments, salamanders were more proliferative, especially at later timepoints. Scale bar = 50 μm.

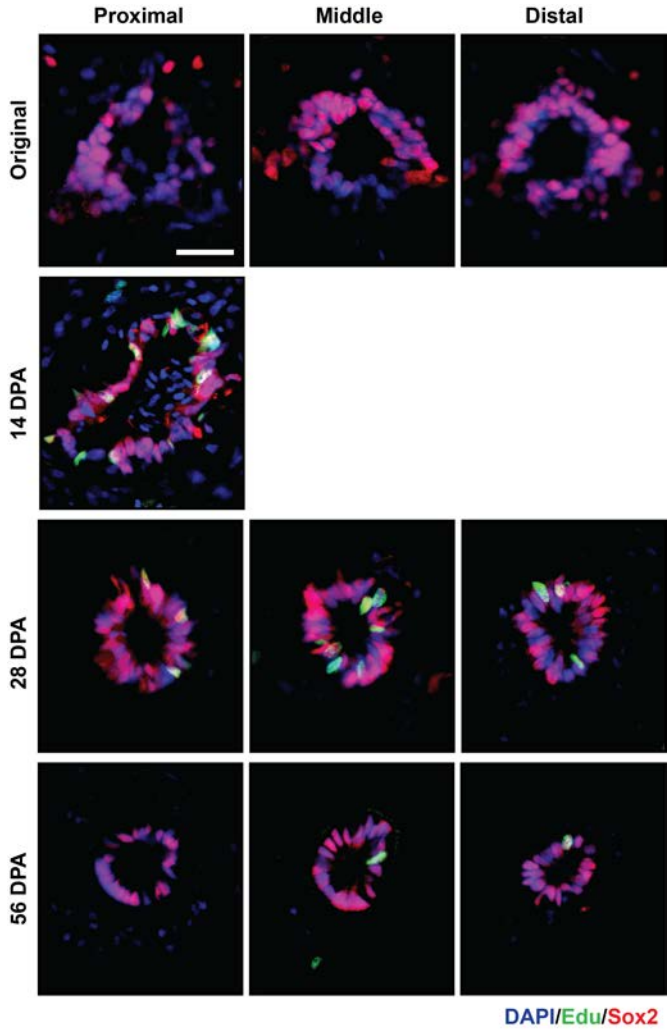

Figure 43. *In vivo* Lizard (*A. carolinensis*) NSC proliferation assessed by EdU incorporation. Tails were amputated and allowed to regenerate for the specified timepoints before labeling with EdU and harvest. Scale bar = 50 μm.

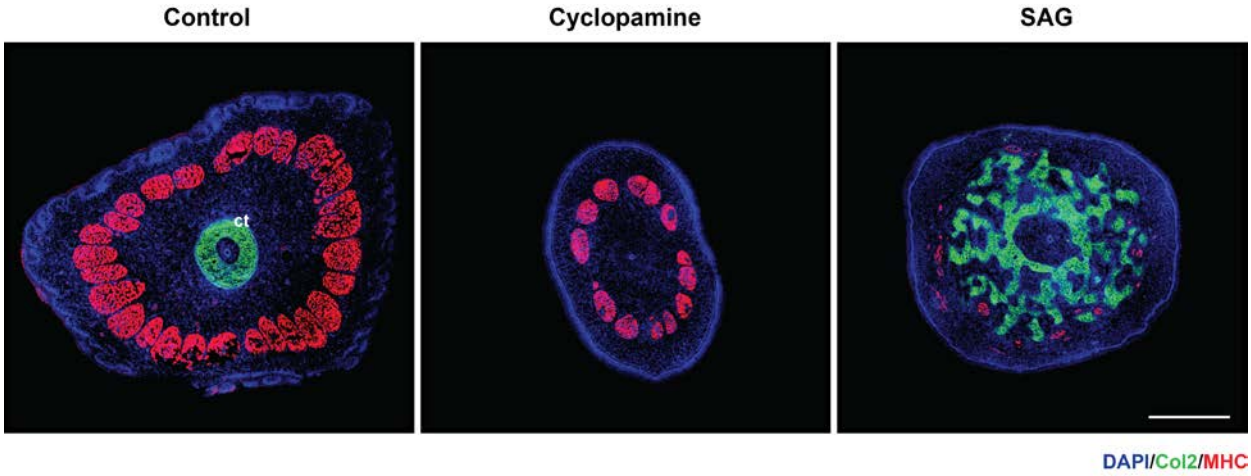

Figure 44. Effect of hedgehog modulation on muscle formation in regenerating lizard (*L. lugubris*) tails. Regenerating lizard tails treated with cyclopamine or SAG were stained for myosin heavy chain (MHC) and Col2. Cyclopamine treatment abolished cartilage formation and decreased the number of muscle bundles observed while SAG treatment resulted in tails with heavily impaired muscle formation and rampant cartilage formation. ct, cartilage tube. Scale bar = 500 μm.

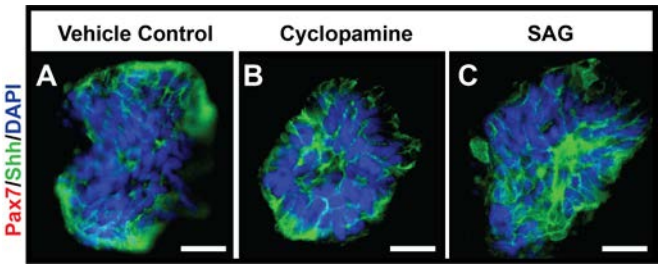

Figure 45. Ventralization of lizard (*A. carolinensis*) neurospheres is not regulated by hedgehog signaling. (A-C) Roof (Pax7) and floor plate (Shh) staining of in vitro neurospheres treated with control, cyclopamine, and Shh agonist (SAG), respectively. Shh expression is unaffected by treatments. Neurospheres were isolated from original tails. Scale bar = 50 μm.

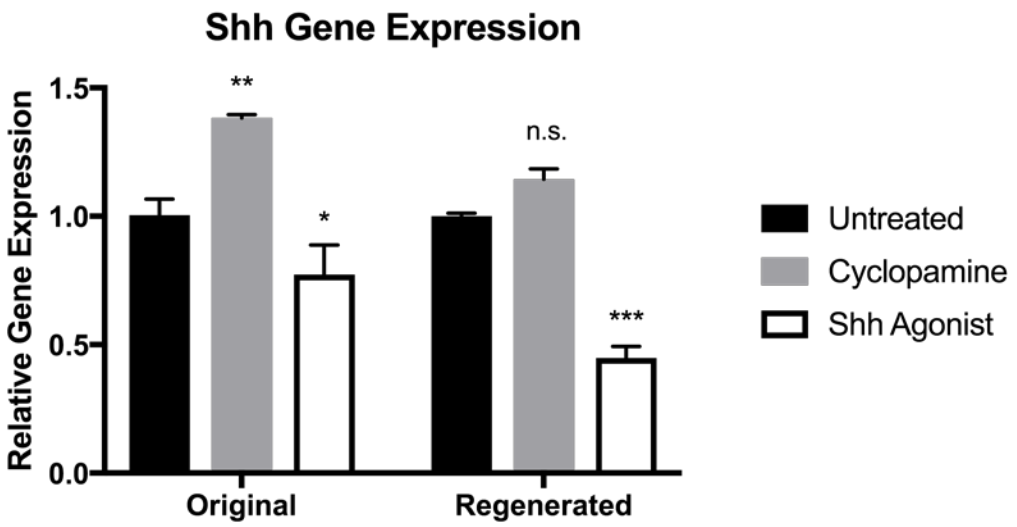

Figure 46. RT-PCR analysis of Shh gene expression in cyclopamine and SAG treated lizard (*L. lugubris*) neurospheres. Neurospheres derived from original and regenerated lizard spinal cords were left untreated or treated with cyclopamine or SAG in culture medium. Within the original and regenerated neurospheres, Shh gene expression was normalized to their untreated groups, respectively. Cyclopamine treatment caused a significant increase original neurospheres that was not seen in the regenerate by two-way ANOVA. This could be due to behavioral differences between original and regenerated neurospheres (i.e. higher basal production of Shh coupled with a negative feedback mechanism leading to a greater cyclopamine effect in original neurospheres). Another consideration is that the non-significance for fold increase in cyclopamine-treated regenerated neurospheres is due to the pooled variation from two-way ANOVA, but is significant when one-way ANOVA is run on original and regenerated separately. Regenerated neurospheres are derived from mature regenerates (>8 weeks post-amputation). All statistical comparisons are between treatments and their respective control. *, $p<0.05$. **, $p<0.005$. ***, $p<0.0001$. n=3 in all conditions.

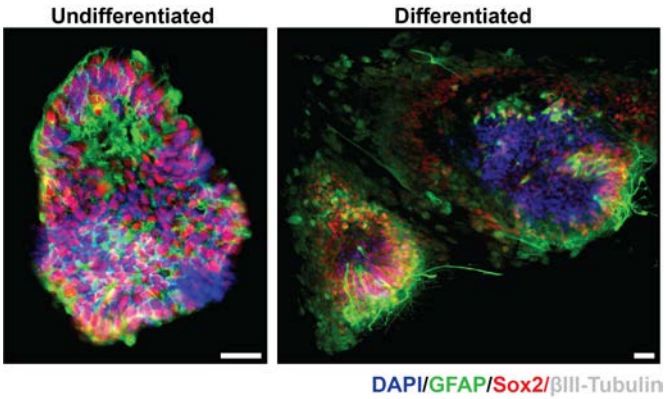

Figure 47. Lizard (*A. carolinensis*) NSCS are not capable of differentiation into neurons. βIII-Tubulin, glial fibrillary acidic protein (GFAP), and Sox2 staining of differentiated and undifferentiated neurospheres. Note the inability to form axons. Scale bar = 50 μm.

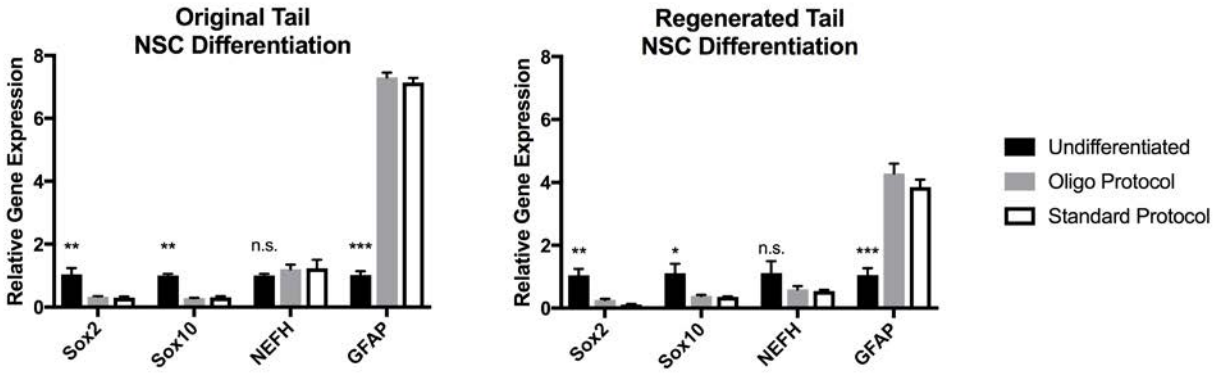

Figure 48. RT-PCR analysis of Sox2, Sox10, NEFH, and GFAP in undifferentiated and differentiated lizard (*L. lugubris*) NSCs. NSCs derived from original and regenerated spinal cords were subjected to standard differentiation protocol and oligodendrocyte differentiation protocol to push differentiated cells towards oligodendrocyte lineage. All gene expression levels within each neurosphere source/gene grouping (for example, Original NSC/Sox2) were normalized to the undifferentiated condition within the grouping. Regenerated neurospheres are derived from mature regenerates (>8 weeks post-amputation). All statistical comparisons were between undifferentiated condition and both differentiation protocols within each grouping. *, $p<0.05$. **, $p<0.005$. ***, $p<0.0001$. n=3 in all conditions.

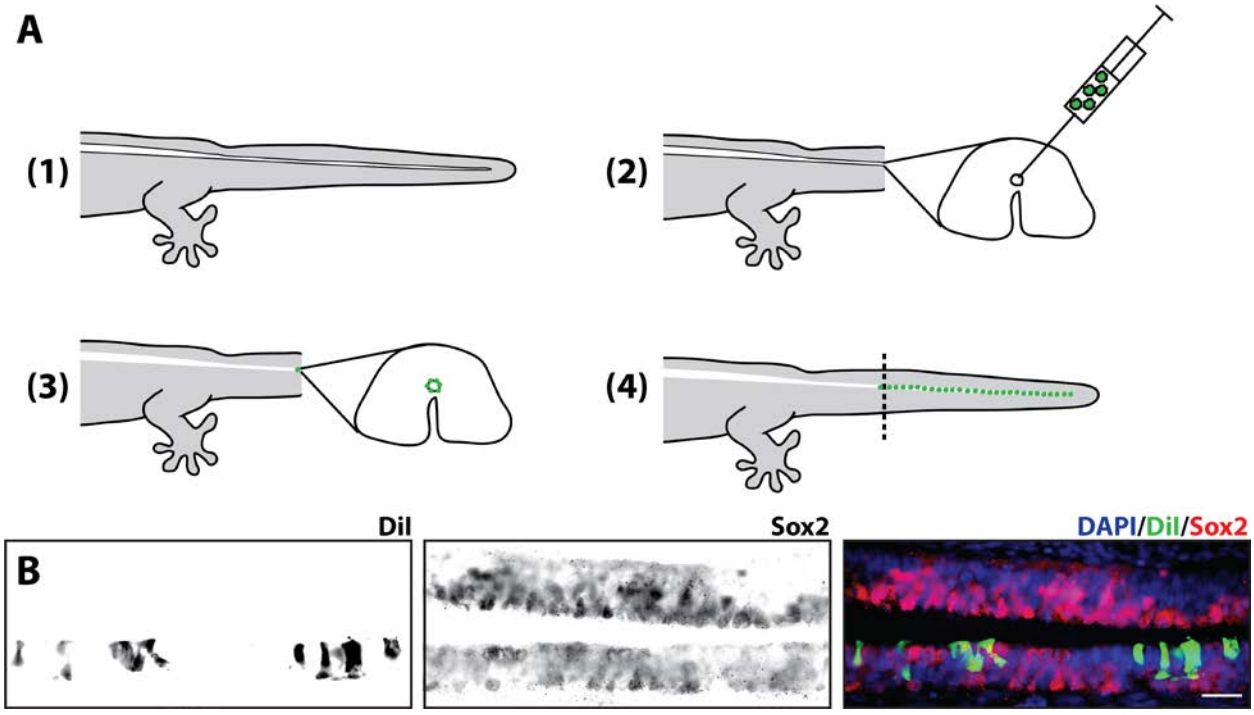

Figure 49. Injected Sox2+ NSCs contribute to the regenerated lizard ependymal tube. (A) Schematic of DiI-labeled NSC injection into a lizard tail. An amputation is made, followed by injection of DiI-labeled NSCs into the spinal cord and subsequent regeneration. **(B)** Longitudinal section of regenerated ependymal tube (28 DPA) stained for Sox2. Sox2+ DiI+ cells are observed within the regenerated ependyma. Scale Bar = 50 μm.

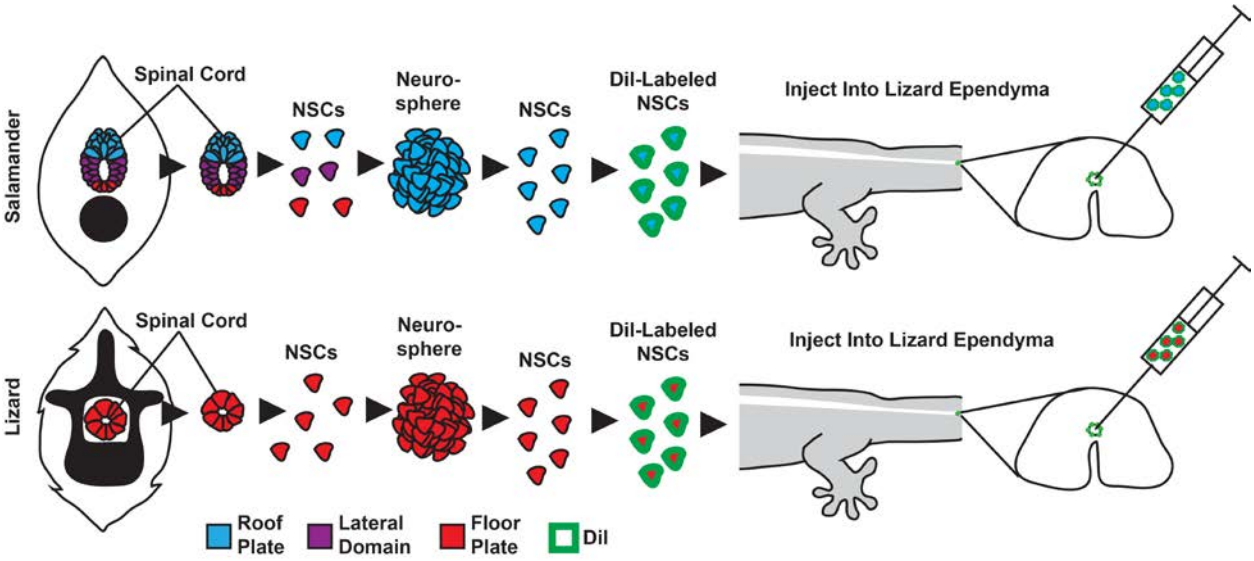

Figure 50. Injection of salamander and lizard Sox2+ NSCs into tacrolimus-treated lizard tails. (A) Schematic of DiI-labeled salamander and lizard NSC injection into a tracrolimus-treated lizard. Neurospheres are cultured in vitro and injected into the spinal cord of an amputated lizard tail.

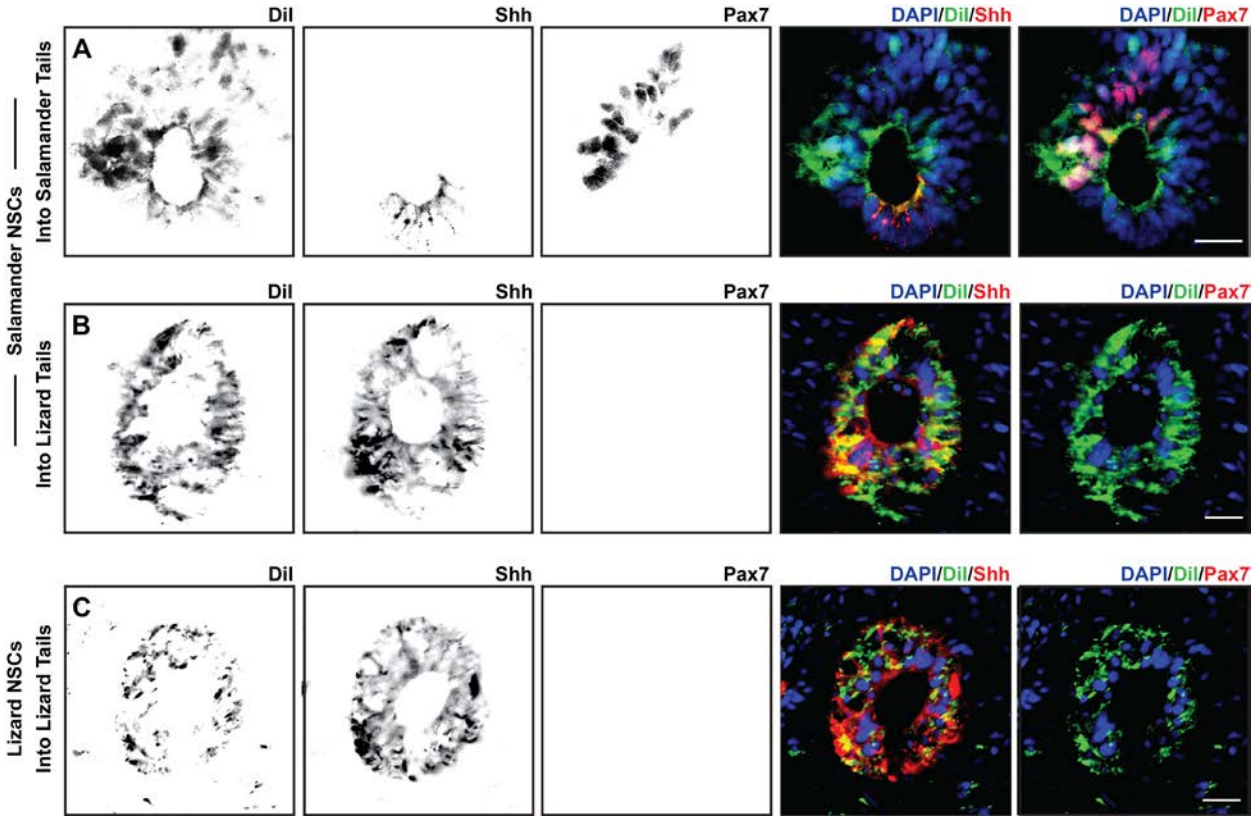

Figure 51. Salamander (*A. mexicanum*) NSCs are ventralized within the lizard (*L. lugubris*) tail microenvironment at 4 weeks. Salamander and lizard neurospheres were cultured in vitro, DiI labeled, and injected into the spinal cord of an amputated salamander or lizard tail. **(A-C)** Transverse sections of salamander **(A,B)** or lizard **(C)** regenerated ependymal tubes stained for Shh and Pax7. Salamander NSCs co-expressed DiI and Pax7/Shh when injected into salamander tails but only Shh in lizard tails. Lizard NSCs did not co-localize expression of DiI and Pax7. All regenerates are 4 weeks post-amputation/NSC injection. Scale bar = 50 μm.

Table 3. Antibody Information

Antibody Name	Company	Catalog No.
Collagen Type II (Col2)	Abcam	ab34712
βIII-Tubulin	Abcam	ab78078
Pax7	Developmental Studies Hybridoma Bank	PAX7-c
Shh	Novus Biologicals	NBP1-69270
BMP-2	Abcam	ab14933
Pax6	Developmental Studies Hybridoma Bank	PAX6-s
FoxA2	Developmental Studies Hybridoma Bank	4C7
Sox2	Abcam	ab97959
GFAP	Abcam	ab4674
Myosin Heavy Chain	Developmental Studies Hybridoma Bank	MF 20-c

Table 4. qRT-PCR primer sequences for the mourning gecko (*Lepidodactylus lugubris*)

Gene	Forward Primer	Reverse Primer
GAPDH	CCATGTTTGTGATGGGTGTC	CTTCTGTGTGGCTGTGATGG
Shh	TACGTCATCGAGACCCGGAG	CAGAAGGGCGTGGGCTACTC
Pax7	CTCCCGCAAACCACATGAA	CCTGTTTCCACGGGTAGGAG
Sox2	CATGATGGAGAGCGAGCTGAA	GGCAGGGTGTACTTATCCTTCT
Sox10	CCATGTTGGAGGCTATGCC	TAGTGGGGCAGACTGAGTGA
NEFH	CCGAGGAATGGTTCCGAGTG	GGCCATTTTGACGTTGAGCA
GFAP	GGAGCGGAAAATCGAATCCCT	TCGGTCTCGTGCATGTTGTT

APPENDIX C

CHONDROGENESIS OF HUMAN BONE MARROW MESENCHYMAL STEM CELLS IN 3-DIMENSIONAL, PHOTOCROSSLINKED HYDROGEL CONSTRUCTS: EFFECT OF CELL SEEDING DENSITY AND MATERIAL STIFFNESS

Abstract

Three-dimensional hydrogel constructs incorporated with live stem cells that support chondrogenic differentiation and maintenance offer a promising regenerative route towards addressing the limited self-repair capabilities of articular cartilage. In particular, hydrogel scaffolds that augment chondrogenesis and recapitulate the native physical properties of cartilage, such as compressive strength, can potentially be applied in point-of-care procedures. We report here the synthesis of two new materials, [poly-L-lactic acid/polyethylene glycol/poly-L-lactic acid] (PLLA-PEG 1000) and [poly-D,L-lactic acid/polyethylene glycol/poly-D,L-lactic acid] (PDLLA-PEG 1000), that are biodegradable, biocompatible (>80% viability post fabrication), and possess high, physiologically relevant mechanical strength (~1,500 to 1,800 kPa). This study examined the effects of physiologically relevant cell densities (4, 8, 20, and 50 x 106/mL) and hydrogel stiffnesses (~150kPa to ~1,500 kPa Young's moduli) on chondrogenesis of human bone marrow stem cells incorporated in hydrogel constructs fabricated with these

materials and a previously characterized PDLLA-PEG 4000. Results showed that 20 x 106 cells/mL, under a static culture condition, was the most efficient cell seeding density for extracellular matrix (ECM) production on the basis of hydroxyproline and glycosaminoglycan content. Interestingly, material stiffness did not significantly affect chondrogenesis, but rather material concentration was correlated to chondrogenesis with increasing levels at lower concentrations based on ECM production, chondrogenic gene expression, and histological analysis. These findings establish optimal cell densities for chondrogenesis within three-dimensional cell-incorporated hydrogels, inform hydrogel material development for cartilage tissue engineering, and demonstrate the efficacy and potential utility of PDLLA-PEG 1000 for point-of-care treatment of cartilage defects.

Introduction

Cartilage tissue possesses limited potential for self-repair, and damage resulting from various disease processes, aging, or trauma ultimately leads to the formation of a persistent cartilage defect and the onset of osteoarthritis (OA).[221] OA is a degenerative joint disease that affects approximately 27 million people in the U.S. each year and it places a heavy burden on society at a cost of approximately $89.1 billion yearly.[222,223] Although the pathogenesis of OA is not fully understood, age and body habitus contribute heavily to the development of OA, and with an ever-aging population suffering from increasing rates of obesity, methods towards addressing and alleviating the burden of this debilitating disease are a necessity.

Traditional treatment options aimed at resolving the osteochondral defect in OA have provided limited success with each bearing their own inadequacies.[224] The use of an osteochondral allograft provides native tissue that can be used to fill the defect, but it has the potential for immune rejection, disease transmission, and infection. Microfracture stimulates endogenous repair by a small fracture injury to the bone, but it can result in the formation of mechanically inferior fibrocartilage instead of native hyaline cartilage, thereby requiring a second intervention. Total joint arthroplasty, which is usually reserved for severe cases of OA, increases mobility but eliminates the potential for biological joint repair and requires a major surgery, which may not be an option for many patients.[225,226] In addition, this repair has limited lifespan in young patients, thus necessitating multiple surgeries over a lifetime. Given the respective limitations of these techniques, new approaches towards treating OA are actively being pursued.

Recently, regenerative medicine strategies using autologous cells, biomaterial scaffolds, and growth factors have garnered significant interest as potential routes to repair the

osteochondral defect.[221,227] One set of techniques, autologous chondrocyte implantation (ACI) and matrix-induced ACI (MACI), involve harvesting healthy chondrocytes from non-weight bearing regions of articular cartilage and expanding the chondrocytes *in vitro* for re-implantation with or without cell seeding onto a biomaterial extracellular matrix (ECM).[228,229] While such techniques utilizing mature adult cells offer a viable regenerative approach, they are constrained by lengthy cell expansion times, the potential for de-differentiation of chondrocytes during the expansion period, and contamination.[230] Another promising avenue towards obtaining mature chondrocytes involves the use of adult mesenchymal stem cells (MSCs), which have the ability to differentiate into a variety of lineages, including chondrocytes.[231] Bone marrow derived stem cells (BMSCs) in particular are of great interest for they are one of the most extensively studied MSCs, and intra-articular injections of BMSCs have been reported to reduce osteoarthritic pain, improve joint mobility, and slow progressive osteoarthritic degeneration.[232–234] As such, regeneration in OA employing BMSCs is an attractive alternative to currently applied ACI procedures.

The ideal scaffold should mimic the mechanical properties of cartilage, degrade as cells secrete their own extracellular matrix (ECM), and provide an environment conducive to cell survival and maintenance of a chondrocyte lineage. Many biomaterials have been developed that allow for live cell incorporation, but none adequately fulfill all the requirements of an ideal scaffold.[235–237] Recently, we reported the use of a water soluble methacrylated polyethyleneglycol-poly-D,L-lactide (mPDLLA-PEG) biodegradable polymer for live cell scaffold fabrication that possessed high mechanical strength (~780 kPa).[238] While this scaffold possessed physiologically relevant mechanical strength on fabrication, we found that after 4 weeks the strength of the cell-seeded scaffold had degraded drastically (~240 kPa). This finding

implies that ECM deposition by the encapsulated cells failed to provide sufficient mechanical reinforcement to the scaffold. Augmenting this ability is thus necessary, for example by varying factors such as cell density and material properties, both of which may affect ECM production, deposition, and organization. Indeed, for cells incorporated in hyaluronic acid and alginate 3D scaffolds increasing levels of matrix organization and deposition were seen with increasing concentrations of initial cell seeding density up to approximately 20×10^6 cells/mL.[239–242] On the other hand, an important material property, stiffness, is also known to play a part in determining stem cell differentiation into different lineages on both 2D and 3D substrates.[243–249] For 2D surface-seeded chondrocytes, mechanically matching scaffolds allowed for retention of rounded chondrocyte morphology and higher ECM production than counterparts with lower stiffnesses.[250] However, this is contrasted by BMSC behavior in 3D hyaluronic acid hydrogels where higher crosslinking densities and moduli led to a decrease in ECM production.[251,252] Given these observations, optimization of cell concentration and material stiffness is likely to be critical for enhanced chondrogenesis in live cell incorporated scaffolds that possess physiologically relevant mechanical properties.

In this study, we report the development of two new biomaterials, PDLLA-PEG 1000 and PLLA-PEG 1000, which are low molecular weight versions of our previously reported material, PDLLA-PEG 4000 (the terminal number indicates the molecular weight of the PEG chain) for use in live cell 3D incorporation. These new polymers exhibit properties of biodegradability and biocompatibility similar to those of the previous PDLLA-PEG 4000, but they possess mechanical properties that are much higher due to increased crosslinking density. Using these 3D materials, for the first time we probe the cellular efficiency of ECM production with varying cell densities and the effects of modulating material stiffness on chondrogenesis on a physiologically

relevant scale (~150 kPa to 1500 kPa Young's modulus) in static cultured human BMSC (hBMSC) incorporated hydrogels. Our results should inform cell seeding protocols and the development of mechanically appropriate scaffolds for point-of-care articular cartilage tissue engineering.

Material and Methods

All chemicals were purchased from Sigma Aldrich (St. Louis, MO, USA) unless otherwise specified.

Human Bone Marrow Stem Cell Isolation. hBMSCs were isolated from the femoral heads of patients undergoing total joint arthroplasty with IRB approval (University of Washington and University of Pittsburgh), and cultured and expanded as previously described.[253] Briefly, bone marrow was flushed out from the trabecular bone of the femoral neck and head using an 18-gauge needle and re-suspended in Dulbecco's Minimal Essential Medium (DMEM). The suspension was filtered through a 40 μm strainer and the flow-through was centrifuged at 300*g* for 5 min. After the supernatant was discarded, the cell pellets were re-suspended using growth medium (GM, α-MEM containing 10% fetal bovine serum (FBS, Invitrogen), 1X antibiotics-antimycotic (Ampicillin 100 units/mL, Streptomycin 100 μg/mL, Amphotericin B 250 ng/mL), and 1.5 ng/mL FGF-2 (RayBiotech, Norcross, GA)), and then plated into 150 cm^2 tissue culture flasks at a density of 20,000-40,000 nucleated cells/cm^2, and medium was changed every 3 to 4 days. Once 70% to 80% confluence was reached, cells were passaged. All experiments were performed with passage 4 (P4) hBMSCs except the cell concentration experiments, which were performed with passage 3 (P3) hBMSCs. All cells used in this study were pooled from three patients: 58 y/o female, 62 y/o female, and 69 y/o male.

Synthesis of Methacrylated PDLLA-PEG 4000, PDLLA-PEG 1000, and PLLA-PEG 1000. Preparation of mPDLLA-PEG 4000 was performed as described by Seck et al.[254] Briefly, 50 g of PEG (4 kDa molecular weight) was placed into a 250 mL beaker and subjected to 600 W microwave irradiation for 3 min. Subsequently, 3.5 g (2.80 mL) of stannous octoate [$Sn(Oct)_2$] was added to the molten PEG followed by addition of 7.2 g D,L-lactide. The mixture was briefly

swirled to mix the contents and then subjected to 600 W microwave irradiation for 1 min. The initial PDLLA-PEG 4000 polymer was precipitated in 500 mL cold isopropanol and dried under vacuum for 2 days. The dry polymer was placed into a dry 500 mL round bottom flask and dissolved in 100 mL dichloromethane (DCM) followed by addition of three equivalents of trimethylamine (TEA, ~5.25 mL) and three equivalents of methacrylic anhydride (MA, ~5.60 mL). The reaction mixture was placed under Argon gas and allowed to stir at room temperature for 7 days. After completion of the reaction, the mixture was precipitated into diethyl ether. For further purification, the macromere was re-dissolved in minimal amounts of chloroform and re-precipitated in diethyl either.

Preparation of mPDLLA-PEG 1000 and mPLLA-PEG 1000 was carried out similarly as above, except PEG with 1 kDa molecular weight was used in the synthesis and L-lactide was used in place of D,L-lactide for the latter synthesis. In addition, the two precipitation steps (isopropanol and diethyl ether) included 1 hour of cooling at -20 °C after initial precipitation to allow for the product to completely precipitate out.

Synthesis of Photoinitiator LAP. The visible-light sensitive initiator lithium phenyl-2,4,6-trimethylbenzoylphosphinate (LAP) was synthesized as described by Fairbanks et al.[255]

Fabrication of Live Cell Incorporated Constructs. Solutions of polymer and LAP were prepared in 50 mL tubes with 0.3% w/v photoinitiator and either 30%, 25%, or 20% w/v polymer. These concentrations were chosen to yield a range of Young's moduli from ~150 kPa to ~1500 kPa. For instance, the preparation of mPDLLA-PEG 1000 (30% w/v) and LAP (0.3% w/v) was carried out as follows: 12g mPDLLA-PEG 1000 was placed in a 50 mL tube followed by addition of Hanks Balanced Salt Solution (HBSS) close to the 40 mL mark. The solution was

subsequently titrated to pH 7.4 with 10 N NaOH and adjusted to 40 mL using HBSS followed by addition of 120 mg LAP (0.3% w/v).

hBMSCs were pelleted by centrifugation, and the supernatant was completely removed. The appropriate amount of polymer solution was added on top of the pellets and mixed with cells thoroughly by pipetting up and down 20 times for a final concentration of either 4×10^6, 8×10^6, 20×10^6, or 50×10^6 cells/mL. After the bubbles were removed by aspiration, the cell-polymer solution was pipetted to fill multiple circular 5 mm diameter × 2 mm height molds punched out of silicone rubber. Subsequently, a glass coverslip was placed over the molds to ensure flat cylindrical structures. Following this, a visible light source supplying wavelengths of 395 nm (7202UV395, LEDWholesalers) was used to cure the polymers for 2 minutes.

The completed constructs were cultured in chondrogenic medium [DMEM with 1% L-alanyl- L-glutamine (GlutaMAX), 55 μM sodium pyruvate, 1X antibiotic-antimycotic, 1% insulin-transferrin-selenium (ITS)(Invitrogen, Carlsbad, CA, USA), 10 ng/mL transforming growth factor-β3 (TGF-β3; PeproTech, Rocky Hill, NJ, USA), 100 nM dexamethasone, 50 μM L-ascorbic acid 2-phosphate, and 23 μM L-proline]] for up to 8 weeks.

Degradation Test and Mechanical Testing. The extent of degradation of polymers is determined indirectly, by measuring the mechanical property of scaffolds.[20] Cell-free scaffolds fabricated as described above were immersed in 4 mL HBSS supplemented with 1X antibiotic-antimycotic and maintained in a cell culture incubator at 37 °C. HBSS was changed every 3 days.

Mechanical testing of scaffolds was conducted with a mechanical tester (Bose Electroforce model 3230 Series II). Briefly, the cylindrical scaffolds were placed between the compressive motor and the load cell and subjected to 10% compression (0.2 mm) at 0.01 mm/s.

The stress-strain curve was then plotted, and the linear area was used to calculate the compressive modulus of the scaffolds.

Live/Dead Staining. At days 1 and 7 post fabrication, cell viability was assessed with the Live/Dead viability/cytotoxicity kit (Invitrogen) as examined by epifluorescence microscopy following the product manual. The percentage of live cells was calculated by counting the number of live green cells divided by the total (green and red cells together) in cross-sections that spanned both the center and border of the constructs. Clusters of cells were counted to the best visual discrimination of single cells. Images were captured with an inverted microscope (Olympus CKX41, Japan) equipped with a Leica DFC 4300 camera.

Sulfated Glycosaminoglycan (sGAG) and Hydroxyproline Quantification. Cartilage ECM deposition was quantified by measuring sGAG and total collagen production. Constructs were homogenized and then digested for 18 h in 700 µl/construct of a papain solution (125 µg/ml papain, 50 mM sodium phosphate buffer, 2 mM N-acetyl cysteine (Sigma), pH 6.5). An aliquot of the digest was assayed for sGAG content using the Blyscan kit (Accurate Chemical & Scientific Corp, Westbury, NY) according to the manufacturer's instruction. Another aliquot of the digest was assayed for DNA content using the QuantiT PicoGreen dsDNA Assay Kit (Invitrogen).

A third aliquot was used to quantify collagen deposition by measuring hydroxyproline levels using a modified hydroxyproline assay with bovine collagen type I as a standard. Briefly, 200 µl of each sample and standard were hydrolyzed with 200 µl of 4 N sodium hydroxide (Fisher) at 121 °C for 20 min. 200 µl of 4N HCl (Fisher) was added and the solution was titrated to a neutral pH. 1.2 mL of chloramine-T solution (Sigma) (14.1 g/L chloramine-T, 50 g/L citric acid, g/L sodium acetate trihydrate, 34 g/L NaOH, 0.21 M acetic acid) was incubated at room

temperature for 20 min. Then, 1.2 mL of 15 g/L p-dimethylaminobenzaldehyde in 2:1 isopropanol:perchloric acid was added and the solution was placed in a 60 °C water bath for 20 min. Finally, 200 µl of each sample in triplicate was added into a 96 well plate and absorbance was read at 550 nm.

Analysis of Gene Expression by Real Time Reverse Transcription PCR (RT-PCR). Total RNA of the cells within constructs was isolated by homogenizing in TRIZOL reagent (Invitrogen) and purified using RNeasy Plus Mini Kit (Qiagen, Germantown, MD, USA). Reverse transcription was achieved using SuperScript® VILO™ cDNA Synthesis Kit (Invitrogen) according to the manufacturer's protocol. Real-time PCR was performed using the SYBR Green Reaction Mix (Applied Biosystems, Foster City, CA, USA) with a StepOne-Plus thermocycler (Applied Biosystems). Gene expression levels of Sox 9, collagen types II and X, aggrecan and matrix metalloproteinase 13 (MMP13) were analyzed. All sample values were normalized to ribosomal protein L13a (RPL13A) using the $2^{-\Delta\Delta Ct}$ method.

Histology. Whole constructs were fixed in 10% neutral buffered formalin (Fisher Scientific, Pittsburgh, PA) for 1 day, dehydrated, paraffin-embedded, and 10 µm sections were prepared. Staining with Safranin O/Fast Green and Alcian Blue/Fast Red was used to detect sGAG and proteoglycan deposition.

Transferrin Perfusion. Cell-seeded constructs composed of 30% PDLLA-PEG 4000 were fabricated as described above. These were cultured in chondrogenic medium containing Transferrin-546 nm (Invitrogen) at 60 µg/ml for 14 days. Constructs were then fixed in 4% paraformaldehyde overnight at 4°C, equilibrated in sucrose, and embedded in optimal cutting temperature (OCT) compound. These were then sectioned at 50 µm.

Statistical Analysis. All data were expressed as mean ± standard deviation and statistical analysis was performed using either two-way independent analysis of variance (ANOVA) or two-way independent multivariate analysis of variance (MANOVA) followed by Tukey's HSD post hoc testing. A threshold of $p < 0.05$ was used to determine statistical significance.

Results

Mechanical testing and degradation analysis. Figure 1 shows the mechanical properties of PDLLA-PEG 4000, PDLLA-PEG 1000, and PLLA-PEG 1000 over 28 days in HBSS. Due to the presence of ester bonds between lactide molecules and PEG, the polymers are expected to degrade through hydrolytic cleavage (Seck et al, 2010). The compressive moduli of the scaffolds decreased steadily over time, with a $p<0.001$ between each time point within each group, except for between days 21 and 28 where the rate of change slowed. Statistically significant differences were also found in group and concentration effects with regard to mechanical strength ($p<0.001$). The new materials, PDLLA-PEG 1000 and PLLA-PEG 1000, were significantly stronger than PDLLA-PEG 4000, as evidenced by a 3- to 4- fold higher compressive modulus at all time points. In addition, the low molecular weight scaffolds did not swell in HBSS, likely contributing to their strength.

Cell viability assessment in new materials. For the new materials, PDLLA-PEG 1000 and PLLA-PEG 1000, cell viability remained high between the post-fabrication period and day 7 with cell viability >85% in all groups at day 7 (Figure 53). The viability did not change significantly between the different concentrations of polymer, indicating that at 20×10^6 cells/mL adequate nutrient diffusion was achieved at all concentrations and that the materials were biocompatible.

Determining optimal cell density. Cells seeded in 30% PDLLA-PEG 4000 at varying concentrations all exhibited a significant difference in compressive moduli between 4 and 8 weeks after fabrication (Figure 54**A**, $p<0.05$), but mechanical strength was neither increased nor maintained within any group. Examination of DNA levels showed significant differences between all groups except the 20×10^6 cells/mL and 50×10^6 cells/mL groups ($p=0.178$) (Figure

54**B**). Total sGAG and hydroxyproline deposition was significantly higher in the 20 × 10^6 cells/mL group when compared to 4 and 8 × 10^6 cells/mL ($p<0.001$), but was not significantly different from 50 × 10^6 cells/mL (Figure 54**C,E**). However, when normalized to number of cells originally seeded in the constructs, the 20 × 10^6 cells/mL group had significantly higher sGAG deposition than all other groups ($p<0.001$) (Figure 54**D,F**). Safranin O and Alcian Blue staining demonstrate strong GAG deposition by both 20 and 50 × 10^6 cells/mL groups, with the former showing uniform staining and the latter showing weaker central staining (Figure 55**A-D**). To evaluate whether the non-uniform pattern of chondrogenesis could be related to accessibility to TGF-β3, fluorescently labeled transferrin (ITS - yellow) was added to the culture medium as a tracer of similar molecular size to TGF-β3 to assess its diffusion through the scaffold at different cell densities. Fluorescence microscopy revealed that at higher cell density, ITS staining was limited to the periphery of the scaffold (Figure 55**F),** while at lower cell density the ITS uptake was more uniform (Figure 55**E**). Sections were taken at approximately the center of each scaffold.

Effect of material stiffness on chondrogenesis. Compressive moduli of PDLLA and PLLA-PEG 1000 were significantly higher at all concentrations and time points than corresponding PDLLA-PEG 4000 ($p<0.001$) (Figure 56**A**). However, compressive moduli were not maintained over the 28-day culture period. DNA content was significantly higher in the PDLLA-PEG 4000 groups across the 3 concentrations than in the other low molecular weight groups ($p<0.001$), most likely due to the swelling of the scaffold which provided for more space for cell proliferation (Figure 56**B**). Due in part to this higher cell number, the group effects for total levels of sGAG and hydroxyproline were significantly higher for PDLLA-PEG 4000 versus PDLLA and PLLA-PEG 1000 ($p<0.005$) (Figure 56**C,E**). However, when calculated based on

DNA content there was no significant difference in the group effects of sGAG/DNA and hydroxyproline/DNA for PDLLA-PEG 4000 versus PDLLA-PEG 1000 ($p>0.5$ for both)(Figure 56**D,F**). In all measures of ECM production, PLLA-PEG 1000 was significantly lower than either of the other two groups ($p<0.001$)(Figure 56**C-F**). In addition, there was a significant polymer concentration effect for sGAG/DNA and sGAG/construct, with $p<0.05$ for 20% versus 25%, 25% versus 30%, and 20% versus 30%. The only exception to this was in sGAG/DNA, with $p=0.06$ for 25% versus 30%. (Figure 56**C, D**).

The influence of polymer concentrations on chondrogenic gene expression across the different groups is shown in Figure 57. Overall, there was a significant polymer concentration effect for PLLA-PEG 1000 for all combinations of concentrations in all genes tested ($p<0.05$). The exceptions to this in the PLLA-PEG 1000 group were for collagen type X (20% versus 25%, $p=0.286$) and MMP13 (25% versus 30%, $p > 0.5$). Conversely, PDLLA-PEG 1000 exhibited significant differences only between 25% and 30% and PDLLA-PEG 4000 in general contained no significant differences between groups. The one exception in the PDLLA-PEG 4000 group was for 20% versus 30% in collagen type II ($p=0.045$). Lastly, multivariate analysis of PDLLA-PEG 4000 versus PDLLA-PEG 1000 to determine differences in chondrogenic potential revealed no significant differences across all genes except MMP13, which had a $p=0.027$.

Histological analysis of ECM production using Alcian Blue/fast red staining is shown in Figure 58. Strong sGAG deposition is seen across all polymer concentrations in the PDLLA-PEG 4000 group with decreasing staining as concentration of material was increased (Figure 58**A-C**). PDLLA-PEG 1000 group exhibited a similar trend of strong staining, which decreased with increasing polymer concentration (Figure 58**D-F**). In contrast, cells exhibit weak staining

across all three polymer concentrations in the PLLA-PEG 1000 group (Figure 58**G-I**). The histological findings thus correlated well with the gene expression data, with PLLA-PEG 1000 scaffolds showing significant differences in gene expression levels of chondrogenic markers when compared to PDLLA-PEG 1000.

Discussion

The goal of this study was to identify and characterize a candidate biomaterial scaffold that is able to support chondrogenic differentiation of seeded hBMSCs, and possesses a biodegradability profile sufficient to mimic the mechanical properties of the native cartilage tissue. As a control, the previously characterized material, PDLLA-PEG 4000, was used. We identified PDLLA-PEG 1000 as a material that possesses mechanical properties in the range of native articular cartilage, and demonstrated both high cell viability and chondrogenic potential of seeded hBMSCs within the material construct. We found that the optimal cell seeding density for ECM deposition in this material was 20×10^6 cells/mL due to limited nutrient diffusion above those concentrations, and interestingly, we also observed that hBMSC chondrogenesis within this material was dependent on material concentration, not material stiffness. These findings point to the potential utility of this material in point-of-care articular cartilage repair and inform future material development.

A point-of-care engineered cartilage construct ideally possesses mechanical properties similar to native cartilage at the time of fabrication.[221] Towards this end, the new low molecular weight polymers possessed much higher moduli than PDLLA-PEG 4000, presumably due to the increased number of crosslinking chains. Indeed, this increase in toughness of methacrylate networks corresponding to higher crosslinking density has been previously described.[256] Interestingly, PLLA-PEG 1000 displayed higher moduli than PDLLA-PEG 1000 at the same concentrations despite having a similar chemical composition (as shown in Figure 52), but we hypothesize that this can be explained by lower levels of hydrolysis, which is a known degradation mode for these networks,[257] in the former during the pH neutralization step of the material preparation. Degradability has been shown to be an important component of successful

remodeling,[258–260] and these new materials possessed similar degradation rates to PDLLA-PEG 4000 likely due to all materials having the same ratio of hydrolyzable lactide to PEG moieties.

With materials covering a wide range of mechanical stiffnesses, the optimal constructs for chondrogenesis in static culture were assessed by examining the effect of cell concentrations on ECM production and mechanical properties. Our results showed that 20×10^6 cells/mL loading density allowed for the most efficient production of ECM per cell (Figure 54). Interestingly, this concentration is similar to those reported to be optimal in softer hydrogels such as hyaluronic acid[239,240,242]. We also observe that the DNA content of 20 and 50×10^6 cells/mL groups are the similar at 4 and 8 weeks, which we hypothesize is due to cell death in the latter. A combination of two factors is potentially at play: saturation of cells per unit volume in the confined space of the construct, and limitation in cell support by nutrient diffusion through the scaffold in static culture. Nutrient diffusion has been implicated as a limiting factor for ECM production, as Mauck et al. demonstrated that increased nutrient diffusion through mechanical stimulation allowed for higher levels of ECM deposition at high cell densities.[25,26] Indeed, at 50×10^6 cells/mL, the periphery of the scaffold showed strong matrix GAG staining with both Alcian blue and Safranin O compared to the center in contrast to the uniform staining seen in the 20×10^6 cells/mL group. This region-dependent characteristic of MSC chondrogenesis has been demonstrated by Farrell et al. and is in accordance with our findings.[261] Results in Figure 55**E and** Figure 55**F** suggest that this phenomenon may be due to the lower cell density allowing for higher diffusion of transferrin, a molecule of similar size to TGFβ3, through the entire scaffold. It is noteworthy that all hydrogel constructs were cultured sitting undisturbed on flat surfaces (the bottom of a six-well tissue culture plate) with the minimum amount of medium needed to

cover the top surface, thus little to no diffusion occurred from the top/bottom and most diffusion occurred along the lateral edge of the constructs.

Another factor known to influence stem cell behavior is matrix stiffness, with stiffer matrices promoting osteogenesis and softer ones driving cell fate toward adipogenesis.[243–249] However, how stiffness affects MSC chondrogenesis in degradable 3D networks within the physiological range of cartilage stiffness has not been reported. With the optimal cell concentration for static culture established, we next studied the influence of scaffold mechanical property on ECM production (Figure 56) and gene expression (Figure 57) at a cell concentration of 20×10^6 cells/mL. Strikingly, on the basis of ECM deposition, we found that mechanical stiffness is unlikely to be the driving factor between the differences in ECM production, but rather it is the concentration of the polymer used to create the hydrogel that seems to dictate the biological response. Specifically, the free space (as a function of concentration) available in the scaffold seems to drive the ability of the cells to produce ECM. This can be clearly seen in the case of gene expression in PLLA-PEG 1000 (Figure 57), where the expression levels of ECM related genes (Sox9, Col II, Aggrecan, Col X) are increasingly downregulated as concentration increases, whereas matrix catabolic gene MMP13 is upregulated with increasing concentration. We also observe that at 4 weeks, cell viability is still maintained in both PDLLA-PEG 1000 and PLLA-PEG 1000 (Figure 59). We hypothesize that the material PLLA-PEG 1000 performs poorly in both ECM production and gene expression because of limited diffusion due to the L configuration of the lactide molecules which does not allow water to move through and penetrate the scaffold as readily as in the PDLLA scaffolds, which is reflected in its slower degradation than PDLLA.[262] This property would potentially lead to decreased nutrient diffusion and a smaller “space” sensed by cells, thus magnifying the polymer concentration effect on matrix

production. While Bryant et al. previously noted that in non-degradable and partially degrading PEG networks ECM production did not vary within a range of about 1 MPa and 10-30% w/w concentration[259], our hydrogels are fully degradable and thus lend a different microenvironment. Our observations also contrast with the study by Bian et al., which demonstrated that higher crosslinking densities decreased cartilage ECM production.[251] This discrepancy, however, can be reconciled by their observation that higher crosslinking density actually resulted in higher concentrations of hyaluronic acid retained in the material. Thus, by viewing these findings in terms of decreased cell space rather than increased crosslinking density, they are consistent with our observations and conclusions.

While ECM production is one measure of efficacy, one of the main limitations of our study is that none of the scaffolds were able to achieve our end goal of constructs that can retain mechanical strength over time. On examination of histological sections **(**Figure 58**)**, we see that even in the groups with adequate nutrient diffusion, the deposited ECM is localized only around cell clusters and not distributed within the PEG material (holes seen in the material are due to sample processing). This localized distribution of ECM has been observed in other studies utilizing PEG-based materials as well[258,259], and is a likely cause to the inability of the deposited ECM to reinforce the scaffold. Indeed, studies utilizing high cell concentrations allowing for cell contact, materials that result in distributed ECM deposition within the scaffold, or cell pellets all have demonstrated the ability to increase mechanical strength over time – albeit starting from a low mechanical strength[240,263–266]. In addition to lack of mechanical property retention, another limitation lies in the appearance of hypertrophic cells, a well-known shortcoming of MSC chondrogenesis in 3D scaffolds. Based on expression levels of hypertrophy related genes MMP13 and ColX (Figure 57) the new material PDLLA-PEG 1000 is not able to reduce

hypertrophic response, an inevitable consequence of exposure to TGF-β3 containing chondroinductive medium.[267,268] However, it does offer the advantage of increased mechanical strength without a decrease in ECM production.

Overall, we have established here an optimal cell seeding density and introduced a new material, PDLLA-PEG 1000, that is similarly pro-chondrogenic for encapsulated BMSCs as the PDLLA-PEG 4000 we previously reported, and we have demonstrated that within the 150 kPa – 1500 kPa range, material concentration plays an important role in determining cellular response rather than material stiffness or crosslinking density. This new material also exhibits substantially improved mechanical strengths approximately 4 times higher than its high molecular weight counterpart after 4 weeks of culture. However, the mechanical strength of the PDLLA-PEG 1000 scaffold is still not adequately augmented by new ECM produced by the seeded cells. Given the absence of cell-binding sites on PDLLA-PEG, it is possible that the supplementation of molecules that can interact with cells, such as hyaluronic acid, can aid in ECM deposition and crosslinking.[269–271] Another challenge is the limited nutrient diffusion into the biomaterial scaffold. Mauck et al. previously showed that mechanical loading increases nutrient diffusion through hydrogels and improves mechanical properties of agarose scaffolds after 4 weeks of cyclic loading, and allows for cell densities higher than 20×10^6 cells/mL to be optimal.[272,273] A similar mechanical regimen may be tested here. Lastly, increasing the PDLLA to PEG ratio in our polymers may allow for increased cell contact and ECM crosslinking due to increased “space” due to higher rates of degradation. These concepts will be tested to achieve a cell incorporated construct that can retain mechanical properties for cartilage tissue engineering.

Conclusion

In this study, we have determined that BMSC seeding at 20×10^6 cells/mL allows for optimal efficiency of ECM production per cell for cell incorporated PDLLA-PEG hydrogels in static culture. We also conclude that within the physiological range of cartilage mechanical properties in PDLLA-PEG hydrogels, material concentration but not material stiffness influences cell ability to secrete ECM with increasing hydrogel concentrations limiting matrix deposition. This characteristic implies that degradable PEG hydrogels that possess high stiffness at low polymer concentrations are better able to maximize cell free space concurrently with mechanical strengths and would be optimal for cartilage tissue engineering. Lastly, we have introduced a new material, PDLLA-PEG 1000, that possesses mechanical strength in the physiologic range of native cartilage and strong chondrogenic potential. Our current work aims to optimize and develop this material for the repair of cartilage defects in future studies.

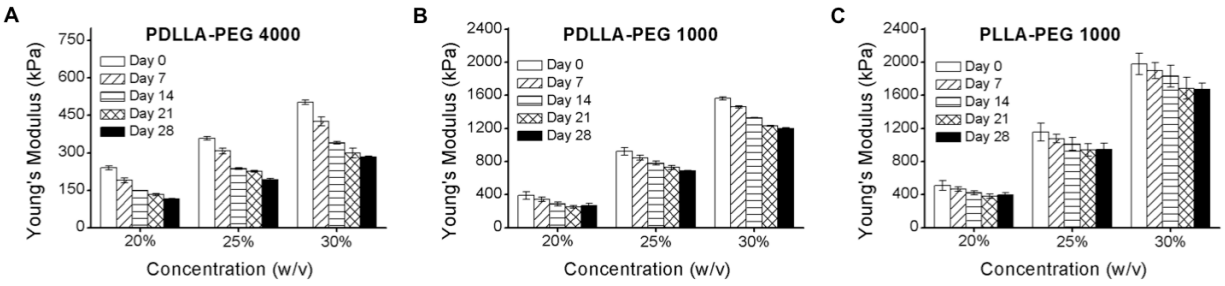

Figure 52. Mechanical properties and degradation of polymers as a function of polymer concentrations and incubation time. (A) PDLLA-PEG 4000; (B) PDLLA-PEG 1000; and (C) PLLA-PEG 1000. Statistically significant reductions in compressive moduli are seen at each increasing time point ($p<0.001$) and each concentration for all materials, except between days 21 and 28 where $p > 0.5$. In addition, the main effects of material type and material concentration are significantly different for these biomaterials ($p<0.001$ based on two-way independent ANOVA). $n = 3$ replicates for all groups.

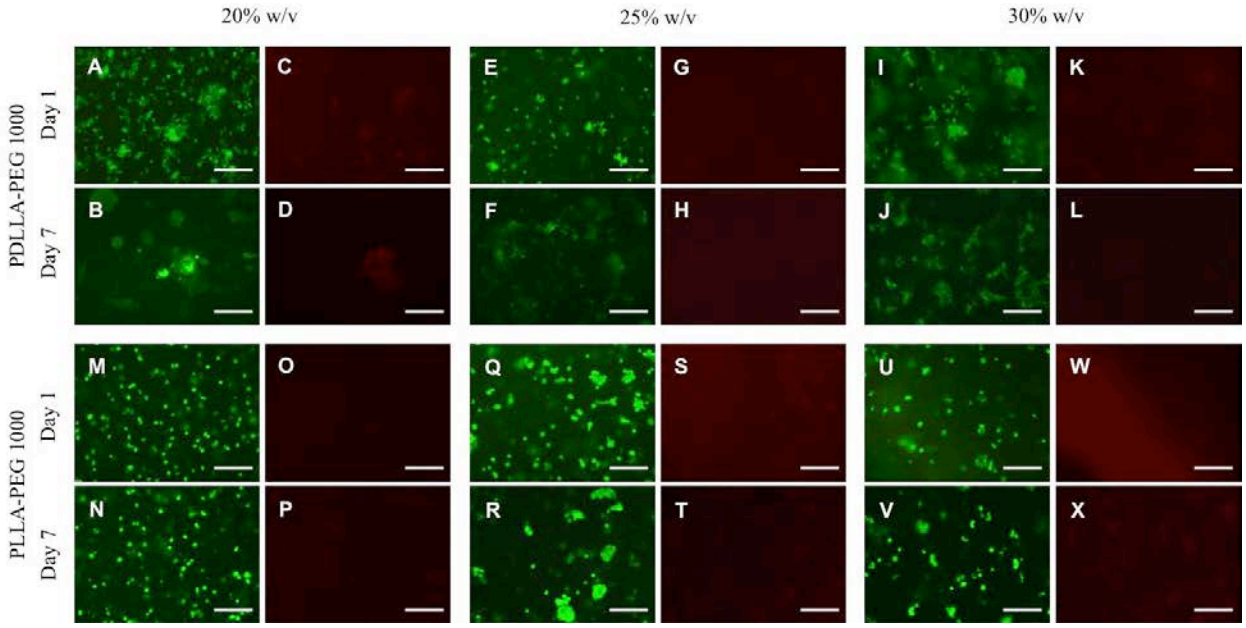

Figure 53. Cell viability in hydrogel constructs. (A,B,E,F,I,J,M,N,Q,R,U,V) Calcein-AM staining (green, live cells) and **(C,D,G,H,K,L,O,P,S,T,W,X)** EthD-1 staining (red, dead cells) in cell-seeded scaffolds following fabrication at days 1 and 7 across 20%, 25%, and 30% w/v polymer concentrations. Cell viability at day 7 was >85% in all groups based on green count/ total count. Scale bar = 150 μm.

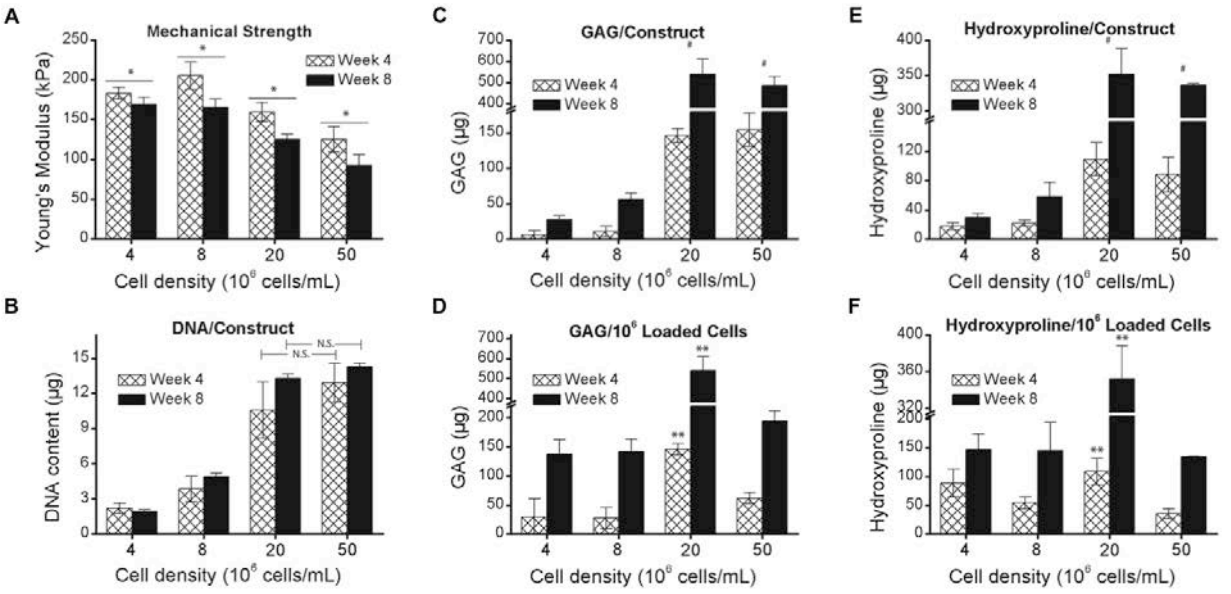

Figure 54. Effect of cell density on ECM synthesis. BMSCs were seeded in 30% PDLLA-PEG 4000 at densities ranging from 4 - 50 x 10^6 cells/mL. **(A)** Mechanical strength of constructs after 4 and 8 weeks of static culture. **(B)** Total cell number estimated from DNA content in constructs **(C,E)** Total ECM deposition measured by **(C)** GAG and **(E)** Hydroxyproline contents per construct. **(D,F)** ECM deposition normalized to initial cell loading number. *, $p<0.05$, between week 4 and week 8. #, $p<0.001$, for 20 and 50 x 10^6 cells/mL groups versus 4 and 8 x 106 cells/mL groups at both timepoints, and no significant difference between 20 and 50 x 10^6 cells/mL. **, $p<0.001$, when compared to all other groups at the same time point. n = 6 replicates per group.

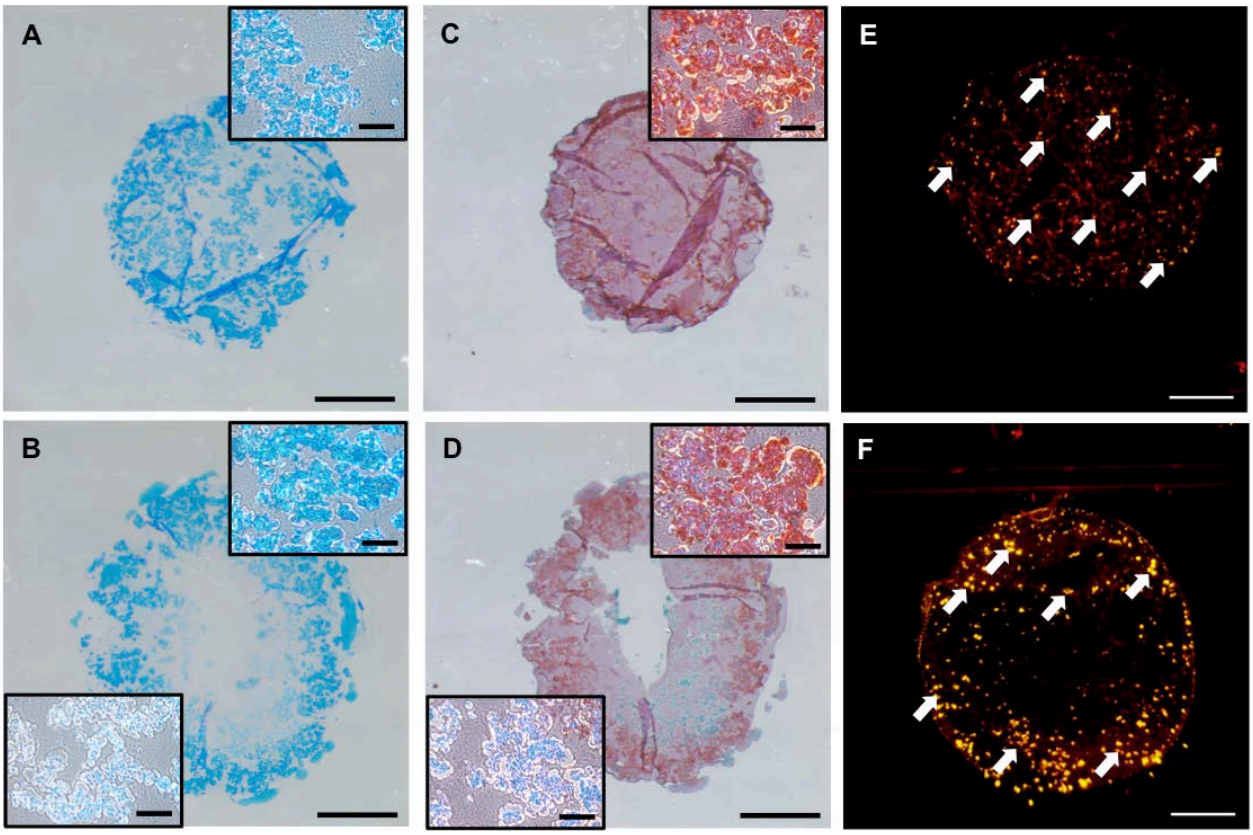

Figure 55. ECM deposition in high cell density constructs at 8 weeks. (A,C) Macroscopic view of **(A)** Alcian Blue/Fast Red staining and **(C)** Safranin O/fast green staining for GAG deposition in 20 × 10^6 cells/mL. Inset is a higher magnification representative region in the construct. **(B,D)** Macroscopic view of **(B)** Alcian Blue/Fast Red and **(D)** Safranin O/Fast Green staining at 50 × 10^6 cells/mL. Top right inset is higher magnification representative region in periphery of construct while bottom left shows higher magnification representative region in more central zone of the construct. **(E,F)** Cellular uptake of fluorescently labeled transferrin at 20 × 10^6 cells/mL and 50 × 10^6 cells/mL after 14 days of static culture, respectively. Scale bars = 1500 μm in macroscopic views, 150 μm in the insets.

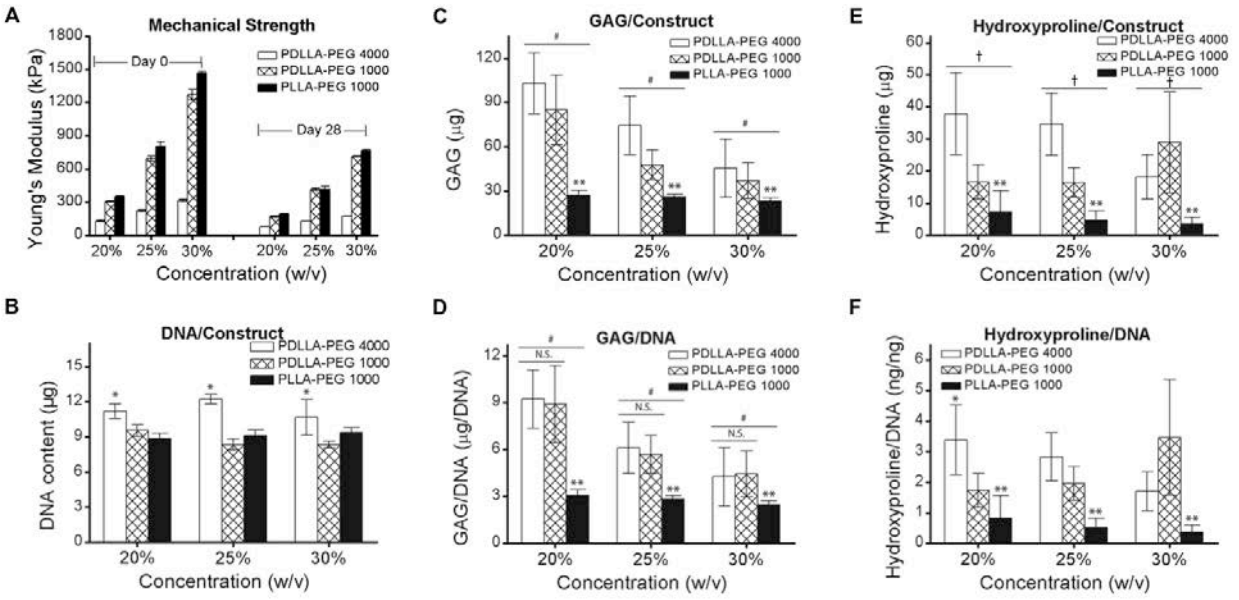

Figure 56. Effect of material concentration and stiffness on ECM deposition. BMSCs were seeded at 20×10^6 cells/mL in scaffolds of different polymer concentrations and material properties. **(A)** Mechanical strength post fabrication and after 4 weeks of culture. Mechanical properties of PDLLA and PLLA-PEG 1000 were significantly higher at all polymer concentrations and timepoints than corresponding PDLLA-PEG 4000 ($p<0.001$). **(B)** Cell number measured on the basis of DNA content in constructs. **(C,E)** Total ECM deposition measured by **(C)** GAG and **(E)** Hydroxyproline production per construct. **(D, F)** ECM deposition normalized to DNA content. *, $p<0.001$, as compared to other materials at same concentration. **, $p<0.001$, for main effect of material as compared to others. #, $p<0.05$, for main effect of material concentration between concentrations and $p<0.005$ for main effect of PDLLA-PEG 4000 versus other groups. †, $p<0.005$, for main effect of PDLLA-PEG 4000 versus other groups. All effects were determined by Tukey's HSD post-hoc testing following two-way independent ANOVA analysis. n = 6 replicates per group.

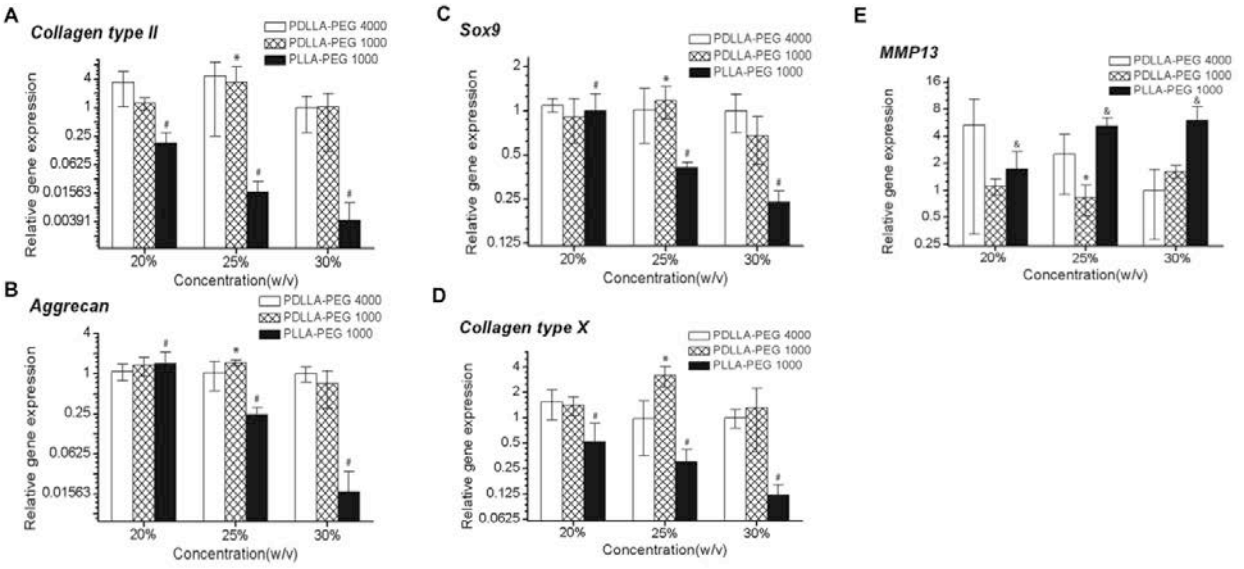

Figure 57. Real-time PCR analysis of gene expression in hBMSC seeded constructs (20×10^6 cells/mL) at day 28. Relative gene expression levels of **(A)** collagen type II, **(B)** Aggrecan, **(C)** Sox9, **(D)** collagen type X, and **(E)** MMP13, normalized to cell gene expression in PDLLA-PEG 4000 at 30% w/v polymer concentration. Overall, two-way independent MANOVA analysis of PDLLA-PEG 4000 versus 1000 revealed no significant differences across all genes except MMP13 ($p=0.027$). *, $p<0.05$, for PDLLA-PEG 1000 25% versus 30%. #, $p< 0.005$, between all concentrations for PLLA-PEG 1000 except collagen type X, where 20% versus 25% showed $p=0.286$. &, $p<0.005$, between 20% versus 25% and 30%. n = 6 replicates per group.

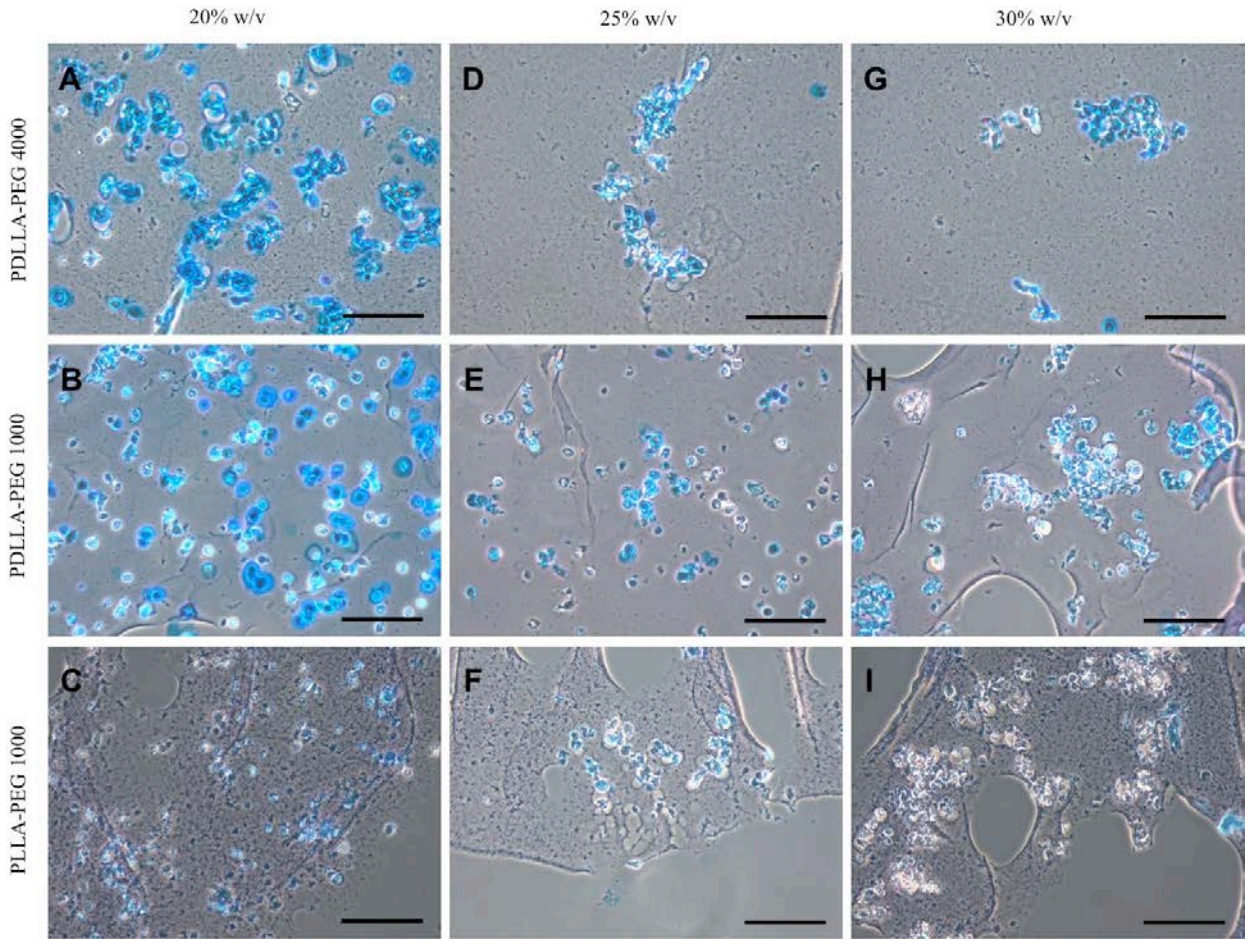

Figure 58. Glycosaminoglycan content in hBMSC-encapsulated constructs (20 × 10^6 cells/mL) visualized by Alcian Blue/Fast Green staining at day 28. (A,D,G) Staining of PDLLA-PEG 4000 group. **(B,E,H)** Staining of PDLLA-PEG 1000 group. **(C,F,I)** Staining of PLLA-PEG 1000. Scale bar = 150 μm. Center of scaffold is towards top left of images, and images were obtained between the center and edge of scaffold.

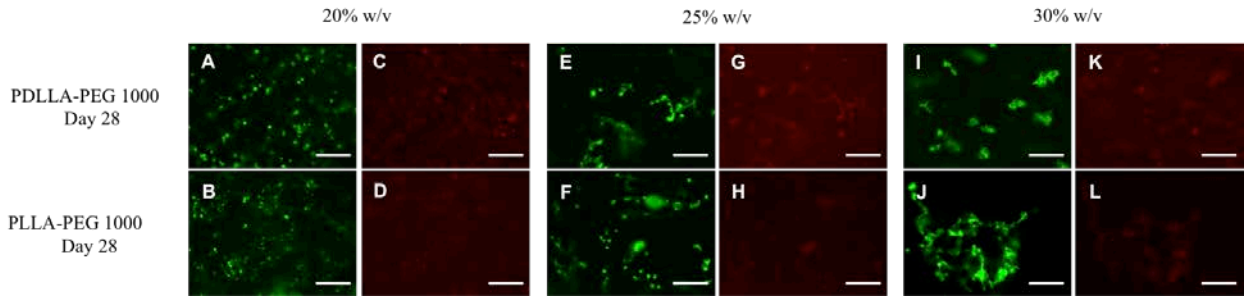

Figure 59. Cell viability in hydrogel constructs. (A,B,E,F,I,J) Calcein-AM staining (green, live cells) and **(C,D,G,H,K,L)** EthD-1 staining (red, dead cells) in cell-seeded scaffolds observed at day 28 post-fabrication, across 20%, 25%, and 30% w/v polymer concentrations. Scale bar = 150 μm.

BIBLIOGRAPHY

1. Griffin JW, Hogan M V, Chhabra a B, Deal DN. Peripheral nerve repair and reconstruction. *J Bone Jt Surg Am*. 2013;95(23):2144-2151. doi:10.2106/jbjs.l.00704.

2. Wiberg M, Terenghi G. Will it be possible to produce peripheral nerves? *Surg Technol Int*. 2003;11:303-310.

3. Novak CB, Anastakis DJ, Beaton DE, Katz J. Patient-reported outcome after peripheral nerve injury. *J Hand Surg Am*. 2009;34(2):281-287. doi:10.1016/j.jhsa.2008.11.017.

4. Novak CB, Anastakis DJ, Beaton DE, Katz J. Evaluation of pain measurement practices and opinions of peripheral nerve surgeons. *Hand (N Y)*. 2009;4(4):344-349. doi:10.1007/s11552-009-9177-8.

5. Rivera JC, Glebus GP, Cho MS. Disability following combat-sustained nerve injury of the upper limb. *Bone Joint J*. 2014;96-B(2):254-258. doi:10.1302/0301-620X.96B2.31798.

6. Goodfellow JA, Willison HJ. Gangliosides and Autoimmune Peripheral Nerve Diseases. In: *Progress in Molecular Biology and Translational Science*. Vol 156. ; 2018:355-382. doi:10.1016/bs.pmbts.2017.12.010.

7. Hilton DA, Hanemann CO. Schwannomas and their pathogenesis. *Brain Pathol*. 2014;24(3):205-220. doi:10.1111/bpa.12125.

8. Menorca RMG, Fussell TS, Elfar JC. Nerve physiology. Mechanisms of injury and recovery. *Hand Clin*. 2013;29(3):317-330. doi:10.1016/j.hcl.2013.04.002.

9. Seddon HJ. Three types of nerve injury. *Brain*. 1943;66(4):237-288. doi:10.1093/brain/66.4.237.

10. Sunderland S. A classification of peripheral nerve injuries producing loss of function. *Brain*. 1951;74(4):491-516. doi:10.1093/brain/74.4.491.

11. Deumens R, Bozkurt A, Meek MF, et al. Repairing injured peripheral nerves: Bridging the gap. *Prog Neurobiol*. 2010;92(3):245-276. doi:10.1016/j.pneurobio.2010.10.002.

12. Sunderland S. A classification of peripheral nerve injuries producing loss of function. *Brain*. 1951;74(4):491-516. doi:http://dx.doi.org/10.1093/brain/74.4.491.

13. Zochodne DW. The challenges and beauty of peripheral nerve regrowth. In: *Journal of the Peripheral Nervous System*. Vol 17. ; 2012:1-18. doi:10.1111/j.1529-8027.2012.00378.x.

14. Grinsell D, Keating CP. Peripheral Nerve Reconstruction after Injury: A Review of Clinical and Experimental Therapies. *Biomed Res Int*. 2014;2014. doi:10.1155/2014/698256.

15. López Cebral R, Silva-Correia J, Reis RL, Silva TH, Oliveira JM. Peripheral nerve injury: Current challenges, conventional treatment approaches and new trends on biomaterials-based regenerative strategies. *ACS Biomater Sci Eng*. 2017:acsbiomaterials.7b00655. doi:10.1021/acsbiomaterials.7b00655.

16. Noaman HH. Surgical Treatment of Peripheral Nerve Injury. In: Rayegani SM, ed. *Basic Principles of Peripheral Nerve Disorders*. Vol ; 2012:93-132.

17. Li R, Liu Z, Pan Y, Chen L, Zhang Z, Lu L. Peripheral Nerve Injuries Treatment: A Systematic Review. *Cell Biochem Biophys*. 2014;68(3):449-454. doi:10.1007/s12013-013-9742-1.

18. Daly W, Yao L, Zeugolis D, Windebank A, Pandit A. A biomaterials approach to peripheral nerve regeneration: bridging the peripheral nerve gap and enhancing functional recovery. *J R Soc Interface*. 2012;9(67):202-221. doi:10.1098/rsif.2011.0438.

19. Kehoe S, Zhang XF, Boyd D. FDA approved guidance conduits and wraps for peripheral nerve injury: A review of materials and efficacy. *Injury*. 2012;43(5):553-572. doi:10.1016/j.injury.2010.12.030.

20. Gaudin R, Knipfer C, Henningsen A, Smeets R, Heiland M, Hadlock T. Approaches to peripheral nerve repair: Generations of biomaterial conduits yielding to replacing autologous nerve grafts in craniomaxillofacial surgery. *Biomed Res Int*. 2016;2016. doi:10.1155/2016/3856262.

21. Kingham PJ, Terenghi G. Bioengineered nerve regeneration and muscle reinnervation. *J Anat*. 2006;209(4):511-526. doi:10.1111/j.1469-7580.2006.00623.x.

22. Allodi I, Udina E, Navarro X. Specificity of peripheral nerve regeneration: interactions at the axon level. *Prog Neurobiol*. 2012;98(1):16-37. doi:10.1016/j.pneurobio.2012.05.005.

23. Belkas JS, Shoichet MS, Midha R. Peripheral nerve regeneration through guidance tubes. *Neurol Res*. 2004;26(2):151-160. doi:10.1179/016164104225013798.

24. R L-M, Angeletti PU. Nerve growth factor. *Physiol Rev*. 1968.

25. Levi-Montalcini R, Meyer H, Hamburger V. In Vitro Experiments on the Effects of Mouse Sarcomas 180 and 37 on the Spinal and Sympathetic Ganglia of the Chick Embryo. *Cancer Res*. 1954;14(1):49-57.

26. Cohen S, Levi-Montalcini R, Hamburger V. A Nerve Growth-Stimulating Factor Isolated From Sarcomas 37 and 180. *Proc Natl Acad Sci*. 1954;40(10):1014 LP - 1018. http://www.pnas.org/content/40/10/1014.abstract.

27. Önger ME, Delibaş B, Türkmen AP, Erener E, Altunkaynak BZ, Kaplan S. The role of growth factors in nerve regeneration. *Drug Discov Ther*. 2016;10(6):285-291. doi:10.5582/ddt.2016.01058.

28. Levi-Montalcini R. The nerve growth factor: Thirty-five years later. *Biosci Rep*. 1987;7(9):681-699. doi:10.1007/BF01116861.

29. Zhang JY, Luo XG, Xian CJ, Liu ZH, Zhou XF. Endogenous BDNF is required for myelination and regeneration of injured sciatic nerve in rodents. *Eur J Neurosci*. 2000;12(12):4171-4180. doi:10.1046/j.1460-9568.2000.01312.x.

30. Boyd JG, Gordon T. The neurotrophin receptors, trkB and p75, differentially regulate motor axonal regeneration. *J Neurobiol*. 2001;49(4):314-325. doi:10.1002/neu.10013.

31. Airaksinen MS, Koltzenburg M, Lewin GR, et al. Specific subtypes of cutaneous mechanoreceptors require neurotrophin-3 following peripheral target innervation. *Neuron*. 1996;16(2):287-295. doi:10.1016/S0896-6273(00)80047-1.

32. Ernfors P, Rosario CM, Merlio J-P, Grant G, Aldskogius H, Persson H. Expression of mRNAs for neurotrophin receptors in the dorsal root ganglion and spinal cord during development and following peripheral or central axotomy. *Mol Brain Res*. 1993;17(3-4). doi:10.1016/0169-328X(93)90005-A.

33. Sterne GD, Brown RA, Green CJ, Terenghi G. Neurotrophin-3 delivered locally via fibronectin mats enhances peripheral nerve regeneration. *Eur J Neurosci*. 1997;9(7):1388-1396. doi:10.1111/j.1460-9568.1997.tb01493.x.

34. Braun S, Croizat B, Lagrange MC, Waiter JM, Poindron P. Neurotrophins increase motoneurons' ability to innervate skeletal muscle fibers in rat spinal cord-human muscle cocultures. *J Neurol Sci*. 1996;136(1-2):17-23. doi:10.1016/0022-510X(95)00315-S.

35. Simon M, Porter R, Brown R, Coulton GR, Terenghi G. Effect of NT-4 and BDNF delivery to damaged sciatic nerves on phenotypic recovery of fast and slow muscles fibres. *Eur J Neurosci*. 2003;18(9):2460-2466. doi:10.1046/j.1460-9568.2003.02978.x.

36. Terenghi G. Peripheral nerve regeneration and neurotrophic factors. *J Anat*. 1999;194(1):1-14. doi:10.1017/S0021878298004312.

37. Gordon T. The role of neurotrophic factors in nerve regeneration. *Neurosurg Focus*. 2009;26(2):E3. doi:10.3171/FOC.2009.26.2.E3.

38. Lykissas MG, Batistatou AK, Charalabopoulos K a, Beris AE. The role of neurotrophins in axonal growth, guidance, and regeneration. *Curr Neurovasc Res*. 2007;4(2):143-151. doi:10.2174/156720207780637216.

39. Trupp M, Rydén M, Jörnvall H, et al. Peripheral expression and biological activities of GDNF, a new neurotrophic factor for avian and mammalian peripheral neurons. *J Cell Biol*. 1995;130(1):137-148. doi:10.1083/jcb.130.1.137.

40. Henderson CE, Phillips HS, Pollock RA, et al. GDNF: A potent survival factor for motoneurons present in peripheral nerve and muscle. *Science (80-)*. 1994;266(5187):1062-1064. doi:10.1126/science.7973664.

41. Ebendal T, Tomac A, Hoffer BJ, Olson L. Glial cell line-derived neurotrophic factor stimulates fiber formation and survival in cultured neurons from peripheral autonomic ganglia. *J Neurosci Res*. 1995;40(2):276-284. doi:10.1002/jnr.490400217.

42. Buj-Bello A, Buchman VL, Horton A, Rosenthal A, Davies AM. GDNF is an age-specific survival factor for sensory and autonomic neurons. *Neuron*. 1995;15(4):821-828. doi:10.1016/0896-6273(95)90173-6.

43. Höke A, Ho T, Crawford TO, LeBel C, Hilt D, Griffin JW. Glial cell line-derived neurotrophic factor alters axon schwann cell units and promotes myelination in unmyelinated nerve fibers. *J Neurosci*. 2003;23(2):561-567. doi:10.1002/jbm.a.30587.

44. Madduri S, Papaloïzos M, Gander B. Synergistic effect of GDNF and NGF on axonal branching and elongation in vitro. *Neurosci Res*. 2009;65(1):88-97. doi:10.1016/j.neures.2009.06.003.

45. Madduri S, di Summa P, Papaloïzos M, Kalbermatten D, Gander B. Effect of controlled co-delivery of synergistic neurotrophic factors on early nerve regeneration in rats. *Biomaterials*. 2010;31(32):8402-8409. doi:10.1016/j.biomaterials.2010.07.052.

46. Chiono V, Tonda-Turo C. Trends in the design of nerve guidance channels in peripheral nerve tissue engineering. *Prog Neurobiol*. 2015. doi:10.1016/j.pneurobio.2015.06.001.

47. Wang HB, Mullins ME, Cregg JM, McCarthy CW, Gilbert RJ. Varying the diameter of aligned electrospun fibers alters neurite outgrowth and Schwann cell migration. *Acta Biomater*. 2010;6(8):2970-2978. doi:10.1016/j.actbio.2010.02.020.

48. Schnell E, Klinkhammer K, Balzer S, et al. Guidance of glial cell migration and axonal growth on electrospun nanofibers of poly-[epsilon]-caprolactone and a collagen/poly-[epsilon]-caprolactone blend. *Biomaterials*. 2007;28(19):3012-3025. doi:10.1016/j.biomaterials.2007.03.009.

49. Hoffman-Kim D, Mitchel JA, Bellamkonda R V. Topography, Cell Response, and Nerve Regeneration. *Annu Rev Biomed Eng*. 2010;12(1):203-231. doi:10.1146/annurev-bioeng-070909-105351.

50. Pinho AC, Fonseca AC, Serra AC, Santos JD, Coelho JFJ. Peripheral Nerve Regeneration: Current Status and New Strategies Using Polymeric Materials. *Adv Healthc Mater*. 2016;5(21):2732-2744. doi:10.1002/adhm.201600236.

51. Gao Z, Wang H, Luo XT. Progress in nerve conduit biomaterials. *J Clin Rehabil Tissue Eng Res*. 2007;11(31):6239-6243.

52. Fairbairn NG, Meppelink AM, Ng-Glazier J, Randolph MA, Winograd JM. Augmenting peripheral nerve regeneration using stem cells: A review of current opinion. *World J Stem Cells*. 2015;7(1):11-26. doi:10.4252/wjsc.v7.i1.11.

53. Morrissey TK, Kleitman N, Bunge RP. Isolation and functional characterization of Schwann cells derived from adult peripheral nerve. *J Neurosci*. 1991;11(8):2433-2442. doi:10.1002/0471142735.im1402s83.

54. Levi a D. Characterization of the technique involved in isolating Schwann cells from adult human peripheral nerve. *J Neurosci Methods*. 1996;68(1):21-26. http://www.ncbi.nlm.nih.gov/pubmed/8884609.

55. Morrissey TK, Levi a D, Nuijens a, Sliwkowski MX, Bunge RP. Axon-induced mitogenesis of human Schwann cells involves heregulin and p185erbB2. *Proc Natl Acad Sci U S A*. 1995;92(5):1431-1435. doi:10.1073/pnas.92.5.1431.

56. Levi a D, Bunge RP, Lofgren J a, et al. The influence of heregulins on human Schwann cell proliferation. *J Neurosci*. 1995;15(2):1329-1340.

57. Casella GTB, Bunge RP, Wood PM. Improved method for harvesting human Schwann cells from mature peripheral nerve and expansion in vitro. *Glia*. 1996;17(4):327-338. doi:10.1002/(SICI)1098-1136(199608)17:4<327::AID-GLIA7>3.0.CO;2-W.

58. Levi a D, Guénard V, Aebischer P, Bunge RP. The functional characteristics of Schwann cells cultured from human peripheral nerve after transplantation into a gap within the rat sciatic nerve. *J Neurosci*. 1994;14(3 Pt 1):1309-1319. http://www.ncbi.nlm.nih.gov/pubmed/8120626.

59. Levi AD, Burks SS, Anderson KD, Dididze M, Khan A, Dietrich WD. The use of autologous Schwann cells to supplement sciatic nerve repair with a large gap - First in human experience. *Cell Transplant*. 2016;25(305):1-26. doi:10.3727/096368915X690198.

60. Evans PJ, Mackinnon SE, Levi ADO, et al. Cold preserved nerve allografts: Changes in basement membrane, viability, immunogenicity, and regeneration. *Muscle and Nerve*. 1998;21(11):1507-1522. doi:10.1002/(SICI)1097-4598(199811)21:11<1507::AID-MUS21>3.0.CO;2-W.

61. Levi ADO, Evans PJ, Mackinnon SE, Bunge RP. Cold storage of peripheral nerves: An in vitro assay of cell viability and function. *Glia*. 1994;10(2):121-131. doi:10.1002/glia.440100206.

62. Emery E, Li X, Brunschwig JP, Olson L, Levi AD. Assessment of the malignant potential of mitogen stimulated human Schwann cells. *J Peripher Nerv Syst*. 1999;4(2):107-116. http://www.ncbi.nlm.nih.gov/pubmed/10442686.

63. Levi ADO, Sonntag VKH, Dickman C, et al. The role of cultured Schwann cell grafts in the repair of gaps within the peripheral nervous system of primates. *Exp Neurol*. 1997;143(1):25-36. doi:10.1006/exnr.1996.6344.

64. Levi ADO, Bunge RP. Studies of myelin formation after transplantation of human schwann cells into the severe combined immunodeficient mouse. *Exp Neurol*. 1994;130(1):41-52. doi:10.1006/exnr.1994.1183.

65. Berrocal YA, Almeida VW, Gupta R, Levi AD. Transplantation of Schwann cells in a collagen tube for the repair of large, segmental peripheral nerve defects in rats. *J Neurosurg*. 2013;119(3):720-732. doi:10.3171/2013.4.JNS121189.

66. Rodríguez FJ, Verdú E, Ceballos D, Navarro X. Nerve guides seeded with autologous Schwann cells improve nerve regeneration. *Exp Neurol*. 2000;161(2):571-584. doi:10.1006/exnr.1999.7315.

67. Liard O, Segura S, Sagui E, et al. Adult-brain-derived neural stem cells grafting into a vein bridge increases postlesional recovery and regeneration in a peripheral nerve of adult pig. *Stem Cells Int*. 2012. doi:10.1155/2012/128732.

68. Guo BF, Dong MM. Application of neural stem cells in tissue-engineered artificial nerve. *Otolaryngol - Head Neck Surg*. 2009;140(2):159-164. doi:10.1016/j.otohns.2008.10.039.

69. Murakami T, Fujimoto Y, Yasunaga Y, et al. Transplanted neuronal progenitor cells in a peripheral nerve gap promote nerve repair. *Brain Res*. 2003;974(1-2):17-24. doi:10.1016/S0006-8993(03)02539-3.

70. Zhang H, Wei YT, Tsang KS, et al. Implantation of neural stem cells embedded in hyaluronic acid and collagen composite conduit promotes regeneration in a rabbit facial nerve injury model. *J Transl Med*. 2008;6. doi:10.1186/1479-5876-6-67.

71. Fu K-Y, Dai L-G, Chiu I-M, Chen J-R, Hsu S. Sciatic Nerve Regeneration by Microporous Nerve Conduits Seeded With Glial Cell Line-Derived Neurotrophic Factor or Brain-Derived Neurotrophic Factor Gene Transfected Neural Stem Cells. *Artif Organs*. 2011;35(4):363-372. doi:10.1111/j.1525-1594.2010.01105.x.

72. Johnson TS, O'Neill AC, Motarjem PM, Nazzal J, Randolph M, Winograd JM. Tumor formation following murine neural precursor cell transplantation in a rat peripheral nerve injury model. *J Reconstr Microsurg*. 2008;24(8):545-550. doi:10.1055/s-0028-1088228.

73. Yamanaka KT and S. Induction of Pluripotent Stem Cells from Mouse Embryonic and Adult Fibroblast Cultures by Defined Factors. *Cell*. 2006;126:663-676. http://download.cell.com/pdfs/0092-8674/PIIS0092867406009767.pdf\nhttp://www.cell.com/content/article/fulltext?uid=PIIS0092867406009767.

74. Thomson JA. Embryonic Stem Cell Lines Derived from Human Blastocysts. *Science (80-)*. 1998;282(5391):1145-1147. doi:10.1126/science.282.5391.1145.

75. Wang A, Tang Z, Park I-H, et al. Induced pluripotent stem cells for neural tissue engineering. *Biomaterials*. 2011;32(22):5023-5032. doi:10.1016/j.biomaterials.2011.03.070.

76. Uemura T, Takamatsu K, Ikeda M, et al. Transplantation of induced pluripotent stem cell-derived neurospheres for peripheral nerve repair. *Biochem Biophys Res Commun*. 2012;419(1):130-135. doi:10.1016/j.bbrc.2012.01.154.

77. Ikeda M, Uemura T, Takamatsu K, et al. Acceleration of peripheral nerve regeneration using nerve conduits in combination with induced pluripotent stem cell technology and a basic fibroblast growth factor drug delivery system. *J Biomed Mater Res - Part A*. 2014;102(5):1370-1378. doi:10.1002/jbm.a.34816.

78. Kubo T, Randolph MA, Gröger A, Winograd JM. Embryonic stem cell-derived motor neurons form neuromuscular junctions in vitro and enhance motor functional recovery in vivo. In: *Plastic and Reconstructive Surgery*. Vol 123. ; 2009. doi:10.1097/PRS.0b013e3181923d07.

79. Craff MN, Zeballos JL, Johnson TS, et al. Embryonic stem cell-derived motor neurons preserve muscle after peripheral nerve injury. *Plast Reconstr Surg*. 2007;119(1):235-245. doi:10.1097/01.prs.0000244863.71080.f0.

80. Lee EJ, Xu L, Kim G-H, et al. Regeneration of peripheral nerves by transplanted sphere of human mesenchymal stem cells derived from embryonic stem cells. *Biomaterials*. 2012;33(29):7039-7046. doi:10.1016/j.biomaterials.2012.06.047.

81. Lin C, Jun J, Ling W, et al. Transplantation of Embryonic Stem Cells Improves Nerve Repair and Functional Recovery After Severe Sciatic Nerve Axotomy in Rats. *Stem Cells*. 2008;26(5):1356-1365. doi:10.1634/stemcells.2007-0333.

82. Pittenger MF. Multilineage Potential of Adult Human Mesenchymal Stem Cells. *Science (80-)*. 1999;284:143-147. doi:10.1126/science.284.5411.143.

83. Ullah I, Baregundi Subbarao R, Rho G-J. Human Mesenchymal Stem Cells - Current trends and future prospective. *Biosci Rep*. 2015;35(2):e00191. doi:10.1042/BSR20150025.

84. Pereira Lopes FR, Camargo de Moura Campos L, Dias Corrêa J, et al. Bone marrow stromal cells and resorbable collagen guidance tubes enhance sciatic nerve regeneration in mice. *Exp Neurol*. 2006;198(2):457-468. doi:10.1016/j.expneurol.2005.12.019.

85. Nijhuis THJ, Brzezicki G, Klimczak A, Siemionow M. Isogenic venous graft supported with bone marrow stromal cells as a natural conduit for bridging a 20 mm nerve gap. *Microsurgery*. 2010;30(8):639-645. doi:10.1002/micr.20818.

86. Nijhuis THJ, Bodar CWJ, Van Neck JW, et al. Natural conduits for bridging a 15-mm nerve defect: Comparison of the vein supported by muscle and bone marrow stromal cells with a nerve autograft. *J Plast Reconstr Aesthetic Surg*. 2013;66(2):251-259. doi:10.1016/j.bjps.2012.09.011.

87. Wakao S, Hayashi T, Kitada M, et al. Long-term observation of auto-cell transplantation in non-human primate reveals safety and efficiency of bone marrow stromal cell-derived Schwann cells in peripheral nerve regeneration. *Exp Neurol*. 2010;223(2):537-547. doi:10.1016/j.expneurol.2010.01.022.

88. Ao Q, Fung CK, Yat-Ping Tsui A, et al. The regeneration of transected sciatic nerves of adult rats using chitosan nerve conduits seeded with bone marrow stromal cell-derived Schwann cells. *Biomaterials*. 2011;32(3):787-796. doi:10.1016/j.biomaterials.2010.09.046.

89. Zarbakhsh S, Bakhtiyari M, Faghihi a, et al. The effects of schwann and bone marrow stromal stem cells on sciatic nerve injury in rat: a comparison of functional recovery. *Cell J*. 2012;14(1):39-46. http://www.ncbi.nlm.nih.gov/entrez/query.fcgi?cmd=Retrieve&db=PubMed&dopt=Citation&list_uids=23626936.

90. Ladak A, Olson J, Tredget EE, Gordon T. Differentiation of mesenchymal stem cells to support peripheral nerve regeneration in a rat model. *Exp Neurol*. 2011;228(2):242-252. doi:10.1016/j.expneurol.2011.01.013.

91. Tohill M, Mantovani C, Wiberg M, Terenghi G. Rat bone marrow mesenchymal stem cells express glial markers and stimulate nerve regeneration. *Neurosci Lett*. 2004;362(3):200-203. doi:10.1016/j.neulet.2004.03.077.

92. Strem BM, Hicok KC, Zhu M, et al. Multipotential differentiation of adipose tissue-derived stem cells. *Keio J Med*. 2005;54(3):132-141. doi:10.2302/kjm.54.132.

93. Santiago LY, Clavijo-Alvarez J, Brayfield C, Rubin JP, Marra KG. Delivery of adipose-derived precursor cells for peripheral nerve repair. *Cell Transplant*. 2009;18(2):145-158. doi:10.3727/096368909788341289.

94. Liu G-B, Cheng Y-X, Feng Y-K, et al. Adipose-derived stem cells promote peripheral nerve repair. *Arch Med Sci*. 2011;4:592-596. doi:10.5114/aoms.2011.24127.

95. Di Summa PG, Kingham PJ, Raffoul W, Wiberg M, Terenghi G, Kalbermatten DF. Adipose-derived stem cells enhance peripheral nerve regeneration. *J Plast Reconstr Aesthetic Surg*. 2010;63(9):1544-1552. doi:10.1016/j.bjps.2009.09.012.

96. di Summa PG, Kalbermatten DF, Pralong E, Raffoul W, Kingham PJ, Terenghi G. Long-term in vivo regeneration of peripheral nerves through bioengineered nerve grafts. *Neuroscience*. 2011;181:278-291. doi:10.1016/j.neuroscience.2011.02.052.

97. Liu G, Cheng Y, Guo S, et al. Transplantation of adipose-derived stem cells for peripheral nerve repair. *Int J Mol Med*. 2011;28(4):565-572. doi:10.3892/ijmm.2011.725.

98. Orbay H, Uysal AC, Hyakusoku H, Mizuno H. Differentiated and undifferentiated adipose-derived stem cells improve function in rats with peripheral nerve gaps. *J Plast Reconstr Aesthetic Surg*. 2012;65(5):657-664. doi:10.1016/j.bjps.2011.11.035.

99. Erba P, Mantovani C, Kalbermatten DF, Pierer G, Terenghi G, Kingham PJ. Regeneration potential and survival of transplanted undifferentiated adipose tissue-derived stem cells in peripheral nerve conduits. *J Plast Reconstr Aesthetic Surg*. 2010;63(12). doi:10.1016/j.bjps.2010.08.013.

100. Mohammadi R, Azizi S, Delirezh N, Hobbenaghi R, Amini K. Comparison of beneficial effects of undifferentiated cultured bone marrow stromal cells and omental adipose-derived nucleated cell fractions on sciatic nerve regeneration. *Muscle and Nerve*. 2011;43(2):157-163. doi:10.1002/mus.21895.

101. Cheng F-C, Tai M-H, Sheu M-L, et al. Enhancement of regeneration with glia cell line-derived neurotrophic factor-transduced human amniotic fluid mesenchymal stem cells after sciatic nerve crush injury. *J Neurosurg*. 2010;112(4):868-879. doi:10.3171/2009.8.JNS09850.

102. Pan H-C, Chin C-S, Yang D-Y, et al. Human amniotic fluid mesenchymal stem cells in combination with hyperbaric oxygen augment peripheral nerve regeneration. *Neurochem Res*. 2009;34(7):1304-1316. doi:10.1007/s11064-008-9910-7.

103. Pan H-C, Chen C-J, Cheng F-C, et al. Combination of G-CSF administration and human amniotic fluid mesenchymal stem cell transplantation promotes peripheral nerve regeneration. *Neurochem Res*. 2008;34(3):518-527. doi:10.1007/s11064-008-9815-5.

104. Matsuse D, Kitada M, Kohama M, et al. Human umbilical cord-derived mesenchymal stromal cells differentiate into functional schwann cells that sustain peripheral nerve regeneration. *J Neuropathol Exp Neurol*. 2010;69(9):973-985. doi:10.1097/NEN.0b013e3181eff6dc.

105. Gärtner A, Pereira T, Armada-da-Silva PAS, et al. Use of poly(DL-lactide-ε-caprolactone) membranes and mesenchymal stem cells from the Wharton's jelly of the umbilical cord for promoting nerve regeneration in axonotmesis: In vitro and in vivo analysis. *Differentiation*. 2012;84(5):355-365. doi:10.1016/j.diff.2012.10.001.

106. Pan HC, Cheng FC, Chen CJ, et al. Post-injury regeneration in rat sciatic nerve facilitated by neurotrophic factors secreted by amniotic fluid mesenchymal stem cells. *J Clin Neurosci*. 2007;14(11):1089-1098. doi:10.1016/j.jocn.2006.08.008.

107. Biernaskie JA, McKenzie IA, Toma JG, Miller FD. Isolation of skin-derived precursors (SKPs) and differentiation and enrichment of their Schwann cell progeny. *Nat Protoc*. 2007;1(6):2803-2812. doi:10.1038/nprot.2006.422.

108. Sieber-Blum M, Grim M, Hu YF, Szeder V. Pluripotent neural crest stem cells in the adult hair follicle. *Dev Dyn*. 2004;231(2):258-269. doi:10.1002/dvdy.20129.

109. Yu H, Kumar SM, Kossenkov A V, Showe L, Xu X. Stem cells with neural crest characteristics derived from the bulge region of cultured human hair follicles. *J Invest Dermatol*. 2010;130(5):1227-1236. doi:10.1038/jid.2009.322.

110. Yu H, Fang D, Kumar SM, et al. Isolation of a Novel Population of Multipotent Adult Stem Cells from Human Hair Follicles. *Am J Pathol*. 2006;168(6):1879-1888. doi:10.2353/ajpath.2006.051170.

111. Amoh Y, Li L, Campillo R, et al. Implanted hair follicle stem cells form Schwann cells that support repair of severed peripheral nerves. *Proc Natl Acad Sci U S A*. 2005;102(49):17734-17738. doi:10.1073/pnas.0508440102.

112. Amoh Y, Kanoh M, Niiyama S, et al. Human hair follicle pluripotent stem (hfPS) cells promote regeneration of peripheral-nerve injury: An advantageous alternative to ES and iPS cells. *J Cell Biochem*. 2009;107(5):1016-1020. doi:10.1002/jcb.22204.

113. AMOH Y, AKI R, HAMADA Y, et al. Nestin-positive hair follicle pluripotent stem cells can promote regeneration of impinged peripheral nerve injury. *J Dermatol*. 2012;39(1):33-38. doi:10.1111/j.1346-8138.2011.01413.x.

114. Martens W, Sanen K, Georgiou M, et al. Human dental pulp stem cells can differentiate into Schwann cells and promote and guide neurite outgrowth in an aligned tissue-engineered collagen construct in vitro. *FASEB J*. 2014;28(4):1634-1643. doi:10.1096/fj.13-243980.

115. Nosrat I V., Smith CA, Mullally P, Olson L, Nosrat CA. Dental pulp cells provide neurotrophic support for dopaminergic neurons and differentiate into neurons in vitro; implications for tissue engineering and repair in the nervous system. *Eur J Neurosci*. 2004;19(9):2388-2398. doi:10.1111/j.0953-816X.2004.03314.x.

116. Nosrat I V., Widenfalk J, Olson L, Nosrat CA. Dental pulp cells produce neurotrophic factors, interact with trigeminal neurons in vitro, and rescue motoneurons after spinal cord injury. *Dev Biol*. 2001;238(1):120-132. doi:10.1006/dbio.2001.0400.

117. Madduri S, Gander B. Growth factor delivery systems and repair strategies for damaged peripheral nerves. *J Control Release*. 2012;161(2):274-282. doi:10.1016/j.jconrel.2011.11.036.

118. Ho PR, Coan GM, Cheng ET, et al. Repair with collagen tubules linked with brain-derived neurotrophic factor and ciliary neurotrophic factor in a rat sciatic nerve injury model. *Arch Otolaryngol Head Neck Surg*. 1998;124(7):761-766. http://www.ncbi.nlm.nih.gov/pubmed/9677110.

119. Aebischer P, Salessiotis AN, Winn SR. Basic fibroblast growth factor released from synthetic guidance channels facilitates peripheral nerve regeneration across long nerve gaps. *J Neurosci Res*. 1989;23(3):282-289. doi:10.1002/jnr.490230306.

120. Piquilloud G, Christen T, Pfister LA, Gander B, Papaloïzos MY. Variations in glial cell line-derived neurotrophic factor release from biodegradable nerve conduits modify the rate of functional motor recovery after rat primary nerve repairs. *Eur J Neurosci*. 2007;26(5):1109-1117. doi:10.1111/j.1460-9568.2007.05748.x.

121. Péan JM, Menei P, Morel O, Montero-Menei CN, Benoit JP. Intraseptal implantation of NGF-releasing microspheres promote the survival of axotomized cholinergic neurons. *Biomaterials*. 2000;21(20):2097-2101. doi:10.1016/S0142-9612(00)00141-1.

122. Midha R, Munro CA, Dalton PD, Tator CH, Shoichet MS. Growth factor enhancement of peripheral nerve regeneration through a novel synthetic hydrogel tube. *J Neurosurg*. 2003;99(3):555-565. doi:10.3171/jns.2003.99.3.0555.

123. Lee AC, Yu VM, Lowe JB, et al. Controlled release of nerve growth factor enhances sciatic nerve regeneration. *Exp Neurol*. 2003;184(1):295-303. doi:10.1016/S0014-4886(03)00258-9.

124. Liu JJ, Wang CY, Wang JG, Ruan HJ, Fan CY. Peripheral nerve regeneration using composite poly(lactic acid-caprolactone)/nerve growth factor conduits prepared by coaxial electrospinning. *J Biomed Mater Res - Part A*. 2011;96 A(1):13-20. doi:10.1002/jbm.a.32946.

125. Chew SY, Mi R, Hoke A, Leong KW. Aligned protein-polymer composite fibers enhance nerve regeneration: A potential tissue-engineering platform. *Adv Funct Mater*. 2007;17(8):1288-1296. doi:10.1002/adfm.200600441.

126. Chew SY, Wen J, Yim EKF, Leong KW. Sustained release of proteins from electrospun biodegradable fibers. *Biomacromolecules*. 2005;6(4):2017-2024. doi:10.1021/bm0501149.

127. Wang S, Cai L. Polymer Gel Systems for Nerve Repair and Regeneration. In: *Biomaterials*. Vol ; 2010:43-63. doi:10.1021/bk-2010-1054.ch003.

128. Jia H, Wang Y, Tong XJ, et al. Sciatic nerve repair by acellular nerve xenografts implanted with BMSCs in rats xenograft combined with BMSCs. *Synapse*. 2012;66(3):256-269. doi:10.1002/syn.21508.

129. Wang D, Liu XL, Zhu JK, et al. Bridging small-gap peripheral nerve defects using acellular nerve allograft implanted with autologous bone marrow stromal cells in primates. *Brain Res*. 2008;1188(1):44-53. doi:10.1016/j.brainres.2007.09.098.

130. Pang CJ, Tong L, Ji LL, et al. Synergistic effects of ultrashort wave and bone marrow stromal cells on nerve regeneration with acellular nerve allografts. *Synapse*. 2013;67(10):637-647. doi:10.1002/syn.21669.

131. Wang Y, Zhao Z, Ren Z, et al. Recellularized nerve allografts with differentiated mesenchymal stem cells promote peripheral nerve regeneration. *Neurosci Lett*. 2012;514(1):96-101. doi:10.1016/j.neulet.2012.02.066.

132. Zhao Z, Wang Y, Peng J, et al. Improvement in Nerve Regeneration Through a Decellularized Nerve Graft by Supplementation With Bone Marrow Stromal Cells in Fibrin. *Cell Transplant*. 2014;23(1):97-110. doi:10.3727/096368912X658845.

133. Hu Y, Wu Y, Gou Z, et al. 3D-engineering of Cellularized Conduits for Peripheral Nerve Regeneration. *Sci Rep*. 2016;6(April):32184. doi:10.1038/srep32184.

134. Shin RH, Friedrich PF, Crum BA, Bishop AT, Shin AY. Treatment of a segmental nerve defect in the rat with use of bioabsorbable synthetic nerve conduits: a comparison of commercially available conduits. *J Bone Jt Surg Am*. 2009;91(9):2194-2204. doi:10.2106/JBJS.H.01301.

135. Widgerow AD, Salibian AA, Lalezari S, Evans GRD. Neuromodulatory nerve regeneration: Adipose tissue-derived stem cells and neurotrophic mediation in peripheral nerve regeneration. *J Neurosci Res*. 2013;91(12):1517-1524. doi:10.1002/jnr.23284.

136. Price RD, Milne SA, Sharkey J, Matsuoka N. Advances in small molecules promoting neurotrophic function. *Pharmacol Ther*. 2007;115(2):292-306. doi:10.1016/j.pharmthera.2007.03.005.

137. Spivey EC, Khaing ZZ, Shear JB, Schmidt CE. The fundamental role of subcellular topography in peripheral nerve repair therapies. *Biomaterials*. 2012;33(17):4264-4276. doi:10.1016/j.biomaterials.2012.02.043.

138. Clements IP, Kim Y tae, English AW, Lu X, Chung A, Bellamkonda R V. Thin-film enhanced nerve guidance channels for peripheral nerve repair. *Biomaterials*. 2009;30(23-24):3834-3846. doi:10.1016/j.biomaterials.2009.04.022.

139. Kim Y, Haftel VK, Kumar S, Bellamkonda R V. The role of aligned polymer fiber-based constructs in the bridging of long peripheral nerve gaps. *Biomaterials*. 2008;29(21):3117-3127. doi:10.1016/j.biomaterials.2008.03.042.

140. Zupanc HRH, Alexander PG, Tuan RS. Neurotrophic support by traumatized muscle-derived multipotent progenitor cells: Role of endothelial cells and Vascular Endothelial Growth Factor-A. *Stem Cell Res Ther*. 2017;8(1):226. doi:10.1186/s13287-017-0665-4.

141. Man AJ, Kujawski G, Burns TS, et al. Neurogenic Potential of Engineered Mesenchymal Stem Cells Overexpressing VEGF. *Cell Mol Bioeng*. 2016;9(1):96-106. doi:10.1007/s12195-015-0425-4.

142. Cho Y, Shin JE, Ewan EE, Oh YM, Pita-Thomas W, Cavalli V. Activating Injury-Responsive Genes with Hypoxia Enhances Axon Regeneration through Neuronal HIF-1α. *Neuron*. 2015;88(4):720-734. doi:10.1016/j.neuron.2015.09.050.

143. Brick RM, Sun AX, Tuan RS. Neurotrophically Induced Mesenchymal Progenitor Cells Derived from Induced Pluripotent Stem Cells Enhance Neuritogenesis via Neurotrophin and Cytokine Production. *Stem Cells Transl Med*. 2018;7(1):45-58. doi:10.1002/sctm.17-0108.

144. Clements MP, Byrne E, Camarillo Guerrero LF, et al. The Wound Microenvironment Reprograms Schwann Cells to Invasive Mesenchymal-like Cells to Drive Peripheral Nerve Regeneration. *Neuron*. 2017;96(1):98-114.e7. doi:10.1016/j.neuron.2017.09.008.

145. Chang YC, Chen MH, Liao SY, et al. Multichanneled Nerve Guidance Conduit with Spatial Gradients of Neurotrophic Factors and Oriented Nanotopography for Repairing the Peripheral Nervous System. *ACS Appl Mater Interfaces*. 2017;9(43):37623-37636. doi:10.1021/acsami.7b12567.

146. Lin YC, Ramadan M, Hronik-Tupaj M, et al. Spatially controlled delivery of neurotrophic factors in silk fibroin-based nerve conduits for peripheral nerve repair. *Ann Plast Surg*. 2011;67(2):147-155. doi:10.1097/SAP.0b013e3182240346.

147. Dodla MC, Bellamkonda R V. Differences between the effect of anisotropic and isotropic laminin and nerve growth factor presenting scaffolds on nerve regeneration across long peripheral nerve gaps. *Biomaterials*. 2008;29(1):33-46. doi:10.1016/j.biomaterials.2007.08.045.

148. Yu LMY, Miller FD, Shoichet MS. The use of immobilized neurotrophins to support neuron survival and guide nerve fiber growth in compartmentalized chambers. *Biomaterials*. 2010;31(27):6987-6999. doi:10.1016/j.biomaterials.2010.05.070.

149. Moore K, Macsween M, Shoichet M. Immobilized Concentration Gradients of Neurotrophic Factors Guide Neurite Outgrowth of Primary Neurons in Macroporous Scaffolds. *Tissue Eng*. 2006;12(2):267-278. doi:10.1089/ten.2006.12.267.

150. Mortimer D, Fothergill T, Pujic Z, Richards LJ, Goodhill GJ. Growth cone chemotaxis. *Trends Neurosci*. 2008;31(2):90-98. doi:10.1016/j.tins.2007.11.008.

151. Dickson BJ. Molecular mechanisms of axon guidance. *Science*. 2002;298(5600):1959-1964. doi:10.1126/science.1072165.

152. Tang S, Zhu J, Xu Y, Xiang AP, Jiang MH, Quan D. The effects of gradients of nerve growth factor immobilized PCLA scaffolds on neurite outgrowth invitro and peripheral nerve regeneration in rats. *Biomaterials*. 2013;34(29):7086-7096. doi:10.1016/j.biomaterials.2013.05.080.

153. Keenan TM, Folch A. Biomolecular gradients in cell culture systems. *Lab Chip*. 2008;8(1):34-57. doi:10.1039/B711887B.

154. Kokai LE, Bourbeau D, Weber D, McAtee J, Marra KG. Sustained Growth Factor Delivery Promotes Axonal Regeneration in Long Gap Peripheral Nerve Repair. *Tissue Eng Part A*. 2011;17(9-10):1263-1275. doi:10.1089/ten.tea.2010.0507.

155. Kokai LE, Ghaznavi AM, Marra KG. Incorporation of double-walled microspheres into polymer nerve guides for the sustained delivery of glial cell line-derived neurotrophic factor. *Biomaterials*. 2010;31(8):2313-2322. doi:10.1016/j.biomaterials.2009.11.075.

156. Suon S, Jin H. Transient differentiation of adult human bone marrow cells into neuron-like cells in culture: development of morphological and biochemical traits is mediated by different molecular mechanisms. … *Dev*. 2004;13(6):625-635. http://online.liebertpub.com/doi/abs/10.1089/scd.2004.13.625.

157. Jackson WM, Nesti LJ, Tuan RS. Concise Review: Clinical Translation of Wound Healing Therapies Based on Mesenchymal Stem Cells. *Stem Cells Transl Med*. 2012;1(1):44-50. doi:10.5966/sctm.2011-0024.

158. Petrie Aronin CE, Tuan RS. Therapeutic potential of the immunomodulatory activities of adult mesenchymal stem cells. *Birth Defects Res Part C Embryo Today Rev*. 2010;90(1):67-74. doi:10.1002/bdrc.20174.

159. Yang G, Lin H, Rothrauff BB, Yu S, Tuan RS. Multilayered polycaprolactone/gelatin fiber-hydrogel composite for tendon tissue engineering. *Acta Biomater*. 2016;35:68-76. doi:10.1016/j.actbio.2016.03.004.

160. Nishi R. Autonomic and sensory neuron cultures. *Methods Cell Biol*. 1996;51:249-263. http://www.ncbi.nlm.nih.gov/pubmed/8722480.

161. Prest TA, Yeager E, LoPresti ST, et al. Nerve-specific, xenogeneic extracellular matrix hydrogel promotes recovery following peripheral nerve injury. *J Biomed Mater Res - Part A*. 2018;106(2):450-459. doi:10.1002/jbm.a.36235.

162. Mokarram N, Dymanus K, Srinivasan A, et al. Immunoengineering nerve repair. *Proc Natl Acad Sci*. 2017:201705757. doi:10.1073/pnas.1705757114.

163. Caterson EJ, Nesti LJ, Danielson KG, Tuan RS. Human marrow-derived mesenchymal progenitor cells: isolation, culture expansion, and analysis of differentiation. *Mol Biotechnol*. 2002;20(3):245-256. doi:10.1385/MB:20:3:245.

164. Diederichs S, Tuan RS. Functional Comparison of Human-Induced Pluripotent Stem Cell-Derived Mesenchymal Cells and Bone Marrow-Derived Mesenchymal Stromal Cells from the Same Donor. *Stem Cells Dev*. 2014;23(14):1594-1610. doi:10.1089/scd.2013.0477.

165. Fairbanks BD, Schwartz MP, Bowman CN, Anseth KS. Photoinitiated polymerization of PEG-diacrylate with lithium phenyl-2,4,6-trimethylbenzoylphosphinate: polymerization rate and cytocompatibility. *Biomaterials*. 2009;30(35):6702-6707. doi:10.1016/j.biomaterials.2009.08.055.

166. Yue K, Trujillo-de Santiago G, Alvarez MM, Tamayol A, Annabi N, Khademhosseini A. Synthesis, properties, and biomedical applications of gelatin methacryloyl (GelMA) hydrogels. *Biomaterials*. 2015;73:254-271. doi:10.1016/j.biomaterials.2015.08.045.

167. James J, Sutton LG, Werner FW, Basu N, Allison MA, Palmer AK. Morphology of the Cubital Tunnel: An Anatomical and Biomechanical Study With Implications for Treatment of Ulnar Nerve Compression. *J Hand Surg Am*. 2011;36(12):1988-1995. doi:10.1016/j.jhsa.2011.09.014.

168. Borschel GH, Kia KF, Kuzon WM, Dennis RG. Mechanical properties of acellular peripheral nerve. *J Surg Res*. 2003;114(2):133-139. doi:10.1016/S0022-4804(03)00255-5.

169. Tran RT, Thevenot P, Zhang Y, Gyawali D, Tang L, Yang J. Scaffold sheet design strategy for soft tissue engineering. *Materials (Basel)*. 2010;3(2):1375-1389. doi:10.3390/ma3021375.

170. Huynh T, Abraham G, Murray J, Brockbank K, Hagen PO, Sullivan S. Remodeling of an acellular collagen graff into a physiologically responsive neovessel. *Nat Biotechnol*. 1999;17(11):1083-1086. doi:10.1038/15062.

171. Jeffries EM, Wang Y. Incorporation of parallel electrospun fibers for improved topographical guidance in 3D nerve guides. *Biofabrication*. 2013;5(3). doi:10.1088/1758-5082/5/3/035015.

172. Kim JI, Hwang TI, Aguilar LE, Park CH, Kim CS. A Controlled Design of Aligned and Random Nanofibers for 3D Bi-functionalized Nerve Conduits Fabricated via a Novel Electrospinning Set-up. *Sci Rep*. 2016;6. doi:10.1038/srep23761.

173. Hu F, Zhang X, Liu H, et al. Neuronally differentiated adipose-derived stem cells and aligned PHBV nanofiber nerve scaffolds promote sciatic nerve regeneration. *Biochem Biophys Res Commun*. 2017;489(2):171-178. doi:10.1016/j.bbrc.2017.05.119.

174. Sowa Y, Imura T, Numajiri T, Nishino K, Fushiki S. Adipose-Derived Stem Cells Produce Factors Enhancing Peripheral Nerve Regeneration: Influence of Age and Anatomic Site of Origin. *Stem Cells Dev*. 2012;21(11):1852-1862. doi:10.1089/scd.2011.0403.

175. Sowa Y, Kishida T, Imura T, et al. Adipose-Derived Stem Cells Promote Peripheral Nerve Regeneration in Vivo without Differentiation into Schwann-Like Lineage. *Plast Reconstr Surg*. 2016;137(2):318e - 330e. doi:10.1097/01.prs.0000475762.86580.36.

176. Jao D, Mou X, Hu X. Tissue Regeneration: A Silk Road. *J Funct Biomater*. 2016;7(3):22. doi:10.3390/jfb7030022.

177. Bely AE. Evolutionary loss of animal regeneration: Pattern and process. In: *Integrative and Comparative Biology*. Vol 50. ; 2010:515-527. doi:10.1093/icb/icq118.

178. Bely AE, Nyberg KG. Evolution of animal regeneration: re-emergence of a field. *Trends Ecol Evol*. 2010;25(3):161-170. doi:10.1016/j.tree.2009.08.005.

179. Londono R, Sun AX, Tuan RS, Lozito TP. Tissue Repair and Epimorphic Regeneration: an Overview. *Curr Pathobiol Rep*. 2018. doi:https://doi.org/10.1007/s40139-018-0161-2.

180. Sugiura T, Wang H, Barsacchi R, Simon A, Tanaka EM. MARCKS-like protein is an initiating molecule in axolotl appendage regeneration. *Nature*. 2016;531(7593):237-240. doi:10.1038/nature16974.

181. Hutchison C, Pilote M, Roy S. The axolotl limb: A model for bone development, regeneration and fracture healing. *Bone*. 2007;40(1):45-56. doi:10.1016/j.bone.2006.07.005.

182. McCusker C, Gardiner DM. The axolotl model for regeneration and aging research: A mini-review. *Gerontology*. 2011;57(6):565-571. doi:10.1159/000323761.

183. Mchedlishvili L, Mazurov V, Grassme KS, Goehler K, Robl B. Reconstitution of the central and peripheral nervous system during salamander tail regeneration. *Proc Natl Acad Sci*. 2012;109(34):E2258-E2266. doi:10.1073/pnas.1116738109.

184. Satoh A, Makanae A, Nishimoto Y, Mitogawa K. Evolution of Developmental Control Mechanisms FGF and BMP derived from dorsal root ganglia regulate blastema induction in limb regeneration in Ambystoma mexicanum. *Dev Biol*. 2016;417(1):114-125. doi:10.1016/j.ydbio.2016.07.005.

185. Schnapp E. Hedgehog signaling controls dorsoventral patterning, blastema cell proliferation and cartilage induction during axolotl tail regeneration. *Development*. 2005;132(14):3243-3253. doi:10.1242/dev.01906.

186. Voss SR, Epperlein HH, Tanaka EM. Ambystoma mexicanum , the Axolotl : A Versatile Amphibian Model for Regeneration , Development , and Evolution Studies. 2017;4(8):1-9. doi:10.1101/pdb.emo128.

187. Gromberg E, Oliveira CR, Drechsel D, Nacu E, Tanaka EM. FGF8 and SHH substitute for anterior–posterior tissue interactions to induce limb regeneration. *Nature*. 2016;533(7603):407-410. doi:10.1038/nature17972.

188. Kragl M, Knapp D, Nacu E, et al. Cells keep a memory of their tissue origin during axolotl limb regeneration. *Nature*. 2009;460(7251):60-65. doi:10.1038/nature08152.

189. Sandoval-Guzmán T, Wang H, Khattak S, et al. Fundamental differences in dedifferentiation and stem cell recruitment during skeletal muscle regeneration in two salamander species. *Cell Stem Cell*. 2014;14(2):174-187. doi:10.1016/j.stem.2013.11.007.

190. Alibardi L. Morphological and cellular aspects of tail and limb regeneration in lizards: A model system with implications for tissue regeneration in mammals. *Adv Anat Embryol Cell Biol*. 2010;207:1-122. doi:10.1007/978-3-642-03733-7_1.

191. Lozito TP, Tuan RS. Lizard tail regeneration as an instructive model of enhanced healing capabilities in an adult amniote. *Connect Tissue Res*. 2017;58(2):145-154. doi:10.1080/03008207.2016.1215444.

192. McLean KE, Vickaryous MK. A novel amniote model of epimorphic regeneration: The leopard gecko, Eublepharis macularius. *BMC Dev Biol*. 2011;11. doi:10.1186/1471-213X-11-50.

193. Ritzman TB, Stroik LK, Julik E, et al. The Gross Anatomy of the Original and Regenerated Tail in the Green Anole (Anolis carolinensis). 2012;1608(July):1596-1608. doi:10.1002/ar.22524.

194. Fisher RE, Geiger LA, Stroik LK, et al. A Histological Comparison of the Original and Regenerated Tail in the Green Anole, *Anolis carolinensis*. *Anat Rec Adv Integr Anat Evol Biol*. 2012;295(10):1609-1619. doi:10.1002/ar.22537.

195. Bellairs A, Bryant SV. Autotomy and regeneration in reptiles. In: *Biology of the Reptilia, Vol. 15: Development B*. Vol ; 1985:301-410.

196. Lozito TP, Tuan RS. Lizard tail skeletal regeneration combines aspects of fracture healing and blastema-based regeneration. *Development*. 2016;143(16):2946-2957. doi:10.1242/dev.129585.

197. Dessaud E, McMahon AP, Briscoe J. Pattern formation in the vertebrate neural tube: a sonic hedgehog morphogen-regulated transcriptional network. *Development*. 2008;135(15):2489-2503. doi:10.1242/dev.009324.

198. Briscoe J, Small S. Morphogen rules: design principles of gradient-mediated embryo patterning. *Development*. 2015;142(23):3996-4009. doi:10.1242/dev.129452.

199. Mchedlishvili L, Epperlein HH, Telzerow A, Tanaka EM. A clonal analysis of neural progenitors during axolotl spinal cord regeneration reveals evidence for both spatially restricted and multipotent progenitors. *Development*. 2007;134(11):2083-2093. doi:10.1242/dev.02852.

200. Albors AR, Tazaki A, Rost F, Nowoshilow S, Chara O, Tanaka EM. Planar cell polarity-mediated induction of neural stem cell expansion during axolotl spinal cord regeneration. *Elife*. 2015;4(NOVEMBER2015):1-29. doi:10.7554/eLife.10230.

201. Lozito TP, Tuan RS. Lizard tail regeneration : regulation of two distinct cartilage regions by Indian hedgehog. *Dev Biol*. 2015;399(2):249-262. doi:10.1016/j.ydbio.2014.12.036.

202. Maden M, Manwell LA, Ormerod BK. Proliferation zones in the axolotl brain and regeneration of the telencephalon. *Neural Dev*. 2013;8(1). doi:10.1186/1749-8104-8-1.

203. Zhou Y, Xu Q, Li D, et al. Early neurogenesis during caudal spinal cord regeneration in adult Gekko japonicus. *J Mol Histol*. 2013;44(3):291-297. doi:10.1007/s10735-012-9466-3.

204. Gilbert EAB, Vickaryous MK. Neural stem/progenitor cells are activated during tail regeneration in the leopard gecko (Eublepharis macularius). *J Comp Neurol*. 2018;526(2):285-309. doi:10.1002/cne.24335.

205. Stemple DL, Anderson DJ. Isolation of a stem cell for neurons and glia from the mammalian neural crest. *Cell*. 1992;71(6):973-985. doi:10.1016/0092-8674(92)90393-Q.

206. Reynolds BA, Weiss S. Generation of neurons and astrocytes from isolated cells of the adult mammalian central nervous system. *Science*. 1992;255(5052):1707-1710. doi:10.1126/science.1553558.

207. Rao MS. Multipotent and restricted precursors in the central nervous system. *Anat Rec*. 1999;257(4):137-148. doi:10.1002/(SICI)1097-0185(19990815)257:4<137::AID-AR7>3.0.CO;2-Q.

208. Reynolds B a, Tetzlaff W, Weiss S. A multipotent EGF-responsive striatal embryonic progenitor cell produces neurons and astrocytes. *J Neurosci*. 1992;12(11):4565-4574. doi:0270-6474.

209. Cattaneo E, McKay R. Proliferation and differentiation of neuronal stem cells regulated by nerve growth factor. *Nature*. 1990;347(6295):762-765. doi:10.1038/347762a0.

210. Temple S. Division and differentiation of isolated CNS blast cells in microculture. *Nature*. 1989;340(6233):471-473. doi:10.1038/340471a0.

211. Temple S. The development of neural stem cells. *Nature*. 2001;414(6859):112-117. doi:10.1038/35102174.

212. Gage FH. Mammalian Neural Stem Cells. *Science (80-)*. 2000;287(5457):1433-1438. doi:10.1126/science.287.5457.1433.

213. Shitasako S, Ito Y, Ito R, Ueda Y, Shimizu Y, Ohshima T. Wnt and Shh signals regulate neural stem cell proliferation and differentiation in the optic tectum of adult zebrafish. *Dev Neurobiol*. 2017;77(10):1206-1220. doi:10.1002/dneu.22509.

214. Rowitch DH, S-Jacques B, Lee SM, Flax JD, Snyder EY, McMahon a P. Sonic hedgehog regulates proliferation and inhibits differentiation of CNS precursor cells. *J Neurosci*. 1999;19(20):8954-8965. doi:10516314.

215. Palma V. Sonic hedgehog controls stem cell behavior in the postnatal and adult brain. *Development*. 2005;132(2):335-344. doi:10.1242/dev.01567.

216. Marino S. Medulloblastoma: Developmental mechanisms out of control. *Trends Mol Med*. 2005;11(1):17-22. doi:10.1016/j.molmed.2004.11.008.

217. Oustah AA, Danesin C, Khouri-Farah N, et al. Dynamics of Sonic hedgehog signaling in the ventral spinal cord are controlled by intrinsic changes in source cells requiring Sulfatase 1. *Development*. 2014;141(6):1392-1403. doi:10.1242/dev.101717.

218. Hui SP, Monaghan JR, Voss SR, Ghosh S. Expression pattern of Nogo-A, MAG, and NgR in regenerating urodele spinal cord. *Dev Dyn*. 2013;242(7):847-860. doi:10.1002/dvdy.23976.

219. Heine VM, Griveau A, Chapin C, Ballard PL, Chen JK, Rowitch DH. Preterm birth: A small-molecule smoothened agonist prevents glucocorticoid-induced neonatal cerebellar injury. *Sci Transl Med*. 2011;3(105). doi:10.1126/scitranslmed.3002731.

220. Londono R, Wenzhong W, Wang B, Tuan RS, Lozito TP. Cartilage and Muscle Cell Fate and Origins during Lizard Tail Regeneration. *Front Bioeng Biotechnol*. 2017;5(70). doi:10.3389/fbioe.2017.00070.

221. Tuan RS, Chen AF, Klatt BA. Cartilage regeneration. *J Am Acad Orthop Surg*. 2013;21(5):303-311. doi:10.5435/JAAOS-21-05-303.

222. Neogi T, Zhang Y. Epidemiology of Osteoarthritis. *Rheum Dis Clin North Am*. 2013;39(1):1-19. doi:10.1016/j.rdc.2012.10.004.

223. Bitton R. The economic burden of osteoarthritis. *Am J Manag Care*. 2009;15(8 Suppl):S230-S235. doi:10.1002/art.1780290311.

224. Ye K, Di Bella C, Myers DE, Choong PFM. The osteochondral dilemma: Review of current management and future trends. *ANZ J Surg*. 2014;84(4):211-217. doi:10.1111/ans.12108.

225. Moran CG, Horton TC. Total knee replacement: the joint of the decade. A successful operation, for which there's a large unmet need. *BMJ*. 2000;320(7238):820. http://www.pubmedcentral.nih.gov/articlerender.fcgi?artid=1127183&tool=pmcentrez&rendertype=abstract.

226. Nashi N, Hong CC, Krishna L. Residual knee pain and functional outcome following total knee arthroplasty in osteoarthritic patients. *Knee Surg Sports Traumatol Arthrosc*. 2014:1841-1847. doi:10.1007/s00167-014-2910-z.

227. Demoor M, Ollitrault D, Gomez-Leduc T, et al. Cartilage tissue engineering: Molecular control of chondrocyte differentiation for proper cartilage matrix reconstruction. *Biochim Biophys Acta - Gen Subj*. 2014;1840(8):2414-2440. doi:10.1016/j.bbagen.2014.02.030.

228. Kon E, Filardo G, Di Martino A, Marcacci M. ACI and MACI. *J Knee Surg*. 2012;25(1):17-22. doi:10.1055/s-0031-1299651.

229. Dewan AK, Gibson MA, Elisseeff JH, Trice ME. Evolution of autologous chondrocyte repair and comparison to other cartilage repair techniques. *Biomed Res Int*. 2014;2014(Table 1). doi:10.1155/2014/272481.

230. Kuo CK, Li WJ, Mauck RL, Tuan RS. Cartilage tissue engineering: its potential and uses. *Curr Opin Rheumatol*. 2006;18(1):64-73. doi:00002281-200601000-00011 [pii].

231. Pittenger MF. Multilineage Potential of Adult Human Mesenchymal Stem Cells. *Science (80-)*. 1999;284(5411):143-147. doi:10.1126/science.284.5411.143.

232. Rodríguez-merchán EC. Intra-Articular Injections of Mesenchymal Stem Cells for Knee Osteoarthritis. *Am J Orthop*. 2014;(December):282-291.

233. Emadedin M, Aghdami N, Taghiyar L, et al. Intra-articular Injection of Autologous Mesenchymal Stem Cells in Six Patients with Knee Osteoarthritis. *Arch Iran Med*. 2012;15(7):422-428. doi:012157/AIM.0010.

234. Jo CH, Lee YG, Shin WH, et al. Intra-articular injection of mesenchymal stem cells for the treatment of osteoarthritis of the knee: A proof-of-concept clinical trial. *Stem Cells*. 2014;32(5):1254-1266. doi:10.1002/stem.1634.

235. Li K-C, Hu Y-C. Cartilage Tissue Engineering: Recent Advances and Perspectives from Gene Regulation/Therapy. *Adv Healthc Mater*. 2015:n/a - n/a. doi:10.1002/adhm.201400773.

236. Bhardwaj N, Devi D, Mandal BB. Tissue-engineered cartilage: The crossroads of biomaterials, cells and stimulating factors. *Macromol Biosci*. 2015;15(2):153-182. doi:10.1002/mabi.201400335.

237. Trzeciak T, Richter M, Suchorska W. Application of cell and biomaterial-based tissue engineering methods in the treatment of cartilage , menisci and ligament injuries. 2016. doi:10.1007/s00264-015-3099-6.

238. Sun AX, Lin H, Beck AM, Kilroy EJ, Tuan RS. Projection Stereolithographic Fabrication of Human Adipose Stem Cell-Incorporated Biodegradable Scaffolds for Cartilage Tissue Engineering. *Front Bioeng Biotechnol*. 2015;3(August):115. doi:10.3389/fbioe.2015.00115.

239. Huang AH, Stein A, Tuan RS, Mauck RL. Transient exposure to transforming growth factor beta 3 improves the mechanical properties of mesenchymal stem cell-laden cartilage constructs in a density-dependent manner. *Tissue Eng Part A*. 2009;15(11):3461-3472. doi:10.1089/ten.TEA.2009.0198.

240. Erickson IE, Kestle SR, Zellars KH, et al. High mesenchymal stem cell seeding densities in hyaluronic acid hydrogels produce engineered cartilage with native tissue properties. *Acta Biomater*. 2012;8(8):3027-3034. doi:10.1016/j.actbio.2012.04.033.

241. Ponticiello MS, Schinagl RM, Kadiyala S, Barry FP. Gelatin-based resorbable sponge as a carrier matrix for human mesenchymal stem cells in cartilage regeneration therapy. *J Biomed Mater Res*. 2000;52(2):246-255. doi:10.1002/1097-4636(200011)52:2<246::AID-JBM2>3.0.CO;2-W.

242. Kavalkovich KW, Boynton RE, Murphy JM, Barry F. Chondrogenic differentiation of human mesenchymal stem cells within an alginate layer culture system. *In Vitro Cell Dev Biol Anim*. 2002;38(8):457-466. doi:10.1290/1071-2690(2002)038<0457:CDOHMS>2.0.CO;2.

243. Engler AJ, Sen S, Sweeney HL, Discher DE. Matrix Elasticity Directs Stem Cell Lineage Specification. *Cell*. 2006;126(4):677-689. doi:10.1016/j.cell.2006.06.044.

244. Tse JR, Engler AJ. Stiffness gradients mimicking in vivo tissue variation regulate mesenchymal stem cell fate. *PLoS One*. 2011;6(1):e15978. doi:10.1371/journal.pone.0015978.

245. Kshitiz, Park J, Kim P, et al. Control of stem cell fate and function by engineering physical microenvironments. *Integr Biol (Camb)*. 2012;4(9):1008-1018. doi:10.1039/c2ib20080e.

246. Khetan S, Guvendiren M, Legant WR, Cohen DM, Chen CS, Burdick J a. Degradation-mediated cellular traction directs stem cell fate in covalently crosslinked three-dimensional hydrogels. *Nat Mater*. 2013;12(5):458-465. doi:10.1038/nmat3586.

247. Yang C, Tibbitt MW, Basta L, Anseth KS. Mechanical memory and dosing influence stem cell fate. *Nat Mater*. 2014;13(6):645-652. doi:10.1038/nmat3889.

248. Murphy WL, McDevitt TC, Engler AJ. Materials as stem cell regulators. *Nat Mater*. 2014;13(6):547-557. doi:10.1038/nmat3937.

249. Wen JH, Vincent LG, Fuhrmann A, et al. Interplay of matrix stiffness and protein tethering in stem cell differentiation. *Nat Mater*. 2014;advance on:1-21. doi:10.1038/nmat4051.

250. Hendriks J a a, Moroni L, Riesle J, de Wijn JR, van Blitterswijk C a. The effect of scaffold-cell entrapment capacity and physico-chemical properties on cartilage regeneration. *Biomaterials*. 2013;34(17):4259-4265. doi:10.1016/j.biomaterials.2013.02.060.

251. Bian L, Hou C, Tous E, Rai R, Mauck RL, Burdick JA. The influence of hyaluronic acid hydrogel crosslinking density and macromolecular diffusivity on human MSC chondrogenesis and hypertrophy. *Biomaterials*. 2013;34(2):413-421. doi:10.1016/j.biomaterials.2012.09.052.

252. Toh WS, Lim TC, Kurisawa M, Spector M. Modulation of mesenchymal stem cell chondrogenesis in a tunable hyaluronic acid hydrogel microenvironment. *Biomaterials*. 2012;33(15):3835-3845. doi:10.1016/j.biomaterials.2012.01.065.

253. Caterson EJ, Nesti LJ, Danielson KG, Tuan RS. Human marrow-derived mesenchymal progenitor cells: isolation, culture expansion, and analysis of differentiation. *Mol Biotechnol*. 2002;20(3):245-256. doi:10.1385/MB:20:3:245.

254. Seck TM, Melchels FPW, Feijen J, Grijpma DW. Designed biodegradable hydrogel structures prepared by stereolithography using poly(ethylene glycol)/poly(d,l-lactide)-based resins. *J Control Release*. 2010;148(1):34-41. doi:10.1016/j.jconrel.2010.07.111.

255. Fairbanks BD, Schwartz MP, Bowman CN, Anseth KS. Photoinitiated polymerization of PEG-diacrylate with lithium phenyl-2,4,6-trimethylbenzoylphosphinate: polymerization rate and cytocompatibility. *Biomaterials*. 2009;30(35):6702-6707. doi:10.1016/j.biomaterials.2009.08.055.

256. Safranski DL, Gall K. Effect of chemical structure and crosslinking density on the thermo-mechanical properties and toughness of (meth)acrylate shape memory polymer networks. *Polymer (Guildf)*. 2008;49(20):4446-4455. doi:10.1016/j.polymer.2008.07.060.

257. Amarprett S. Sawhney, CHandrashokher P. Pathak and JAH. Bioerodible Hydrogels Based on Photopolymerized Poly(ethy1eneglycol)-co-poly(a-hydroxy acid) Diacrylate Macromers. *Macromolecules*. 1993;26:581-587. doi:10.1021/ma00056a005.

258. Bryant SJ, Anseth KS. Controlling the spatial distribution of ECM components in degradable PEG hydrogels for tissue engineering cartilage. *J Biomed Mater Res A*. 2003;64(1):70-79. doi:10.1002/jbm.a.10319.

259. Bryant SJ, Anseth KS. Hydrogel properties influence ECM production by chondrocytes photoencapsulated in poly(ethylene glycol) hydrogels. *J Biomed Mater Res*. 2002;59(1):63-72. doi:10.1002/jbm.1217.

260. Ikada Y. Challenges in tissue engineering. *J R Soc Interface*. 2006;3(10):589-601. doi:10.1098/rsif.2006.0124.

261. Farrell MJ, Comeau ES, Mauck RL. Mesenchymal stem cells produce functional cartilage matrix in three-dimensional culture in regions of optimal nutrient supply. *Eur Cell Mater*. 2012;23:425-440. doi:vol023a33 [pii].

262. Li WJ, Cooper J a., Mauck RL, Tuan RS. Fabrication and characterization of six electrospun poly(??-hydroxy ester)-based fibrous scaffolds for tissue engineering applications. *Acta Biomater*. 2006;2(4):377-385. doi:10.1016/j.actbio.2006.02.005.

263. Levett PA, Melchels FPW, Schrobback K, Hutmacher DW, Malda J, Klein TJ. A biomimetic extracellular matrix for cartilage tissue engineering centered on photocurable gelatin, hyaluronic acid and chondroitin sulfate. *Acta Biomater*. 2014;10(1):214-223. doi:10.1016/j.actbio.2013.10.005.

264. Tuli R, Nandi S, Li WJ, et al. Human mesenchymal progenitor cell-based tissue engineering of a single-unit osteochondral construct. *Tissue Eng*. 2004;10(7-8):1169-1179. doi:10.1089/ten.2004.10.1169.

265. Bhumiratana S, Eton RE, Oungoulian SR, Wan LQ, Ateshian GA, Vunjak-Novakovic G. Large, stratified, and mechanically functional human cartilage grown in vitro by mesenchymal condensation. *Proc Natl Acad Sci U S A*. 2014;111(19):6940-6945. doi:10.1073/pnas.1324050111.

266. Bian L, Guvendiren M, Mauck RL, Burdick J a. Hydrogels that mimic developmentally relevant matrix and N-cadherin interactions enhance MSC chondrogenesis. *Proc Natl Acad Sci U S A*. 2013;110(25):10117-10122. doi:10.1073/pnas.1214100110.

267. Hubka KM, Dahlin RL, Meretoja V V, Kasper K, Mikos AG. Enhancing Chondrogenic Phenotype for Cartilage Tissue Engineering: Monoculture and Co-culture of Articular Chondrocytes and Mesenchymal Stem Cells. *Tissue Eng Part B.* 2014;20(6):1-50. doi:10.1089/ten.TEB.2014.0034.

268. Chen S, Fu P, Cong R, Wu HS, Pei M. Strategies to minimize hypertrophy in cartilage engineering and regeneration. *Genes Dis*. 2015;2(1):76-95. doi:10.1016/j.gendis.2014.12.003.

269. Bian L, Guvendiren M, Mauck RL, Burdick J a. Hydrogels that mimic developmentally relevant matrix and N-cadherin interactions enhance MSC chondrogenesis. *Proc Natl Acad Sci U S A.* 2013;110(25):10117-10122. doi:10.1073/pnas.1214100110.

270. Klein TJ, Rizzi SC, Schrobback K, et al. Long-term effects of hydrogel properties on human chondrocyte behavior. *Soft Matter*. 2010;6:5175. doi:10.1039/c0sm00229a.

271. Chung C, Burdick JA. Influence of three-dimensional hyaluronic acid microenvironments on mesenchymal stem cell chondrogenesis. *Tissue Eng Part A.* 2009;15(2):243-254. doi:10.1089/ten.tea.2008.0067.

272. Mauck RL, Wang CCB, Oswald ES, Ateshian G a., Hung CT. The role of cell seeding density and nutrient supply for articular cartilage tissue engineering with deformational loading. *Osteoarthr Cartil*. 2003;11(12):879-890. doi:10.1016/j.joca.2003.08.006.

273. Mauck RL, Seyhan SL, Ateshian G a., Hung CT. Influence of Seeding Density and Dynamic Deformational Loading on the Developing Structure/Function Relationships of Chondrocyte-Seeded Agarose Hydrogels. *Ann Biomed Eng*. 2002;30(8):1046-1056. doi:10.1114/1.1512676.